

INFORMATION TO USERS

This manuscript has been reproduced from the microfilm master. UMI films the text directly from the original or copy submitted. Thus, some thesis and dissertation copies are in typewriter face, while others may be from any type of computer printer.

The quality of this reproduction is dependent upon the quality of the copy submitted. Broken or indistinct print, colored or poor quality illustrations and photographs, print bleedthrough, substandard margins, and improper alignment can adversely affect reproduction.

In the unlikely event that the author did not send UMI a complete manuscript and there are missing pages, these will be noted. Also, if unauthorized copyright material had to be removed, a note will indicate the deletion.

Oversize materials (e.g., maps, drawings, charts) are reproduced by sectioning the original, beginning at the upper left-hand corner and continuing from left to right in equal sections with small overlaps.

Photographs included in the original manuscript have been reproduced xerographically in this copy. Higher quality 6" x 9" black and white photographic prints are available for any photographs or illustrations appearing in this copy for an additional charge. Contact UMI directly to order.

ProQuest Information and Learning
300 North Zeeb Road, Ann Arbor, MI 48106-1346 USA
800-521-0600

UMI[®]

**Ionospheric Influence on the Global Characteristics of
Electron Precipitation During Auroral Substorms**

Damien Han Chua

**A dissertation submitted in partial fulfillment of
the requirements for the degree of**

Doctor of Philosophy

University of Washington

2002

Program Authorized to Offer Degree: Department of Earth and Space Sciences

UMI Number: 3041016

UMI[®]


UMI Microform 3041016

Copyright 2002 by ProQuest Information and Learning Company.

All rights reserved. This microform edition is protected against
unauthorized copying under Title 17, United States Code.

ProQuest Information and Learning Company
300 North Zeeb Road
P.O. Box 1346
Ann Arbor, MI 48106-1346

In presenting this dissertation in partial fulfillment of the requirements for the Doctoral degree at the University of Washington, I agree that the Library shall make its copies freely available for inspection. I further agree that extensive copying of this dissertation is allowable only for scholarly purposes, consistent with "fair use" as prescribed in the U.S. Copyright Law. Requests for copying or reproduction of this dissertation may be referred to Bell and Howell Information and Learning, 300 North Zeeb Road, Ann Arbor, MI 48106-1346, to whom the author has granted "the right to reproduce and sell (a) copies of the manuscript in microform and/or (b) printed copies of the manuscript made from microform."

Signature 

Date March 21, 2002

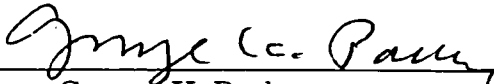
University of Washington
Graduate School

This is to certify that I have examined this copy of a doctoral dissertation by

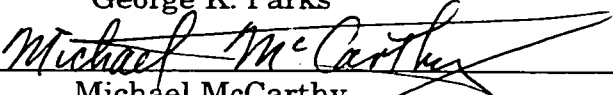
Damien Han Chua

and have found that it is complete and satisfactory in all respects,
and that any and all revisions required by the final
examining committee have been made.

Co-Chairs of Supervisory Committee:

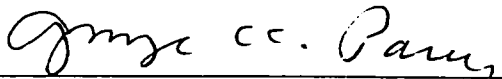


George K. Parks




Michael McCarthy


Reading Committee:



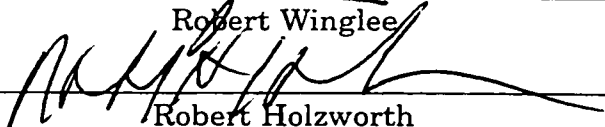
George K. Parks



Michael McCarthy



Robert Winglee



Robert Holzworth

Date: MARCH 21, 2002

University of Washington

Abstract

Ionospheric Influence on the Global Characteristics of
Electron Precipitation During Auroral Substorms

by Damien Han Chua

Co-Chairs of Supervisory Committee:

Professor George K. Parks
Department of Earth and Space Sciences

Professor Michael McCarthy
Department of Earth and Space Sciences

Global auroral images from the Polar Ultraviolet Imager (UVI) and *in situ*, low altitude particle measurements from the Fast Auroral Snapshot Explorer (FAST) spacecraft are used to investigate the effects of solar wind variations and seasonal variability in the ionosphere on electron precipitation during auroral substorms. Isolated substorms and storm-time, pressure pulse-driven intensifications are compared and we show that the global patterns of precipitating electron energy flux and average energy are markedly different for each class of auroral phenomena. Field-aligned acceleration of auroral electrons in the upward current regions is found to be an essential aspect of the global aurora during isolated substorms. In contrast, the electron precipitation during pressure pulse-driven intensifications is less structured with no indication of field-aligned acceleration.

A new method of quantifying the time scales and phases of magnetospheric substorms using the hemispheric power derived from the UVI images is described. We show that substorm time scales vary most strongly with season while IMF orientation plays a secondary role. The recovery time for substorm activity is roughly a factor of

two longer when the nightside auroral zone is in darkness (winter and equinox) than when it is sunlit. We find that the longer time scale of substorms occurring in darkness is sustained by discrete auroral features associated with field-aligned potential drops and inertial Alfvén waves. These discrete structures exist for shorter time scales, if they are observed at all, during substorms that occur under sunlit conditions. The observed seasonal variations in global auroral structure during substorms are most consistent with the hypothesis that ionospheric boundary conditions strongly influence the effectiveness of auroral acceleration mechanisms that include parallel potentials and Alfvén waves. The results presented in this thesis will enhance our understanding of substorm phenomena by bridging the gap between the microphysical description of the aurora and that describing the variations in auroral morphology on substorm time scales of tens of minutes to hours.

TABLE OF CONTENTS

| | |
|--|------------|
| List of Figures | iv |
| List of Tables | vii |
| Chapter 1: Introduction | 1 |
| 1.1 Auroral Structure | 3 |
| 1.1.1 Auroral acceleration and discrete aurora | 4 |
| 1.1.2 Diffuse aurora | 5 |
| 1.1.3 Auroral oval | 6 |
| 1.2 The Dynamic Aurora | 9 |
| 1.2.1 Interplanetary pressure pulse driven aurora | 13 |
| 1.2.2 Seasonal variability in aurorae | 13 |
| 1.3 Objectives of This Dissertation | 16 |
| Chapter 2: Instrumentation | 20 |
| 2.1 Polar Ultraviolet Imager (UVI) | 21 |
| 2.1.1 Field of View | 21 |
| 2.1.2 Filters | 22 |
| 2.1.3 Polar Spacecraft Wobble | 24 |
| 2.2 Quantitative Analysis of UVI Images | 25 |
| 2.2.1 Energy Flux | 26 |
| 2.2.2 Average Energy | 28 |
| 2.2.3 Considerations of the neutral atmosphere | 29 |
| 2.2.4 Effect of different electron distributions | 33 |
| 2.3 Fast Auroral Snapshot (FAST) Explorer: Particle measurements | 33 |

| | | |
|---------------------|---|------------|
| 2.3.1 | Magnetospheric Particle Dynamics | 34 |
| 2.3.2 | Electrostatic Analyzers (ESAs) | 36 |
| Chapter 3: | A Comparison of Isolated Substorms and Pressure Pulse Driven Auroral Activity | 37 |
| 3.1 | Isolated Auroral Substorms | 38 |
| 3.2 | Pressure Pulse Related Auroral Activity | 45 |
| 3.3 | Summary | 56 |
| Chapter 4: | Seasonal Variations in Auroral Structure and Time Scales During Substorms | 58 |
| 4.1 | Substorm phases defined by hemispheric power | 59 |
| 4.1.1 | IMF influence on substorm hemispheric power | 62 |
| 4.2 | Seasonal variations of auroral substorm characteristics | 70 |
| 4.3 | Superposed epoch analysis of auroral electron energy flux and average energy | 78 |
| 4.3.1 | Pre-onset ($t < T_{\text{onset}}$) | 78 |
| 4.3.2 | Onset ($t = T_{\text{onset}}$) | 80 |
| 4.3.3 | Substorm expansion ($T_{\text{onset}} - T_{\text{HPmax}}$) | 81 |
| 4.3.4 | $T_{\text{HPmax}} - \tau$ | 83 |
| 4.3.5 | $\tau - 2\tau$ | 96 |
| 4.3.6 | $2\tau - 3\tau$ | 97 |
| 4.3.7 | Dayside auroral characteristics | 98 |
| 4.3.8 | Comparison to earlier studies | 99 |
| 4.4 | Summary of observations | 100 |
| Chapter 5: | Summary and Conclusions | 104 |
| 5.1 | Future work | 106 |
| Bibliography | | 108 |

| | |
|---|------------|
| Appendix A: Data Processing Techniques for the Quantitative Analysis of UVI Images | 120 |
| A.1 Line of Sight Correction | 120 |
| A.2 Dayglow Correction | 121 |
| A.3 UVI image binning | 124 |
| Appendix B: Relation between AE and UVI derived Hemispheric Power | 127 |
| Appendix C: Ancillary Data | 131 |

LIST OF FIGURES

| | |
|--|----|
| 1.1 The terrestrial magnetosphere | 2 |
| 1.2 Coincident aircraft and satellite particle measurements of discrete auroral arcs | 5 |
| 1.3 Contour lines of equal auroral frequency (isochasms). From <i>Fritz</i> [1873]. | 7 |
| 1.4 The phases of an auroral substorm | 10 |
| 1.5 UVI images of a typical auroral substorm | 11 |
| 1.6 Monthly frequency of aurora between 1911-1951 | 15 |
| 2.1 Evolution of Polar's orbit, 1996-2002 | 21 |
| 2.2 Polar UVI field of view parameters | 22 |
| 2.3 FUV N ₂ LBH Spectrum | 23 |
| 2.4 Passbands of UVI filters. | 24 |
| 2.5 Wobble signature in star observations. | 25 |
| 2.6 Surface brightness (kR) as a function of incident energy flux. | 28 |
| 2.7 Mean energy versus LBHL:LBHs ratio. | 30 |
| 2.8 O:N ₂ and N ₂ : O ₂ altitude profiles | 31 |
| 2.9 Seasonal variation of modeled 1356 Å:LBHL and LBHL:LBHs ratios . . | 32 |
| 3.1 UVI observations during an isolated substorm on December 18, 1996. . | 42 |
| 3.2 UVI and FAST observations for the January 30, 1988 substorm. | 44 |
| 3.3 Solar wind and auroral zone data on August 25-27, 1998. | 47 |
| 3.4 UVI observations for August 26, 1998 CME event. | 49 |
| 3.5 FAST electron pitch angle and energy-time spectrograms for orbit 7954. | 51 |
| 3.6 Electron energy spectra at for the August 26, 1998 pressure pulse event. | 53 |

| | | |
|------|--|-----|
| 3.7 | A comparison of FAST and UVI derived mean energy values | 54 |
| 4.1 | Hemispheric power during an isolated substorm on January 25, 1998. . | 61 |
| 4.2 | Hemispheric power for a substorm occurring during southward IMF con- ditions | 64 |
| 4.3 | Superposed epoch analysis of hemispheric power | 65 |
| 4.4 | Histograms of the peak hemispheric power values for substorms sorted by IMF B_z orientation | 66 |
| 4.5 | Histograms of substorm expansion times sorted by IMF B_z orientation . | 67 |
| 4.6 | Histograms of substorm recovery times sorted by IMF B_z orientation . . | 68 |
| 4.7 | Distributions of total energy dissipated during substorm events sorted by IMF B_z orientation | 69 |
| 4.8 | Seasonal variations in ionospheric Pedersen conductance | 71 |
| 4.9 | Seasonal distributions of substorm peak hemispheric power. | 73 |
| 4.10 | Seasonal distributions of substorm expansion times. | 74 |
| 4.11 | Seasonal distributions of substorm e -folding times. | 75 |
| 4.12 | Total energy deposition sorted by season | 76 |
| 4.13 | Superposed epoch analysis for the pre-onset epoch | 85 |
| 4.14 | Superposed epoch analysis at substorm onset | 87 |
| 4.15 | Superposed epoch analysis for substorm expansion ($T_{\text{onset}} - T_{\text{HPmax}}$) . . | 89 |
| 4.16 | Superposed epoch analysis for $T_{\text{HPmax}} - \tau$ | 91 |
| 4.17 | Superposed epoch analysis for $\tau - 2\tau$ | 93 |
| 4.18 | Superposed epoch analysis for $2\tau - 3\tau$ | 95 |
| 4.19 | UVI inferred energy flux and mean energy averaged over all substorm epochs and sorted by season | 100 |
| A.1 | Line of sight factors. | 122 |
| A.2 | Binned dayglow flux versus solar zenith angle | 123 |
| A.3 | Dayglow subtraction example. | 124 |

| | | |
|------|--|-----|
| A.4 | UVI image mappings | 125 |
| B.1 | UVI derived hemispheric power versus AE index | 129 |
| C.1 | UVI images corresponding to FAST orbit 1719 | 132 |
| C.2 | UVI images corresponding to FAST orbit 4666 | 133 |
| C.3 | UVI images corresponding to FAST orbit 11077 | 134 |
| C.4 | UVI images corresponding to FAST orbit 1710 | 135 |
| C.5 | UVI images corresponding to FAST orbit 4164 | 136 |
| C.6 | UVI images corresponding to FAST orbit 1759 | 137 |
| C.7 | UVI images corresponding to FAST orbit 12443 | 138 |
| C.8 | UVI images corresponding to FAST orbit 11102 | 139 |
| C.9 | UVI images corresponding to FAST orbit 5644 | 140 |
| C.10 | More examples of summer-time FAST electron measurements during substorm expansion | 141 |
| C.11 | UVI images corresponding to FAST orbit 1910 | 142 |
| C.12 | UVI images corresponding to FAST orbit 14999 | 143 |
| C.13 | UVI images corresponding to FAST orbit 5590 | 144 |
| C.14 | UVI images corresponding to FAST orbit 7979 | 145 |
| C.15 | UVI images corresponding to FAST orbit 7067 | 146 |
| C.16 | UVI images corresponding to FAST orbit 1720 | 147 |
| C.17 | UVI images corresponding to FAST orbit 8033 | 148 |
| C.18 | UVI images corresponding to FAST orbit 11273 | 149 |

LIST OF TABLES

| | | |
|-----|---|-----|
| 3.1 | Interplanetary pressure pulse driven intensifications observed by Polar UVI | 38 |
| 4.1 | Substorm epochs defined by the UVI derived hemispheric power | 102 |
| B.1 | Linear fits and correlation coefficients between AE index and UVI derived hemispheric power | 128 |

ACKNOWLEDGMENTS

The work presented in this thesis was made possible through the generous opportunities in research and guidance provided by my advisor, Professor George K. Parks. He has provided life-long lessons in scholarship and inquiry into the natural world. Further thanks go to Professors Michael McCarthy, Robert Winglee, and Bob Holzworth for their academic and professional guidance.

I extend my gratitude to Drs. Mitch Brittnacher, Glynn Germany, Jim Spann, and Dirk Lummerzheim for their contributions to this work. The quantitative analysis of the Polar UVI images in this dissertation would not have been possible without the groundwork established by these individuals.

A special acknowledgment is extended to Dr. William Peria who generously provided invaluable guidance in the analysis of the FAST particles and fields data. His fresh insights and open mind were a great help in seeing through many challenging problems. Dr. Chuck Carlson is thanked for granting access to the FAST data and for providing valuable discussions regarding the FAST particle measurements.

I am thankful for the friendship and commiseration of my fellow graduate students who over the years have included Matt Fillingim, Li-Jen Chen, John Williams, Ruth Wilton-Godberfforde, Robyn Millan, Carol Paty, Frank Marcoline and Drs. Mark Wilber, Ted Freeman, Kirsten Lorentzen, Frank Lind, Kerry Deutsch, and Suvro Datta. Sarah, you're the best.

The research presented in this dissertation was supported by the International Solar Terrestrial Physics Program and the Polar Ultraviolet Imager project through NASA grant NAG5-3170.

DEDICATION

For Sarah and her infinite patience.

Chapter 1

INTRODUCTION

The upper atmosphere hosts a variety of dynamic, luminous phenomena. Among the most well known and studied of these is the aurora. Auroral light emissions arise from collisions between energetic charged particles (electrons and ions) and constituents of the upper atmosphere such as molecular nitrogen (N_2) and atomic oxygen (O). The results of these interactions are luminous structures observed at altitudes near 100 km and above, nominally at polar latitudes. This altitude region corresponds to the *ionosphere* where the upper atmosphere is partially ionized due primarily to solar ultraviolet radiation. Auroral displays occur over a large range of length scales (tens of meters to hundreds of kilometers) and can vary in form and color over short time scales (seconds). As such, aurorae have a strong visual impact and a visceral appeal that commands interest from casual observers and scientific investigators alike.

Auroral emissions occur at the interface between the upper atmosphere and the *magnetosphere*, the region of space surrounding the Earth (or in general, any magnetized planetary body) in which charged particles are under the influence of its magnetic field (Figure 1.1). Understanding the dynamics of the aurora is therefore essential for investigations of the coupling between the magnetosphere and ionosphere. Magnetospheric plasmas are composed of electrons and ions in a quasi-neutral state. Since the sources of charged particles involved in auroral production are generally found in various regions of the magnetosphere, as illustrated in Figure 1.1, the analogy is often made that the magnetosphere acts like a cathode tube with the ionosphere serving as a television screen that luminesces when bombarded by incident magnetospheric electrons. In this traditional view, the aurora is considered to be a projection of processes

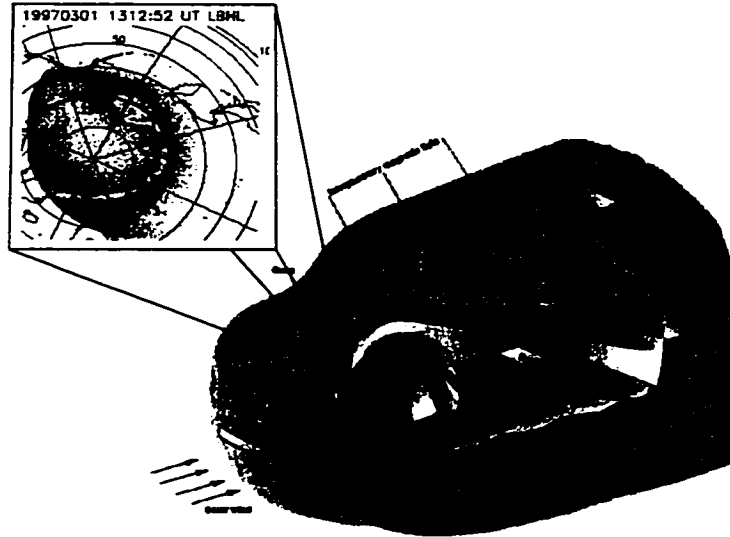


Figure 1.1: A cartoon depiction of the Earth's magnetosphere and various regions of plasma within it.

occurring in the magnetosphere. Here, the ionosphere acts as a passive sink for auroral particle and energy inputs from the magnetospheric source. Examples of this treatment are magnetohydrodynamic (MHD) simulations of the aurora that model it using estimates of magnetospheric energy flux through their inner (near-Earth) boundaries [Walker *et al.*, 1993] or through proxies such as field-aligned current strength [Fedder *et al.*, 1994].

In contrast, an increasing number of studies strongly suggest that the ionosphere plays a more active role in auroral dynamics than previously thought. The state of the high latitude, auroral ionosphere has strong seasonal variations. In the summer months, the high latitude ionosphere is continuously sunlit. Photoionization gives rise to photoelectrons and enhanced ionospheric conductivity that are absent during the polar winters when this region is in continual darkness. The conductivity in the ionosphere is an important parameter for many models of magnetosphere-ionosphere (MI) coupling [Lysak, 1991; Chiu and Shulz, 1978, for example] and affects how currents and electric fields associated with the aurora behave. For example, the calculations

of *Chiu and Shulz* [1978] predict an inverse relationship between the ionospheric ion density (which is related to the degree of solar insolation and ionospheric conductivity) and the electrostatic potential drop along a magnetic field line connecting the ionosphere and magnetosphere. Field-aligned potential drops are widely accepted to be key elements for the formation of discrete auroral arcs. This prediction has some observational support from statistical studies that have compared characteristics of the aurora during the winter versus summer (See Section 1.2.2).

The analysis of coordinated optical and *in situ* observations of the aurora presented in this thesis provides further evidence for the emerging view that the ionospheric boundary conditions at the foot of auroral field lines play a significant role in not only determining the synoptic scale structure of the aurora but the time scales of its dynamics as well. Our analysis of seasonal variations in global auroral characteristics includes equinoctial periods that were largely neglected in previous studies which focused on solstitial conditions. We expand upon previous studies by showing how shorter time scale activity in the aurora (i.e. substorms) varies as a function of season. Moreover, this dissertation will describe the circumstances in which auroral activity appears independent of conditions in the ionosphere.

1.1 Auroral Structure

For any given observation of the aurora, it is possible to view a multitude of auroral forms that vary on spatial and temporal scales spanning many orders of magnitude. Early researchers such as *Störmer* [1955] found that one could break down the aurora into more elementary structures. Despite their complexity, aurorae are commonly divided into discrete and diffuse forms. Underlying the differences in their appearance is the fact that discrete and diffuse aurora represent distinct physical processes. The way in which the discrete and diffuse components of the aurora vary as a function of space, time, and geomagnetic activity gives us insight into the processes which couple the ionosphere and magnetosphere.

1.1.1 Auroral acceleration and discrete aurora

Visually, discrete aurorae correspond to a variety of auroral arcs that include the familiar curtain-like forms with which most casual observers are familiar. *Störmer* [1955] describes these as resembling “a curtain hanging down, with its lower border undulating and more luminous than the upper-rayed part.” To a ground observer whose field of view from horizon to horizon may extend over a few hundred kilometers, discrete auroral arcs have a long east-west extension while the scale size in the north-south direction is typically on the order of a few to tens of kilometers. Fine structure within individual discrete arcs with scale sizes of tens of meters, on the order of proton gyroradii in the ionosphere, has been reported [*Maggs and Davis*, 1968], but remains poorly understood.

In situ particles and fields observations from rocket and satellite borne instruments have shown that field-aligned acceleration of the precipitating auroral electrons is an important process above discrete arcs. Signatures known as inverted-V structures in electron energy-time spectra [*Frank and Ackerson*, 1971] are indications of quasi-monoenergetic electron precipitation at keV energies over discrete arcs. These are interpreted as the result of field-aligned acceleration of primary auroral electrons through a potential drop parallel to the magnetic field [*Evans*, 1974]. How an electric field can be supported along the direction of the magnetic field for a collisionless plasma remains an ongoing topic of research. *Kamide and Rostoker* [1977] also showed that discrete auroral structures are associated with upward field-aligned currents (FAC) flowing out of the ionosphere.

The correspondence between optically observed discrete auroral arcs and inverted-V signatures in electron energy-time spectra is demonstrated by *Stenbaek-Nielsen et al.* [1998] who compared all-sky auroral images obtained from an aircraft with particle data measured simultaneously above the cameras’ field of view by the Fast Auroral Snapshot (FAST) spacecraft. The top panel of Figure 1.2 is an all-sky image that shows several discrete auroral arcs. The white dots indicate the nominal magnetic footprint of the FAST satellite as it flies through the all-sky camera’s field of view. The middle

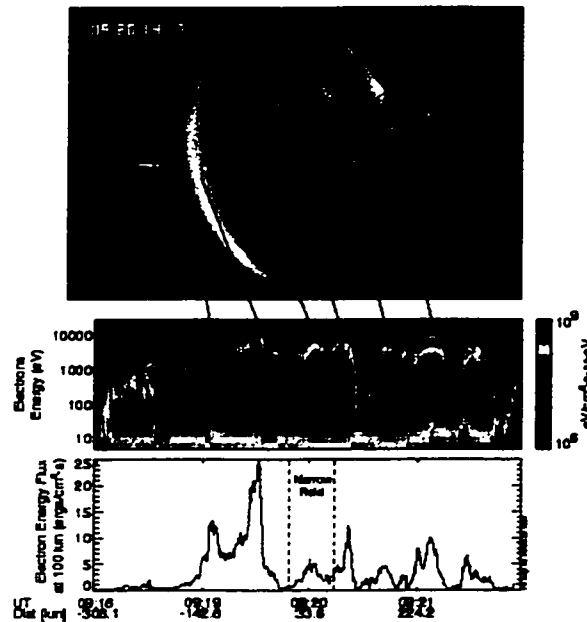


Figure 1.2: The top panel shows an all-sky (white light) image of multiple, discrete auroral arcs. The center panel displays an energy-time spectrogram integrated over all pitch angles showing inverted-V structures each corresponding to an auroral arc. The bottom panel shows the integrated energy flux ($\text{ergs cm}^{-2} \text{s}^{-1}$) mapped to 100 km altitude (from *Stenbaek-Nielsen et al.* [1998]).

panel (Figure 1.2 shows an energy-time spectrogram integrated over all pitch angles for the time period of the FAST overflight shown in the panel above. Intense fluxes of electrons within a narrow band of energies between 1-10 keV correspond to each discrete auroral arc in the all-sky image above. The peak energy of each inverted-V is near 10 keV and occurs close to the center of each arc.

1.1.2 Diffuse aurora

In addition to discrete auroral forms, *Lui and Anger* [1973] showed that the aurora had a diffuse component that was less structured and more uniform across larger scale lengths with less distinct boundaries. *Störmer* [1955] also noted diffuse aurora as a

principal auroral form, although for a ground observer diffuse aurora are generally sub-visible. Discrete structures are often found embedded within diffuse aurora. In general, regions of diffuse aurora are observed equatorward of discrete aurora.

Diffuse aurora represents magnetospheric electron precipitation that has not been accelerated by a mechanism such as a magnetic field-aligned potential drop. In contrast to discrete aurora, the creation of diffuse aurora involves processes occurring in the magnetospheric source regions rather than those operating closer to the auroral ionosphere. The source of diffuse precipitation is believed to be the earthward region of the central plasma sheet in the magnetotail. Electron spectra measured *in situ* in the plasma sheet and at lower altitudes over diffuse aurora are generally Maxwellian or kappa-like distributions with temperatures of a few keV. Kappa distributions are generalized Lorentzian functions that characterize space plasmas with a non-Maxwellian, suprathermal tail [Summers and Thorne, 1991].

1.1.3 Auroral oval

On a global scale, the aurorae described above occur within a band of luminosity in each hemisphere, roughly centered about the magnetic poles, known as the auroral oval. The earliest efforts to understand the global distribution of aurora include the work of *Fritz* [1873] and *Vestine* [1944] who mapped out lines of auroral frequency, M , defined as the mean number of days with auroral sightings per year. Lines of constant M values were defined as *isochasms*. In Figure 1.3 (From *Fritz* [1873]) the thickest contour lines correspond to the maximum values of M , where aurorae are observed most frequently. Statistically compiled maps such as Figure 1.3 were the first representations of the auroral oval.

A prominent milestone in describing the global auroral distribution came with the deployment of a world-wide network of all-sky cameras during the International Geophysical Year (IGY) 1957 [Akasofu, 1964, 1968]. This provided one of the first coherent descriptions of how the aurora behaves on a global scale during heightened auroral activity (Figure 1.4). Examinations of the aurora on spatial scales much larger than those

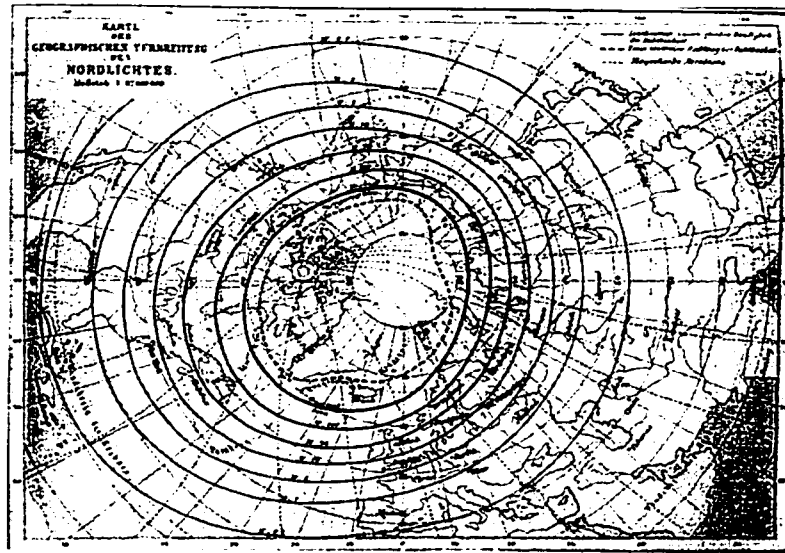


Figure 1.3: Contour lines of equal auroral frequency, defined as *isochasms* (From *Fritz* [1873]). Such maps were the first representations of the auroral oval.

associated with individual auroral arcs was an important observational and conceptual leap that allowed auroral phenomena to be related to magnetospheric processes.

Auroral images obtained from spacecraft quickly became valuable diagnostic tools used to relate *in situ* point measurements, either taken on the ground or by spacecraft, to auroral or magnetospheric activity occurring over much larger spatial scales. Early advances from spacecraft-borne auroral imagers included the identification of the diffuse aurora from ISIS-2 observations [*Lui and Anger*, 1973] in addition to more thorough studies of the dayside aurora and its association with the polar cusp region [*Shephard et al.*, 1976; *Meng and Lundin*, 1986, for example]. Moreover, continuous monitoring of the auroral oval over time periods of several hours allowed for the observation of previously unidentified large-scale auroral features. For example, global auroral images from the Dynamics Explorer 1 (DE-1) revealed the occurrence of sun-aligned auroral arcs, now known as theta aurora, that extended from the midday to nightside oval [*Frank et al.*, 1982]. *Meng and Mauk* [1991] provide a thorough review of the global auroral imaging experiments prior to the launch of the Polar spacecraft.

Quantitative analysis of auroral images emerged quickly for such data to be used

for measurement rather than just reference. *Holzworth and Meng* [1975] formulated a mathematical representation of the auroral oval based on Defense Meteorological Satellite Program (DMSF) auroral photographs. This technique, which was later applied by *Meng et al.* [1977], provided a quantitative means for specifying the location and size of the auroral oval during quiet conditions. Once the observational capabilities allowed, monitoring the instantaneous, global aurora became very valuable for magnetospheric-ionospheric studies. Difficulties with observing the aurora at visible wavelengths under sunlit conditions were overcome by imaging the aurora in the ultraviolet where the terrestrial albedo from incident solar radiation is much lower [*Meng and Huffman*, 1984; *Meng and Chakrabarti*, 1985; *Frank et al.*, 1982; *Anger et al.*, 1987, for example].

As remote sensing tools, multispectral auroral images allow the characteristics of auroral precipitation to be inferred over spatial scales and extended time intervals not possible through single point measurements alone. The technique of extracting precipitating particle characteristics from global auroral images generally exploits emission features at different wavelengths that vary as a function of the energy flux and average energy of the incident particles. This method relies on model calculations of expected emission intensities for a given energy flux and energy spectrum of incident particles. These calculations have been done for visible [*Rees and Luckey*, 1974; *Richards and Torr*, 1990] and far ultraviolet [*Strickland et al.*, 1983; *Germany et al.*, 1994b] wavelengths.

In Chapter 2, we describe in detail the application of this technique to Polar UVI images to infer the precipitating electron energy flux and average energies. Previously, *Ishimoto et al.* [1988] used UV observations of the N₂ Lyman-Birge-Hopfield (LBH) and Vegard-Kaplan (VK) emission bands from the S3-4 satellite to estimate the precipitating electron energy flux and average energy. Other efforts to estimate these parameters from FUV auroral observations include those of *Steele et al.* [1992] using Viking data and *Rees et al.* [1988] with images from the DE-1 spacecraft. Observations of auroral x-rays from spacecraft have also been used to infer energy fluxes and average energies, particularly for electrons with energies greater than $\sim 10\text{keV}$ [*Datlowe*

et al., 1993; *Stadsnes et al.*, 1997; *Cummer et al.*, 2000; *Ostgaard et al.*, 1999, 2001].

1.2 The Dynamic Aurora

Previously, we outlined the general structure of the aurora and described some basic processes in the magnetosphere that contribute to auroral physics. This description of the aurora is largely a static one however. Changes in aurora on times scales from seconds to minutes may be (quasi-)periodic as in pulsating aurora [*Bryant et al.*, 1969; *Johnstone*, 1978; *Royrvik and Davis*, 1977; *Tanskanen*, 1991, for example] or impulsive in the case of auroral substorms.

As we mentioned above, one of the first coherent descriptions of how the aurora behaves on a global scale during heightened auroral activity is given by *Akasofu* [1964] who studied optical observations from a network of all-sky cameras in the auroral zone obtained during the International Geophysical Year 1957. *Akasofu* [1964] describes two phases of enhanced auroral activity which became the canonical description of the *auroral substorm* or *polar magnetic substorm* [*Akasofu et al.*, 1965, 1966b; *Akasofu and Meng*, 1969].

In the *expansive* phase, a quiet auroral arc near magnetic midnight suddenly intensifies in brightness and rapidly moves toward the geomagnetic pole and outwards in local time (longitude) over a period of tens of minutes at a rate of a few kilometers per second. Sketches of auroral morphology during the substorm expansive (expansion) phase are shown in panels B-D of Figure 1.4 (from *Akasofu* [1964]). A prominent feature of the expansion phase is shown in Figures 1.4 C and D where intense, folded arcs along the western edge of the substorm bulge propagate rapidly toward the evening sector. This is known as the *westward surge*. *Akasofu et al.* [1966a] note that for ground magnetometers near local midnight during a substorm expansion the vertical component of the magnetic field changes sign as the auroral disturbance and its associated currents move poleward overhead. Large decreases in the horizontal component of the magnetic field are also observed by auroral zone magnetometers as the westward traveling electrojet (surge) develops during the auroral expansion [*Akasofu*

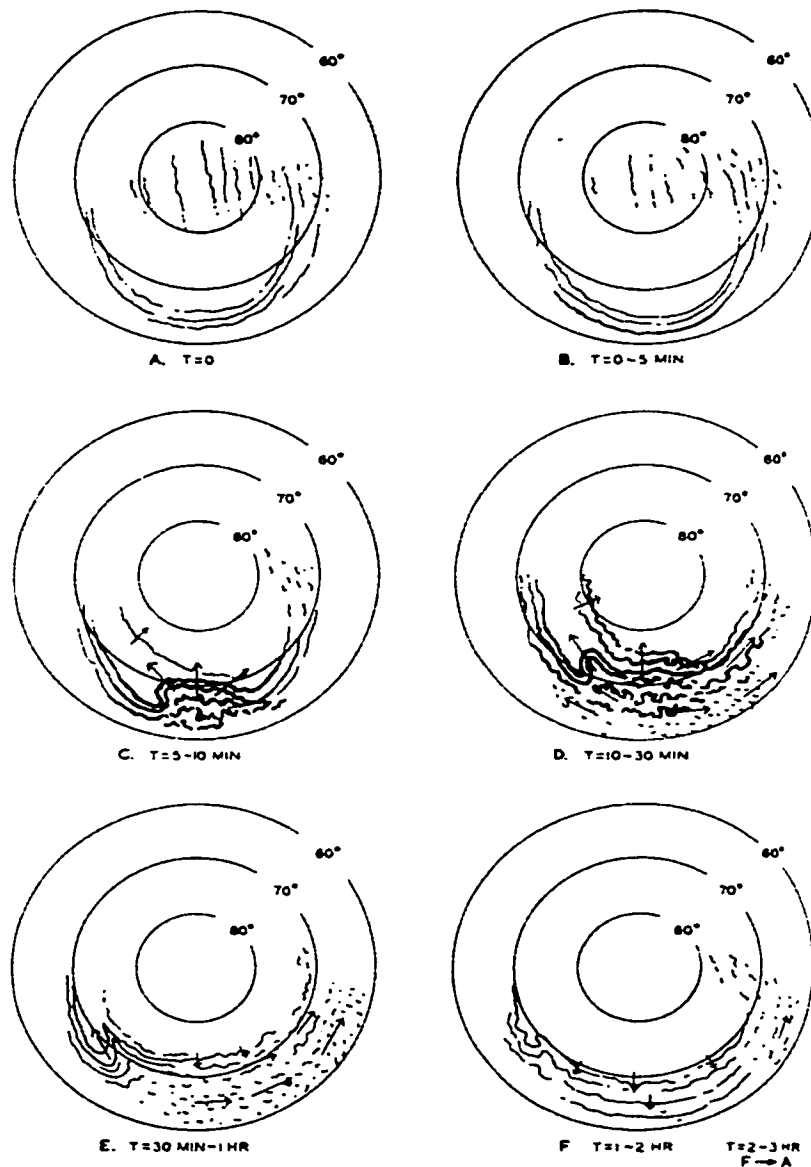


Figure 1.4: Sketches of the development of an auroral substorm. These statistical auroral distributions are based on all-sky camera observations during IGY 1957. Geomagnetic latitudes are shown and the sunward direction is at the top of each diagram (From Akasofu [1964]).

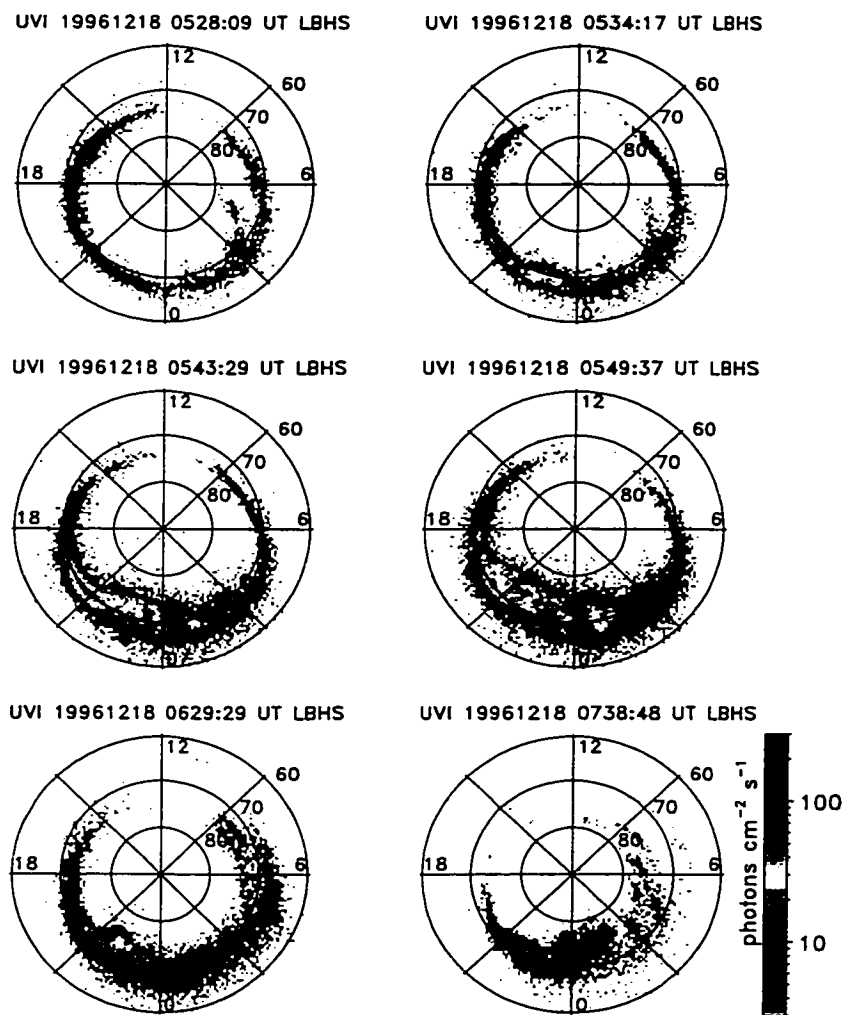


Figure 1.5: UVI images showing the global auroral morphology through the course of an auroral substorm on December 18, 1996. A comparison of these snapshots of the aurora with the statistical diagrams of *Akasofu* [1964] shown in Figure 1.4 shows a high degree of similarity.

et al., 1966b].

The *recovery* phase begins once the substorm bulge dims and begins to retreat equatorward from its most poleward extent, usually at a rate slower than its poleward expansion (Figures 1.4 E and F). Patches of diffuse aurora are often seen drifting eastward during the late expansion and recovery phases of substorms. The time scale for substorm recovery is typically one to several hours. In Chapter 4, a method for better quantifying the substorm recovery time scale is described.

The schematic diagrams shown in Figure 1.4 are statistical pictures of global auroral distributions during each substorm phase. However, they are consistent with the instantaneous, global auroral images obtained by Polar Ultraviolet Imager (UVI) over the course of a typical substorm. Figure 1.5 shows a sequence of UVI images for a substorm during on December 18, 1996. Although this example of a typical substorm fits the *Akasofu* [1964] description well, in both the observed auroral morphology and the time scales over which the event evolved, auroral behavior during substorms has a great deal of variability whose dependencies have not been adequately established. Indeed, one outstanding issue that will be addressed in this dissertation is whether or not all auroral intensifications are substorms and their associated phenomena which are described below.

The term *magnetospheric substorm* is also in common usage to emphasize the fact that auroral phenomenology is coupled to processes occurring in the magnetosphere [Brice, 1967; McPherron *et al.*, 1967; Coroniti *et al.*, 1968]. Near geosynchronous orbit, Cummings *et al.* [1968] noted that the magnetotail became stretched (i.e increase in the magnitude of $B_{\chi_{GSM}}$) prior to substorm onset. The tail field returns to a more dipolar configuration during the substorm expansion phase. This dipolarization of the magnetotail is accompanied by the earthward injection of electrons and ions with energies of a few tens to hundreds of keV during substorm expansion [Parks and Winckler, 1968; Arnoldy and Chan, 1969; DeForest and McIlwain, 1971]. Hereafter the terms *auroral substorm* and *magnetospheric substorm* are used interchangeably.

1.2.1 *Interplanetary pressure pulse driven aurora*

Auroral intensifications also occur during the interaction between interplanetary pressure pulses (IPP) and the magnetosphere. Interplanetary pressure pulses are identified as transient enhancements in solar wind ion density, sometimes carried by flow velocities as high as 1000 km s^{-1} [Kahler, 1992]. Pressure pulse driven auroral intensifications are characterized by a rapid expansion of the auroral oval on short time scales (tens of seconds to minutes) following the arrival of the solar wind perturbation at the dayside magnetopause. Recent case studies using auroral imaging by Polar UVI have generally shown that the auroral response to incident pressure pulses occurs much more rapidly than convection time scales in the magnetosphere [Spann *et al.*, 1998; Zhou and Tsurutani, 1999; Brittnacher *et al.*, 2000].

These observations have raised several key questions regarding the source regions of auroral precipitation during CME-magnetosphere interactions, as well as what processes may be operative during these events. How much direct access solar wind particles have to the auroral zone during CME passages is also unclear. Understanding the complex dynamics governing the response of the magnetosphere-ionosphere system to interplanetary pressure pulses is important because their interaction involves fundamental mechanisms of mass and energy transport from the solar wind into the magnetosphere. Zhou and Tsurutani [1999] have suggested that interplanetary pressure pulses may play an important role in triggering auroral substorms. The characteristics of pressure pulse driven auroral intensifications are examined in detail in Chapter 3. It is demonstrated that the auroral intensifications associated with the arrival of interplanetary pressure pulses are quantitatively different from those that occur in magnetospheric substorms.

1.2.2 *Seasonal variability in aurorae*

Up to now, we have discussed auroral dynamics on short time scales (~ 1 hour) associated with substorm activity and pressure pulse driven intensifications. On time scales longer than substorms there is a growing body of statistical evidence for strong

seasonal variations in the global structure of the aurora. A thorough review of these studies is given by *Newell et al.* [2001]. *Berko and Hoffman* [1974] studied the occurrence rate of field-aligned, 2.3 keV electron precipitation using measurements from the polar orbiting Ogo 4 spacecraft. They found that the electron precipitation at this energy was observed most often during the winter months at the highest altitudes of their measurements, near 900 km. *Berko and Hoffman* [1974] interpreted this as the result of localized electric fields parallel to the magnetic field being favored during the winter. Similarly, *Newell et al.* [1996] analyzed nine years of low altitude satellite particle measurements to show that intense, discrete aurorae are suppressed in sunlight.

Global images of the aurora have also been used to compare auroral intensities as a function of season. *Liou et al.* [2001] used Polar UVI images to show that the average energy of auroral electron precipitation is higher when the ionosphere is in darkness versus when it is sunlit. Likewise, *Petrinec et al.* [2000] found that the global pattern of auroral x-ray emissions exhibited a seasonal asymmetry whereby 2-12 keV auroral x-rays are observed to be more intense when the auroral oval is in darkness compared to when it is sunlit. *Shue et al.* [2001] explicitly examined the brightness of UV auroral emissions as a function of ionospheric Pedersen conductance. In support of *Newell et al.* [1996] and *Liou et al.* [2001] they found an anti-correlation between ionospheric Pedersen conductance and auroral brightness in the pre-midnight auroral oval. However, a positive correlation was found between conductance and auroral intensity for the morning sector, pre-noon auroral oval: the dayside aurora becomes more intense for higher ionospheric conductivity. *Liou et al.* [2001] and *Shue et al.* [2001] attribute this to enhanced number fluxes of (low energy) precipitating electrons in the dayside aurora during summer. This is consistent with the results of *Newell and Meng* [1988] who used DMSP particle data to show that the energy fluxes of precipitating ions and electrons in the cusp, likely originating from the magnetosheath, are higher near summer solstice than winter solstice by factors of 1.61 and 1.51, respectively. However, the causal connection between precipitation associated with the cusp and the dayside auroral region described by *Liou et al.* [2001] and *Shue et al.* [2001] has not been explicitly demonstrated and the relation between ionospheric conductivity and auroral

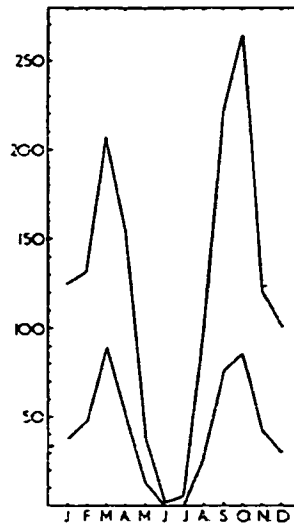


Figure 1.6: Monthly frequency of aurorae spanning 1911-1951 showing the equinoctial maxima of auroral activity. From *Störmer* [1955].

intensity on the dayside requires further study.

The hypothesis presented by the aforementioned studies is that quasi-static field-aligned potentials that accelerate electrons associated with discrete aurora are retarded when the density of cold, ionospheric plasma is enhanced when the ionosphere is sunlit. Plentiful cold, ionospheric photoelectrons present when the auroral zone is sunlit have a high degree of mobility in the field-aligned direction and are available to quickly neutralize any accelerating potentials. In this picture, the ionosphere is a principal agent in determining whether the aurora appears in discrete or diffuse forms.

In understanding seasonal variations in global auroral structure, one must also consider whether changes in the dipole tilt angle of the earth's magnetosphere play a role. Empirically, it is known that geomagnetic activity is greatest when the acute angle between the earth's dipole axis and the sun-earth line is near 90° as happens during the equinoxes [*McIntosh*, 1959]. Figure 1.6 shows the seasonal frequency of auroral observations in the northern (top curve) and southern (bottom curve) hemispheres between 1911-1951 from *Störmer* [1955]. Two peaks in auroral frequency are clearly seen during the equinoxes near March and mid-September. It is also well established ob-

servationally that a southward configuration (negative B_z) of the interplanetary magnetic field (IMF) leads to greater geomagnetic activity, presumably through enhanced magnetic energy transport on the dayside which drives more vigorous magnetospheric convection and storage of magnetic energy in the magnetospheric lobes. *Russell and McPherron* [1973] pointed out that the earth's magnetosphere encounters a southward IMF on average more frequently during the equinoxes than in the solstices. This has come to be known as the Russell-McPherron effect.

The extant studies in global auroral structure have generally neglected the dipole tilt and Russell-McPherron effects in favor of conductivity as the principal mechanism causing seasonal variations in the aurora. In one case though, *Lyatsky et al.* [2001] report that dipole tilt effects can only account for about 17% of the observed seasonal and diurnal variations in the AL index, a measure of the horizontal ionospheric currents associated with the aurora. They concluded that the seasonal and universal time variations of the AL index were best ordered by whether one or both nightside auroral zones (northern and southern hemisphere) were in darkness or sunlight. However, no direct observations of the aurora were included in this study which used a statistical auroral oval assumed to lie at 70° magnetic latitude.

1.3 Objectives of This Dissertation

In this dissertation, global auroral images are used in concert with *in situ*, low altitude particle measurements to study the effects of solar wind variations and seasonal variability in the ionosphere on electron precipitation during auroral substorms. The methods used in the quantitative analysis of UVI images are explained in Chapter 2. We describe the technique of inferring the precipitating electron energy flux and average energy from observations of the N_2 LBH auroral emissions. Particular care is taken to note that seasonal variations in the neutral atmosphere and uncertainties in the shape of the incident electron energy spectra can be neglected in estimating the precipitating electron energy flux and average energy by this method. An overview of the particle instruments on the FAST spacecraft is also included.

In Chapter 3 we present two case studies comparing observations of electron precipitation during a typical isolated substorm and a pressure pulse-driven auroral intensification associated with the initial phase of a magnetic storm. The global patterns of precipitating electron energy flux and average energy inferred from UVI images during the isolated substorm are shown to be markedly different from those observed during the pressure pulse-driven auroral intensification.

Our comparison of isolated substorms and pressure pulse-driven intensifications illustrates differences in the underlying physics behind these auroral phenomena. In the isolated substorm case, electron precipitation with average energies on the order of 10 keV is observed in the poleward region of the pre-midnight auroral oval and the equatorward portion of the post-midnight oval, following the global pattern of upward field-aligned currents *Iijima and Potemra [1978]*. We interpret these to be regions of discrete aurora. FAST electron measurements confirm that these regions are associated with discrete, inverted-V structures. Field-aligned acceleration of auroral electrons in the upward current regions is an essential aspect of the global aurora during isolated substorms. In contrast, the electron precipitation during the pressure pulse-driven intensification is less structured and has lower average energies. Simultaneous FAST electron observations show that the precipitation during the pressure pulse-driven intensification is diffuse with no evidence of field-aligned potential acceleration. The precipitating electron energy spectra in this case are Maxwellian-like with temperatures and densities consistent with plasma sheet electrons. Not all global-scale auroral intensifications are substorms despite the tendency to identify them as such from qualitative, visual observations.

Demonstrations of seasonal variation in the global structure of the aurora motivate further study into the role played by the ionosphere in auroral dynamics [*Newell et al., 1996; Liou et al., 2001*, and others described above]. The standard model of auroral phenomenology during substorms [*Akasofu, 1964*] was founded on ground-based observations obtained (by necessity) in darkness. The characteristics of substorms that occur when the ionosphere is sunlit have not been studied in great detail. Whether or not the *Akasofu [1964]* substorm description is applicable to events that occur in a

sunlit hemisphere has not been previously addressed.

This dissertation extends the results of previous statistical studies of ionospheric effects on the aurora by examining how seasonality affects global variations of auroral structure during magnetospheric substorms. With the exception of *Petrinec et al.* [2000] and perhaps implicitly *Shue et al.* [2001], the extant studies of seasonal auroral variation have made little mention of global auroral characteristics during equinoctial periods and have primarily focused on the seasonal extremes near each solstice. Our study will better represent the continuum of seasonal variability by examining global auroral behavior and substorm characteristics during both equinoctial and solstitial periods.

In Chapter 4 we use the hemispheric power derived from UVI images to quantify substorm phase and to investigate how the time scales of auroral substorm activity depend on both seasonal and solar wind factors. Using the substorm phases defined by the hemispheric power, a superposed epoch analysis is performed on the UVI observed auroral energy flux and average energy for substorms that occur during summer, winter, and equinox periods. *In situ* FAST particle measurements are used to examine the energy and pitch angle spectra of auroral electrons within each substorm epoch.

Substorms that occur during periods of southward interplanetary magnetic field (IMF) tend to have longer time scales than those occurring under northward IMF during all seasons. However, it is shown that substorm time scales vary most strongly with season while IMF orientation plays a secondary role. The characteristic decay time for substorm activity is roughly a factor of two longer when the nightside auroral zone is in darkness (winter and equinox) than when it is sunlit. We find that the longer time scale of substorms occurring in darkness is sustained by discrete auroral features associated with field-aligned potential drops and inertial Alfvén waves. These discrete structures exist for shorter time scales, if they are observed at all, during substorms that occur under sunlit conditions.

While the Russell-McPherron effect and variations in the earth's dipole tilt angle may be important for the occurrence frequency of substorms and auroral activity, the seasonal variations in global auroral structure during substorms described in this

work are most consistent with a mechanism involving ionospheric conductivity. The results presented in this thesis will enhance our understanding of substorm phenomena by bridging the gap between the microphysical description of the aurora and that describing the global changes in auroral morphology on substorm time scales (tens of minutes to hours). The seasonal behavior of auroral substorms described in this dissertation will also be important in guiding studies of auroral conjugacy, especially for future observations which may be able to describe the global auroral characteristics of both the sunlit and dark hemispheres simultaneously.

Chapter 2

INSTRUMENTATION

The primary data used in this study are global auroral images obtained from the Ultraviolet Imager (UVI) on the Polar satellite complemented by *in situ* particle measurements taken by the Fast Auroral Snapshot Explorer (FAST) spacecraft. When used in concert, we obtain simultaneously the global distribution of auroral FUV emissions and detailed information on the source auroral particle distributions (energy and pitch angle) at discrete points along the FAST trajectory through the region of the aurora observed by UVI.

The Polar spacecraft was successfully launched on February 24, 1996 into a $9.0 R_E$ by $1.8 R_E$ orbit with an inclination of 86° . With an orbit period of roughly 18 hours, the Polar spacecraft spends roughly nine hours during each orbit at altitudes greater than $6.0 R_E$ over the northern polar region, making it an ideal platform for imaging the aurora continuously over time scales much longer than the characteristic times associated with auroral phenomena such as substorms. Over time the line of apsides¹ will precess slowly at a maximum rate of 10° per year to higher latitudes, eventually passing over the north pole and then continuing southward to lower latitudes as shown in Figure 2.1.

The main spacecraft body of Polar spins at a rate of 10 RPM to accommodate most of the particles and fields instruments. The imaging experiments on Polar, however, are mounted on a despun platform that can be slewed about a single rotation axis to optimize the look direction of the imagers over the duration of a pass over the auroral zone.

¹The major axis of Polar's elliptical orbit

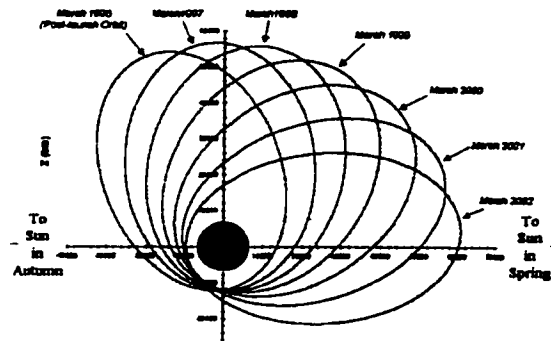


Figure 2.1: Evolution of Polar's orbit from its initial launch orbit through its extended mission.

2.1 Polar Ultraviolet Imager (UVI)

As one of three imagers aboard the Polar spacecraft (see *Frank et al. [1995]* and *Imhof et al. [1995]* for details regarding the other Polar cameras), Polar UVI plays a key role in the International Solar Terrestrial Physics (ISTP) initiative by allowing the study of the global scale structure of the aurora in simultaneous sunlit and dark conditions. *Torr et al. [1995]* provide a thorough description of the the optical system and mechanical design of the Polar UVI instrument. In the following we describe the features of the UVI instrument most important to this study.

2.1.1 Field of View

Global auroral imaging from space is a continual compromise between spatial coverage and spatial resolution: Greater global coverage generally translates into coarser spatial resolution since a larger area is projected on a fixed number of pixels. UVI's CCD detector comprises 200×224 pixels covering a circular 8° field of view. The spatial resolution is then $0.0363^\circ \times 0.0357^\circ$ per pixel in each respective spatial dimension. The top panel in Figure 2.2 shows the spatial resolution per pixel as a function of spacecraft altitude for the rectangular detector array. The diamonds (triangles) correspond to the short (long) dimension of the detector. Between $8 R_E$ and perigee near $1.8 R_E$

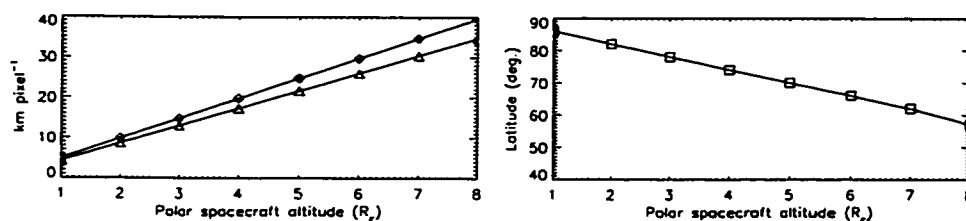
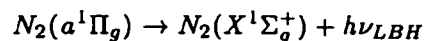
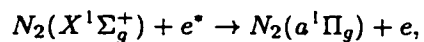


Figure 2.2: The top panel shows the spatial resolution in each dimension of the UVI CCD detector as a function of spacecraft altitude. The diamonds correspond to the short (200 pixels) dimension of the CCD array while the triangles are for the long (228 pixels) dimension. The bottom panel shows the extent of the global coverage provided by an 8° field of view as a function of spacecraft altitude.

the spatial resolution improves by about a factor of four. The bottom panel of Figure 2.2 shows the minimum geographic latitude that can be observed instantaneously over the pole as a function of Polar's altitude given its 8° field of view. Near apogee the field of view will be about 57° . Assuming that the equatorward edge of the auroral oval is near 60° magnetic latitude, global coverage of the auroral oval will be achieved for Polar altitudes greater than about $6 R_E$, which for the Polar orbit extends over roughly nine hours.

2.1.2 Filters

Polar UVI images the Lyman-Birge-Hopfield (LBH) emissions caused by electron impact excitation of molecular nitrogen (N_2). The process is summarized in the reactions:



The emission bands of the LBH system are shown in Figure 2.3. UVI also images the atomic oxygen (O I) multiplet lines at 130.4 nm and 135.6 nm. These oxygen emissions are created by electron impact excitation as well. Along with the N_2 LBH bands these are the most prominent FUV auroral emissions (excluding the very strong hydrogen Lyman- α emission at 121.6 nm).

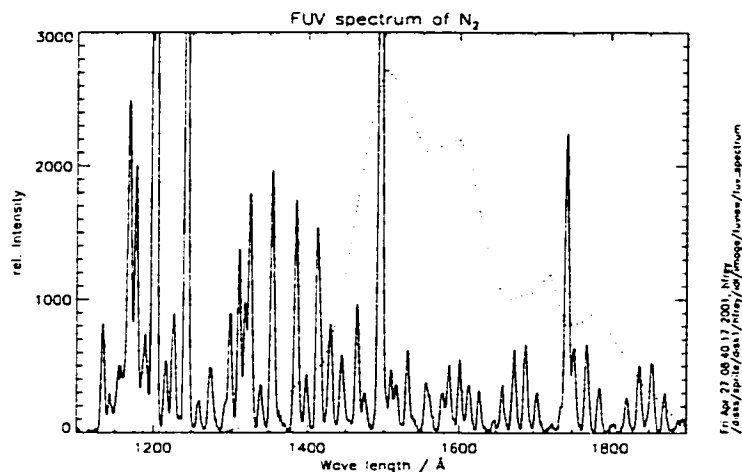


Figure 2.3: FUV N_2 LBH Spectrum

The passbands of each filter are shown in Figure 2.4. The y-axis shows the normalized transmittance in each channel. A more detailed description of the UVI filter characteristics is given by *Zukic et al.* [1993] and *Torr et al.* [1995]. The N_2 LBH bands are imaged in two separate bandpasses that cover the short and long wavelength regimes of these emissions. The bandpass of the LBH-long (LBHL) filter is roughly 160-180 nm with a peak near 170 nm. The LBH-short (LBHS) filter passes wavelengths between 140-160 nm, peaking at 150 nm. At the wavelengths covered by the LBHS filter the emissions are strongly affected by the O_2 Schumann-Runge continuum absorption. Thus the intensities observed through the LBHS filter are sensitive to the energy of the incident electrons causing the emissions: photons originating lower in the atmosphere, created by higher energy electrons, must pass through a thicker column of O_2 and suffer greater extinction before reaching the UVI detector. The emissions observed in the LBHL bandpass, on the other hand, are mostly longward of the O_2 Schumann-Runge absorption band and are negligibly quenched, only in the short wavelength portion of the LBHL bandpass.

The energy dependent electron transport process has been modeled by *Germany et al.* [1994a, b] using a two-stream energy deposition code. Here, the expected emis-

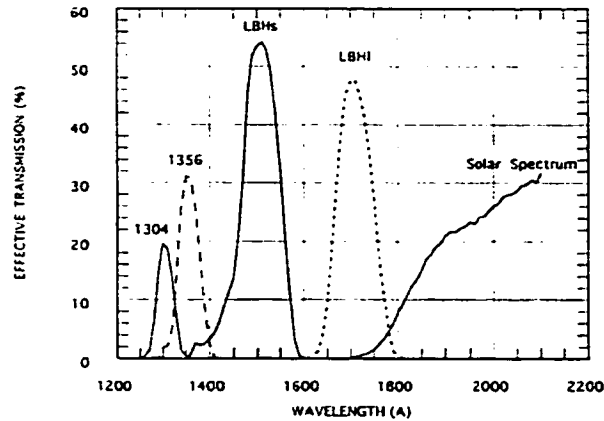


Figure 2.4: Passbands of UVI filters.

sion intensities (surface brightness) through the LBHs and LBHI bandpasses are computed given some known input energy spectrum of incident electrons. These results can be applied inversely to data, allowing one to infer the energy characteristics of the incident auroral electrons from LBHs and LBHI images. This technique as applied to the quantitative analysis of the UVI images is described below.

2.1.3 Polar Spacecraft Wobble

An error in the deployment of Polar's electric field booms induced a minor nutation in the spacecraft spin axis with a period of approximately 6 seconds. The stability of the despun platform on which UVI is mounted was thus compromised by this additional, unforeseen wobble motion. The spacecraft wobble degrades the spatial resolution of the UVI images by redistributing the observed photon flux along a line equivalent to roughly 10 pixels in the image plane, following the up and down motion of the despun platform. Thus a fixed point source observed by UVI would appear as two points separated by about 10 pixels. This situation can be readily demonstrated by star observations made by UVI as shown in Figure 2.5.

Efforts have been made to remove the wobble effect from the UVI images by post-processing the data with image reconstruction algorithms such as those used for as-

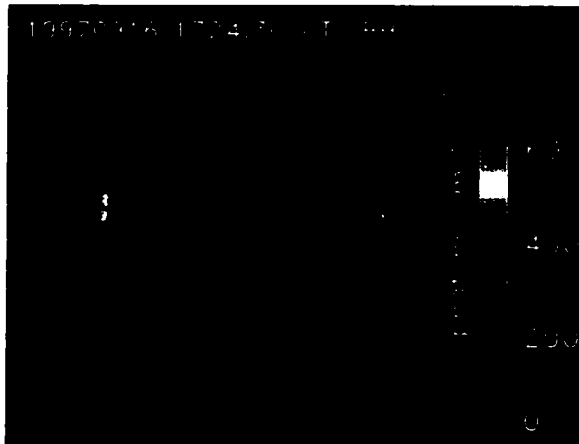


Figure 2.5: The wobble signature in UVI images is easily seen in observations of UV stars.

tronomical objects [Puetter, 1995]. However, due to computational expense the images presented throughout this dissertation have not been corrected for the wobble effect. Instead, the UVI images are spatially averaged into 0.5 magnetic local time (MLT) by 0.5° magnetic latitude bins prior to performing any quantitative analysis. While spatial resolution is sacrificed by not working at the per pixel level, the uncertainties in the parameters inferred from the UVI images are reduced when averaging over the spatial bins.

2.2 Quantitative Analysis of UVI Images

Qualitatively the FUV images of the aurora obtained by UVI are useful for purposes of monitoring the global spatial distribution of auroral activity. Many studies have used UVI images to give a global context for *in situ* ionospheric and magnetospheric observations and to aid in correlating auroral activity to processes in other regions in geospace. The real utility of the UVI images comes in the physical quantities that

can be extracted from the UV intensities. With some understanding of how the observed auroral emissions are created, properties of the source auroral particles can be inferred. These include the incident energy flux and the average energy of the source auroral precipitation. This also allows for the measurement of the energy deposition rate (hemispheric power) of auroral particles.

2.2.1 Energy Flux

In general the total energy flux carried by some particle species can be computed by

$$\epsilon = \int_{E_{min}}^{E_{max}} E f(E) dE \quad (2.1)$$

where $f(E)$ is the differential flux of the particles and E is the particle energy. The total energy flux, ϵ , has units of $\frac{\text{energy}}{\text{length}^2 \cdot \text{time}}$ which is equivalent to power per unit area. The upper limit of integration, E_{max} , is usually set to the maximum energy of a particle detector's measurement range. The choice for the lower limit of integration, E_{min} , may vary depending on which particle populations are to be included in the energy flux computation. *Robinson et al.* [1987] have previously discussed the selection of these limits of integration. For example, if one is interested in characterizing the primary auroral electrons of magnetospheric (i.e. plasma sheet) origin, secondary electrons and spacecraft photoelectrons, which are usually present in the data, must be excluded. In this case, values of 100-200 eV are usually chosen for E_{min} .

Electron transport modeling performed by *Germany et al.* [1990, 1994a, b] and *Richards and Torr* [1990] allows the incident electron energy flux to be estimated directly from the photon flux ($\text{photons cm}^{-2} \text{ s}^{-1}$) observed in the LBHI filter. The electron transport model used for this purpose determines the energy deposition of primary auroral electrons as a function of altitude and energy. The production rates of the N_2 LBH emissions resulting from these incident electrons are computed. The emission cross sections of *Ajello and Shemansky* [1985] are used in this computation. The O_2 absorption cross sections used in this model are those of *Ogawa and Ogawa* [1975]. Altitude profiles of the neutral atmosphere are specified by the MSIS-86 model [*Hedin,*

1987]. In this computation, the incident electrons are assumed to have a Gaussian energy distribution such as that in Equation 2.2 [Strickland *et al.*, 1983; Germany *et al.*, 1994a]. Here Q is the incident energy flux, W is a dimensionless parameter that sets the width of the Gaussian distribution, and E_c is the characteristic energy of the distribution. Maxwellian distributions like that given in Equation 2.3 have also been used for this purpose [Strickland *et al.*, 1989, for example]. Gaussian distributions are used to more closely represent the energy spectra of electrons over auroral arcs which are typically more narrow and have sharper peaks than Maxwellian-like distributions measured over regions of diffuse auroral precipitation [Boyd, 1975; McFadden *et al.*, 1987, for example].

$$f_{Gaussian}(E) = \frac{Q}{\pi^{1.5} E_c^2} e^{-\left(\frac{E-E_c}{W E_c}\right)^2} \quad (2.2)$$

$$f_{Maxwellian}(E) = \frac{QE}{2\pi E_c^3} e^{-\left(\frac{E}{E_c}\right)} \quad (2.3)$$

The auroral emissions observed through the LBHI filter are negligibly affected by O_2 absorption. The measured intensities in this channel have only a minor dependence on the average energy of the input electron distribution which is neglected in the following. Therefore, the intensity of the emissions observed through the LBHI filter are taken to be proportional to the incident electron energy flux since they have no significant attenuation mechanism. The observed photon fluxes ($\text{photons cm}^{-2} \text{s}^{-1}$) in the LBHI channel are converted to nadir surface brightness in units of Rayleighs. For the UVI instrument, the conversion factor between the observed photon flux to Rayleighs is $1 \text{ photons cm}^{-2} \text{s}^{-1} = 30.17 \text{ Rayleighs}$. The surface brightnesses are then converted into units of energy flux using the results of Germany *et al.* [1990, 1994a, b]. The proportionality between the column integrated surface brightness in the LBHI channel and incident energy flux ($\text{ergs cm}^{-2} \text{s}^{-1}$) is shown in Figure 2.6 and is roughly $110 \text{ Rayleighs} = 1 \text{ erg cm}^{-2} \text{s}^{-1}$. The conversion between photon flux and energy flux is then $1 \text{ photons cm}^{-2} \text{s}^{-1} = \frac{30.17}{110.0} \text{ ergs cm}^{-2} \text{s}^{-1}$. Ignoring the dependence on the average energy of the incident electron spectrum introduces a $\sim 10\%$ systematic uncertainty in the energy flux computation but yields the advantage of a simple linear proportionality

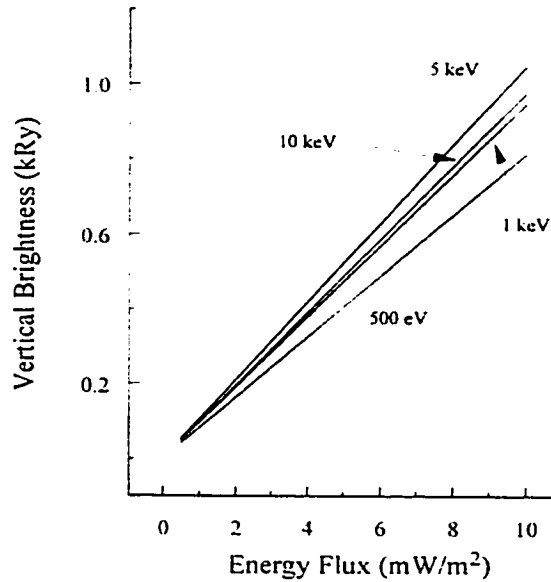


Figure 2.6: Column integrated surface brightness (kR) as a function of incident energy flux for varying electron energy spectra of mean energies as shown. From *Germany et al.* [1998]

between observed photon flux and energy flux.

2.2.2 Average Energy

In addition to the energy flux, another parameter that is useful for characterizing the population of precipitating auroral particles is the average energy. Given the differential flux for a particle species expressed as a function of energy, $f(E)$, the mean energy of the population is defined in general as

$$E_{ave} = \frac{\int_{E_{min}}^{E_{max}} E f(E) dE}{\int_{E_{min}}^{E_{max}} f(E) dE} \quad (2.4)$$

The denominator of Equation 2.4 is equivalent to the total number flux of particles (with units of $\frac{\#}{\text{length}^2 \cdot \text{time}}$). The numerator represents the total energy flux as defined in Equation 2.1. The factors that determine the limits of integration are the same as those discussed in Section 2.2.1.

As described in Section 2.1.2, the photon flux measured in the LBHs filter is inversely proportional to the energy of the incident auroral electrons. This provides a means with which to use the observed LBH emission intensities to infer the average energies of the electrons from the UVI images. As with the incident energy flux described above, the modeling results of *Germany et al.* [1990, 1994b] are used to infer the average energy of the source electrons from the observed LBH intensities. For the results given below, electrons of varying average energies and Gaussian energy distributions are input into a model atmosphere with a energy flux of $1 \text{ erg cm}^{-2} \text{ s}^{-1}$. The resulting column-integrated LBH emission intensities are then computed taking into account the effect of O_2 absorption and the LBHl and LBHs filter responses. In practice, the average energy of the incident electrons is computed from the LBHl:LBHs ratio rather than just the LBHs photon flux alone to normalize for varying levels of incident energy flux. The modeled mean energy versus LBHl:LBHs ratio is shown in Figure 2.7. The upper and lower bounds to the nominal curve (shown in bold) shows the expected errors in the inferred E_{ave} values given a 30% uncertainty in the LBHl:LBHs ratio.

Other researchers have discussed the use of other UV auroral emissions for the same purpose of inferring the average energy of electron precipitation [*Rees et al.*, 1988; *Steele et al.*, 1992; *Daniell and Strickland*, 1986]. For example, *Ishimoto et al.* [1988] investigated using the ratio of the atomic oxygen 135.6 nm emission to the LBH emission at 192.8 nm as diagnostics of precipitating electrons. *Germany et al.* [1990] also found that the OI 135.6 nm to LBH ratio was a very sensitive measure of incident electron average energy, varying by over an order of magnitude between E_{ave} values of 200 eV and 10 keV. However, we discuss below the disadvantages of using emissions that originate from two different constituents of the upper atmosphere.

2.2.3 Considerations of the neutral atmosphere

An important consideration in using the observed LBH emissions as diagnostics of electron precipitation is how variations in the neutral atmosphere with season and

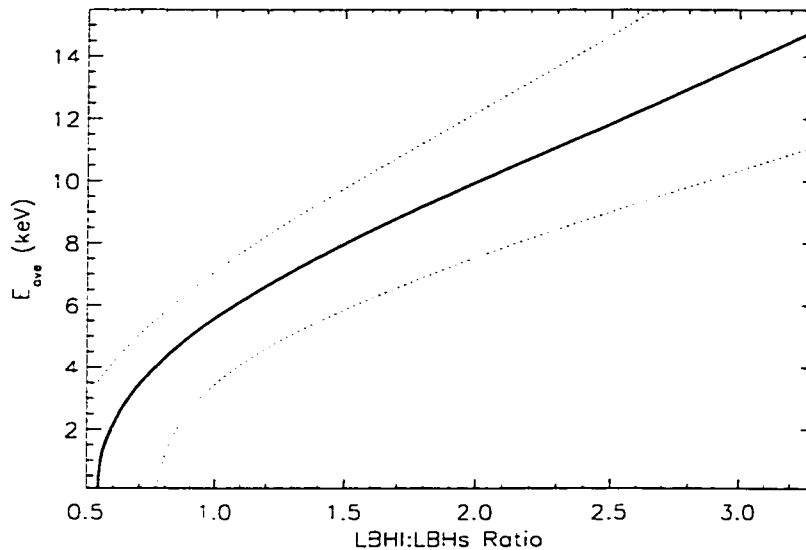


Figure 2.7: Mean energy versus LBHI:LBHs ratio. The dashed lines show the upper and lower limits for the uncertainties in the average energy values given a 30% error in the LBHI:LBHs ratio determination.

solar cycle affect the inferred energy flux and average energy values. The dominant neutral species at auroral altitudes (≥ 100 km) are O, N₂, and O₂. The most consequential variations to this study are those of the relative concentrations of N₂ and O₂. This is especially important for the analysis presented in Chapter 4 which examines seasonal variations in the characteristics of electron precipitation during substorms using the energy flux and average energy inferred from the UVI images. The sensitivity of modeled LBH emissions to changes in the neutral atmosphere was examined by *Germany et al.* [1990].

Variations in the inferred energy flux with changes in the neutral atmosphere is the simpler case to consider. The LBH emissions used to compute this quantity arise from only one atmospheric constituent (N₂) and are largely independent of variations in O₂. Variations in N₂ density with season or solar activity then only have the effect of raising or lowering the altitude at which the peak LBH emissions occur. *Germany et al.* [1990] found that doubling or halving the N₂ densities relative to O and O₂ at all

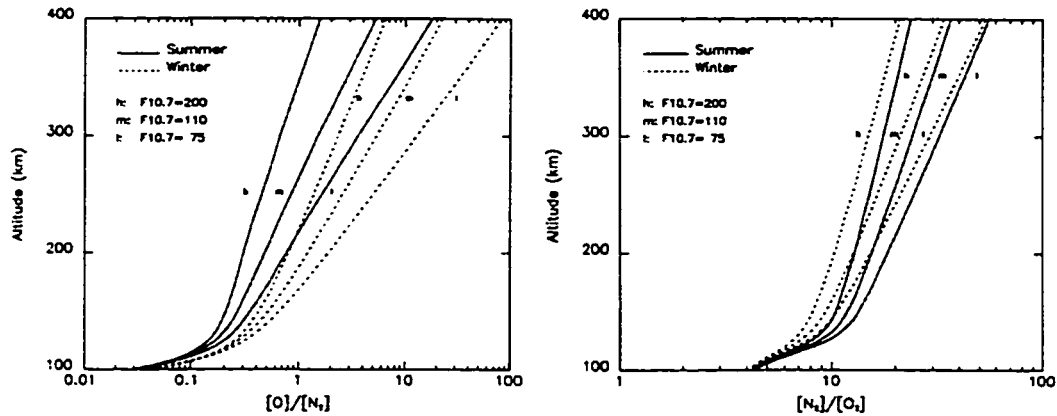


Figure 2.8: O:N₂ and N₂ : O₂ altitude profiles for varying seasons and solar activity levels. From *Germany et al.* [1990].

altitudes only changed the modeled, height-integrated emissions in the LBH bandpass (160-180 nm) by less than 20%. These variations are attributed to the competition between O and N₂ for interactions with precipitating electrons. This is only significant for low energy electrons below ~200 eV which deposit their energy at higher altitudes above 300 km where O concentrations become comparable to those of N₂.

In considering how variations in the neutral atmosphere affect the average energy computation, changes in the O₂ altitude distribution must be taken into account in addition to that of N₂. If the O₂ concentration relative to N₂ increases, a greater amount of absorption is affected on the shorter wavelength LBH emissions and the inferred average energies will be higher. Conversely, a decrease in O₂ relative to N₂ would result in lower inferred average energies.

Germany et al. [1990] studied how changes in the N₂ : O₂ ratio affect the average energies inferred from the LBH:LBHs ratio. Using the MSIS-86 atmospheric model, *Germany et al.* [1990] examined N₂ : O₂ altitude profiles as a function of season and F10.7 cm flux (Figure 2.8, right panel). For comparison, the O : N₂ altitude profiles are shown as well (Figure 2.8, left panel). It can be seen that the O to N₂ ratio can vary by almost an order of magnitude between winter and summer given the same level of solar activity. In contrast, the N₂ to O₂ ratio only varies by about a factor of two or three

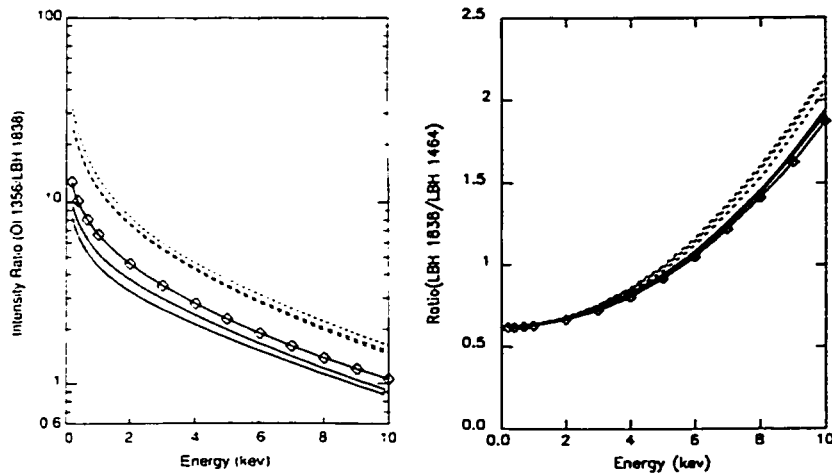


Figure 2.9: Variation of the OI 1356 Å:LBH 1838 Å ratio (left panel) and the LBH 1838 Å to 1464 Å ratio (right panel) with season and solar activity. From *Germany et al.* [1990].

above 150 km. The computed LBH_H:LBH_S ratio as a function of the incident electron average energy for different atmospheric states is shown in Figure 2.9. The dashed lines correspond to winter-time conditions and the solid lines are for summer. Each set of dashed or solid lines correspond to different levels of solar activity as represented by the F10.7 cm flux.

Germany et al. [1990] found that the LBH_H:LBH_S ratio varies by less than 20% with seasonal changes in the N₂ : O₂ ratio. *Germany et al.* [1990] also considered using the OI 1356 Å:LBH 1838 Å ratio as a diagnostic of average energy. The left panel in Figure 2.9 shows that the OI 1356 Å to LBH 1838 Å is very sensitive to the incident electron average energy, varying by about a factor of 10 between 200 eV and 10 keV. However, this ratio varies by a factor of three or four between summer and winter, reflecting the large variation in the O to N₂ ratio between seasons (Figure 2.9, left panel). This points out one disadvantage of using the ratio of auroral emissions arising from two different atmospheric species with large seasonal variations in relative abundance for estimating the average energy of incident auroral electrons: the average energies inferred from the OI 1356 Å:LBH 1838 Å ratio are highly dependent on the state of neutral

atmosphere. In contrast, the LBH:LBHs ratio is not very sensitive to compositional changes in the neutral atmosphere with season and solar cycle.

2.2.4 Effect of different electron distributions

There will also be some variation in the results of the average energy computation depending on one's choice of distribution when doing the electron transport modeling. This problem was investigated by *Germany et al.* [1994b] who compared the modeled column-integrated LBH emission intensities resulting from incident electrons with Gaussian versus Maxwellian energy spectra. *Germany et al.* [1994b] found that the modeled LBH emission intensities varied by less than 30% between input Gaussian and Maxwellian electron energy distributions. For the choice of energy distribution to be significant, the errors in the UVI data would have to be much less than 30% which is generally not the case.

2.3 Fast Auroral Snapshot (FAST) Explorer: Particle measurements

Six months after the launch of Polar (on August 21, 1996), FAST was placed into a highly elliptical 4175 km by 350 km orbit with an inclination of 83°. With an orbital period of 133 minutes, the FAST trajectory through the northern auroral zone is included in UVI's field of view at least once per Polar apogee pass. In these regions, high resolution measurements of energetic particles (electrons and ions), electric and magnetic fields, and plasma waves are obtained. An overview of the instrumentation on the FAST spacecraft is given by *Carlson et al.* [1998a]. A brief synopsis of the instrumentation on FAST most relevant to this study is given in the following.

The FAST data are used to reveal the detailed structure of the auroral regions imaged globally by UVI and are essential to this study as they allow for a more detailed physical interpretation of the UVI images. The FAST observations are also used to validate the energy flux and average energy of the precipitating auroral electrons derived from the UVI images. Since the line of nodes² of the FAST orbit precesses in time, the

²The line created by the intersection of the equatorial plane and the FAST orbit plane.

in situ FAST measurements are made in a wide range of latitudes, local times, and altitudes to complement the global auroral imaging provided by UVI.

2.3.1 Magnetospheric Particle Dynamics

In order to understand the FAST particle data it is first necessary to briefly review the basic dynamics of charged particles in the magnetosphere. In the presence of magnetic and electric fields in the magnetosphere, magnetospheric particles obey the Lorentz equation of motion (Equation 2.5).

$$m \frac{d^2 \vec{r}}{dt^2} = q \left(\frac{d\vec{r}}{dt} \times \vec{B} + \vec{E} \right) + \vec{F} \quad (2.5)$$

\vec{F} encompasses all non-electromagnetic forces including gravity. In a quasi-dipole magnetic field configuration such as that used to approximate the magnetic topology of the magnetosphere, solutions to Equation 2.5 describe particle trajectories that can be deconvolved into three basic types of motion. In the following we only describe two that are most relevant for auroral production.

At the shortest time scales, charged particles in the presence of a magnetic field undergo cyclotron motion as they gyrate about the field in a helical path. It is common to separate a particle's instantaneous velocity into two components: one parallel to the local magnetic field, v_{\parallel} , and one perpendicular to it, v_{\perp} . The angle between the particle's instantaneous velocity vector and the local magnetic field direction is defined as its *pitch angle*, α .

A charged particle undergoing cyclotron motion defines a current loop with a magnetic moment which can be written as

$$\mu = \frac{mv_{\perp}^2}{2B} = \frac{mv^2 \sin^2 \alpha}{2B} \quad (2.6)$$

μ is an invariant of the particle's motion so long as changes in the magnetic field occur on time scales much longer than the particle's cyclotron period. The motion of a charged particle in this regime changes in such a way as to conserve the magnetic flux enclosed by its cyclotron orbit. For example, if a particle's trajectory carries it into

a region where the magnetic field strength increases, its pitch angle, α (or v_{\perp}) must increase according to Equation 2.6 to keep μ a constant.

If the magnetic field is inhomogeneous and if the field converges in a certain region (such is the case for a dipole magnetic field used as a zeroth order approximation of the terrestrial field) the particle's pitch angle will move to 90° as the magnetic field strength increases according to Equation 2.6. As α approaches 90° , v_{\parallel} goes to zero. Furthermore, since there exists a gradient in B along the magnetic field direction in this geometry ($\nabla_{\parallel} B \neq 0$), there exists a force given by Equation 4.2 of *Parks* [1991] as $F_{\parallel} = -\mu \frac{\partial B}{\partial s}$ which acts in the direction opposed to that of the particle's parallel velocity causing the particle to be reflected after its v_{\parallel} goes to zero. Here s is a line segment along the field line. The point at which a particle is reflected by this force is known as its *mirror point*. If there exists another such point somewhere else along the field, the particle will bounce between each mirror point and is said to be in trapped orbit.

At some altitude where the magnetic field magnitude is B , the pitch angles of particles that will mirror at an altitude where the magnetic field is B_R is given by Equation 2.7. This expression is derived from Equation 2.6 by setting α at B_R to 90° and solving for α at B . If the mirror point is at a sufficiently low altitude the particle may interact with a constituent of the atmosphere and be lost, or precipitated, from that magnetic field (flux tube).

$$\sin^2 \alpha = \frac{B}{B_R} \quad (2.7)$$

$$\alpha = \arcsin \sqrt{\frac{B}{B_R}} \quad (2.8)$$

At the location where B is evaluated, particles with pitch angles less than α are lost to interactions with the atmosphere and are said to be in the *loss cone*. These are the particles that take part in the collisional interactions with the atmosphere that produce aurorae. A particle with pitch angle greater than α at the altitude where B is evaluated will mirror above the loss altitude and remain trapped on its flux tube assuming that its motion is adiabatic. The loss altitude is usually taken to be about 100 km. At geosynchronous orbit (near $6.6 R_E$ altitude) on the magnetic equator, the loss

cone is only about 3° wide. At various points along the FAST orbit, the width of the loss cone varies between roughly $25\text{-}50^\circ$ wide. For the FAST electron measurements shown in Chapters 3 and 4 the width of the loss cone is determined by Equation 2.7 at each data point where B is the magnetic field magnitude measured at the FAST spacecraft and B_R is the magnetic field magnitude at the ionospheric footprint location at 100 km altitude.

2.3.2 *Electrostatic Analyzers (ESAs)*

The advantages of using the FAST particle observations over those taken from other spacecraft contemporaneous with UVI are the continuous measurements of particle pitch angle distributions independent of the spacecraft spin and the much higher time resolution of the data. FAST employs 16 “top-hat” electrostatic analyzers (ESAs) to measure particles over the energy range of 4 eV to 30 keV for electrons and 3 eV to 25 keV for ions. The detector heads for each analyzer are placed in pairs on opposite sides of the spacecraft to achieve an unobstructed 360° field of view. Each ESA obtains high time resolution electron measurements every 1.7 ms in 16 pitch angle bins and electron or ion (EESA or IESA) distribution measurements over 32 pitch angle bins every 70 ms. The latter measurements are made using deflection plates which steer the field of view to automatically track the local magnetic field direction.

Chapter 3

A COMPARISON OF ISOLATED SUBSTORMS AND PRESSURE PULSE DRIVEN AURORAL ACTIVITY

The occurrence of auroral substorms appears trivial to identify from optical observations since the expansion and intensification of aurorae are usually the most conspicuous manifestations of this phenomenon. After all, the substorm framework originated from optical observations as described in Chapter 1. It may seem reasonable then to assume a one-to-one correspondence of auroral brightenings with the occurrence of substorms. However, we will show that this is an erroneous assumption. Synoptic scale auroral intensifications also occur in response to the arrival of interplanetary pressure pulses (IPP) associated with coronal mass ejections (CME) or magnetic clouds. Previous studies have suggested that these CME pressure pulses may even trigger auroral substorms [*Zhou and Tsurutani, 1999*, for example]. However, we shall see that the precipitation associated with these events have very different characteristics than auroral brightenings during substorms. We do not find evidence for the triggering of auroral substorms by incident CME pressure pulses.

The distinction between isolated substorms and pressure pulse driven intensifications is important because it illustrates underlying differences in the physics that create the large-scale auroral structure during these two phenomena. The appearance of discrete auroral forms during substorms as described by *Akasofu [1964]* points to a central role played by the auroral acceleration process between magnetospheric source regions of auroral particles and the ionosphere in these events. In contrast, observations of electron precipitation during pressure pulse driven intensifications reveal little evidence of auroral acceleration above the ionosphere; diffuse aurora dominates. In this case, the ionosphere acts as a passive sink for magnetospheric precipitation.

Over three hundred isolated substorms have been examined. An extensive statis-

Table 3.1: Interplanetary pressure pulse driven intensifications observed by Polar UVI. The universal times correspond to the initial brightening of the aurora.

| Date | UT | Comments | References |
|----------------|-------|--|--|
| Jan. 10, 1997 | 01:00 | CME, magnetic cloud event | <i>Fox et al.</i> [1998] and references therein |
| April 10, 1997 | 18:52 | CME event | |
| Oct. 1, 1997 | 00:50 | CME event | <i>Brittnacher et al.</i> [2000] |
| Dec. 10, 1997 | 05:29 | | <i>Zhou and Tsurutani</i> [1999] |
| May 2, 1998 | 05:10 | CME, magnetic cloud event | |
| Aug. 26, 1998 | 06:53 | CME, v_{sw} up to 1300 km s^{-1} | <i>Bale et al.</i> [1999], <i>Chua et al.</i> [2001] |
| Sep. 24, 1998 | 23:44 | CME event | <i>Moore et al.</i> [1999], <i>Russell et al.</i> [1999] <i>Winglee et al.</i> [2000] |
| Oct. 19, 1998 | | CME, magnetic cloud event | |
| June 28, 1999 | 05:11 | Brightening equatorward of dayside oval. | |
| Oct. 22, 1999 | 06:40 | During main phase of storm | |
| April 6, 2000 | 16:39 | Full-Halo CME event | |
| July 14, 2000 | 14:39 | X-class solar flare, CME | |

tical study of the UVI inferred precipitating electron energy flux and average energy observed during these substorms as a function of season will be presented in Chapter 4. We have examined the auroral response to a dozen interplanetary pressure pulse arrivals. A list of these pressure pulse driven events is given in Table 3.1. All of the pressure pulse events associated with coronal mass ejections (CME) precede magnetic storms. References are given to other studies that have examined these events. The isolated substorms and pressure pulse driven intensification described in the case studies that follow are representative examples that illustrate the key differences between these phenomena.

3.1 Isolated Auroral Substorms

The sequence of UVI images and keograms taken on December 18, 1996 show the spatial and temporal development of a typical isolated substorm (Figure 3.1). The

gap in the keograms between 05:53 UT and 05:56 UT is due to a shift of the despun platform on which the UVI instrument is mounted on the Polar spacecraft. Prior to the onset of the isolated substorm on December 18, 1996, the electron precipitation near local midnight (2200-0200 MLT) has average energies near 4.1 ± 2.7 keV with precipitating energy flux below $3 \text{ ergs cm}^{-2} \text{ s}^{-1}$ (Figure 3.1b). Throughout this isolated substorm we observe very little auroral activity in the dayside oval between 0900-1500 MLT where incident electron energy flux remains below $1.5 \pm 1.2 \text{ ergs cm}^{-2} \text{ s}^{-1}$. The large errors ($\geq 40\%$) in the inferred E_{ave} values prior to the onset of the substorm are due to the low counts (energy flux less than $3.0 \text{ ergs cm}^{-2} \text{ s}^{-1}$) in the UVI images.

The onset of this isolated substorm occurs between 05:30:36 UT and 05:33:40 UT and is seen in the 05:33:04 UT LBHI image as an enhancement in incident energy flux from 2.7 ± 1.6 to $19.2 \pm 4.4 \text{ ergs cm}^{-2} \text{ s}^{-1}$ within a limited local time region between 2300-2330 MLT. The mean energy of the precipitating electrons at the breakup location (between 2300 and 2330 MLT) increases to 14.6 ± 2.6 keV near the equatorward edge of auroral oval ($\sim 65^\circ$ MLAT) and 12.2 ± 1.6 keV at higher latitudes near 71° MLAT (Figure 3.1b, 05:32:44 UT E_{ave} image). The substorm expansion is marked by the poleward enhancement of auroral precipitation over an increasingly wider local time region around the onset location between 05:33 and 05:51 UT. The expansion of auroral activity following the substorm onset is readily seen in the midnight sector keograms for this event (Figure 3.1c, panels 3 and 5) which show elevated energy fluxes at increasingly higher magnetic latitudes between 05:33 and 05:51 UT. During the substorm expansion, higher energy electron precipitation with mean energies between 9.8 and 11.3 keV are observed throughout the breakup region between 2200 and 0030 MLT and 65° and 75° MLAT (Figure 3.1b, 05:35:49 UT E_{ave} image).

The E_{ave} images in Figure 3.1b show that the precipitating electron average energy is structured in local time and magnetic latitude during the expansion phase of this substorm. In the pre-midnight sector (2200-0000 MLT), precipitating electron energies are highest near the poleward edge of the substorm expansion while in the post-midnight sector (0000-0200 MLT) the opposite is observed, with the highest E_{ave} values near the equatorward portion of the oval. This pattern is seen between 1800

and 0600 MLT in the average energy images between 05:42-06:03 UT (Figure 3.1b) during the substorm expansion phase. In the pre-midnight sector (2200-0000 MLT) E_{ave} keogram, both incident electron energy flux and mean energy increase with latitude, indicating that the precipitation within the substorm expansion region hardens as it expands poleward between 05:33-05:50 UT (Figure 3.1c, panels 3 and 4). In the dusk sector (1700-1900 MLT) we also observe higher mean energies near the poleward boundary ($E_{\text{ave}} \gtrsim 12$ keV) than at lower latitudes (Figure 3.1b). In contrast, the electron precipitation in the post-midnight sector (0000-0200 MLT) has the highest mean energies near the equatorward boundary of the oval. From the substorm onset through the expansion phase, the average energy of electron precipitation is 11.8 ± 3.4 keV near 63° MLAT in the post-midnight region (Figure 3.1c, panel 6). Similarly, the dawn sector E_{ave} keogram (Figure 3.1c, panel 8) shows incident electron average energies of 11.9 ± 4.3 keV near the equatorward boundary of the oval ($\sim 66^\circ$ MLAT) which decrease with increasing latitude.

The westward surge of the substorm expansion region reaches 1900 MLT by 05:51:28 UT. From the UVI images between 05:36:08 and 05:51:28 UT we estimate the velocity of the westward surge to be 1.1 km s^{-1} along the auroral oval, which is consistent with previous optical observations [Akasofu *et al.*, 1969]. In the 1900-2100 MLT region a peak energy flux of $36.3 \pm 6.0 \text{ ergs cm}^{-2} \text{ s}^{-1}$ is observed near 74.5° MLAT. The most energetic electron precipitation during the substorm event is observed in this region with average energies inferred to be 14.3 ± 2.2 keV. This is also shown in the evening sector (2000-2200 MLT) E_{ave} keogram (panel 2), which shows a hardening of the precipitation mean energy to 14.4 ± 2.1 keV near the poleward boundary of the auroral oval between 05:41 UT and 05:53 UT when the westward surge of the substorm expansion enters this region. The black-colored pixels within the westward surge region in the 05:51:28 UT E_{ave} map are where some average energy values are excluded because they fell outside the range of values for which our analysis is appropriate. The westernmost region of the substorm expansion continues to have the highest levels of incident energy flux throughout this event, as can be seen in the 05:51:28 UT and 06:03:44 UT images (Figure 3.1a).

The increase in energy of the electron precipitation in the westward surge of a substorm has also been reported by *Rème and Bosqued* [1973] from *in situ* electron measurements obtained by a sounding rocket. They find that the flux of electrons between 5 and 30 keV greatly increased in the westward surge region while electrons fluxes at energies below 5 keV were relatively weak and stable. Defense Meteorological Satellite Program (DMSP) measurements of auroral precipitation within a westward surge showed enhanced fluxes of electrons above 20 keV [*Meng et al.*, 1978].

The hard electron precipitation ($E_{\text{ave}} \geq 10$ keV) observed in dawn sector of the average energy images for the December 18, 1996 event, (Figure 3.1b) is the result of substorm-injected electrons which drift eastward toward the morning side where wave-particle interactions lead to precipitation. The substorm injected electrons with the highest energies arrive first and are detected prior to those with lower energies. This effect is shown by the post-midnight (0000-0200 MLT) and dawn sector mean energy keograms (Figure 3.1c, panels 6 and 8). Electron precipitation with $E_{\text{ave}} > 11$ keV is first observed after the substorm onset near 05:33 UT in the post-midnight sector (panel 6). Precipitating electrons with similar mean energies then appear in the dawn sector E_{ave} keogram (panel 8) between 06:05 UT and 06:23 UT. The hardening of the electron precipitation in the morningside has been well established by balloon-borne measurements of auroral x-rays [*Barcus and Rosenberg*, 1966; *Parks et al.*, 1968].

In regions of discrete aurora E_{ave} parameter indicates the energy that electrons gain from passing through an electrostatic parallel potential [*Carlson et al.*, 1998b, for example]. Magnetospheric electrons accelerated downward by such potentials constitute regions of upward field-aligned current (FAC). The regions in which we infer average energies near 10 keV and above in the UVI observations for the December 18, 1996 substorm (Figure 3.1b) are consistent with the statistical pattern of upward field-aligned current of *Iijima and Potemra* [1978] for active periods ($|AL| > 100\gamma$) and we interpret these as discrete aurora. In the dusk and pre-midnight sectors (1800-0000 MLT) the band of electron precipitation with mean energies above 10 keV lies poleward of 70° MLAT as do the Region 1 upward FAC. In the post-midnight and dawn sectors (0000-0600 MLT) the Region 2 upward field-aligned currents are equatorward of 70°

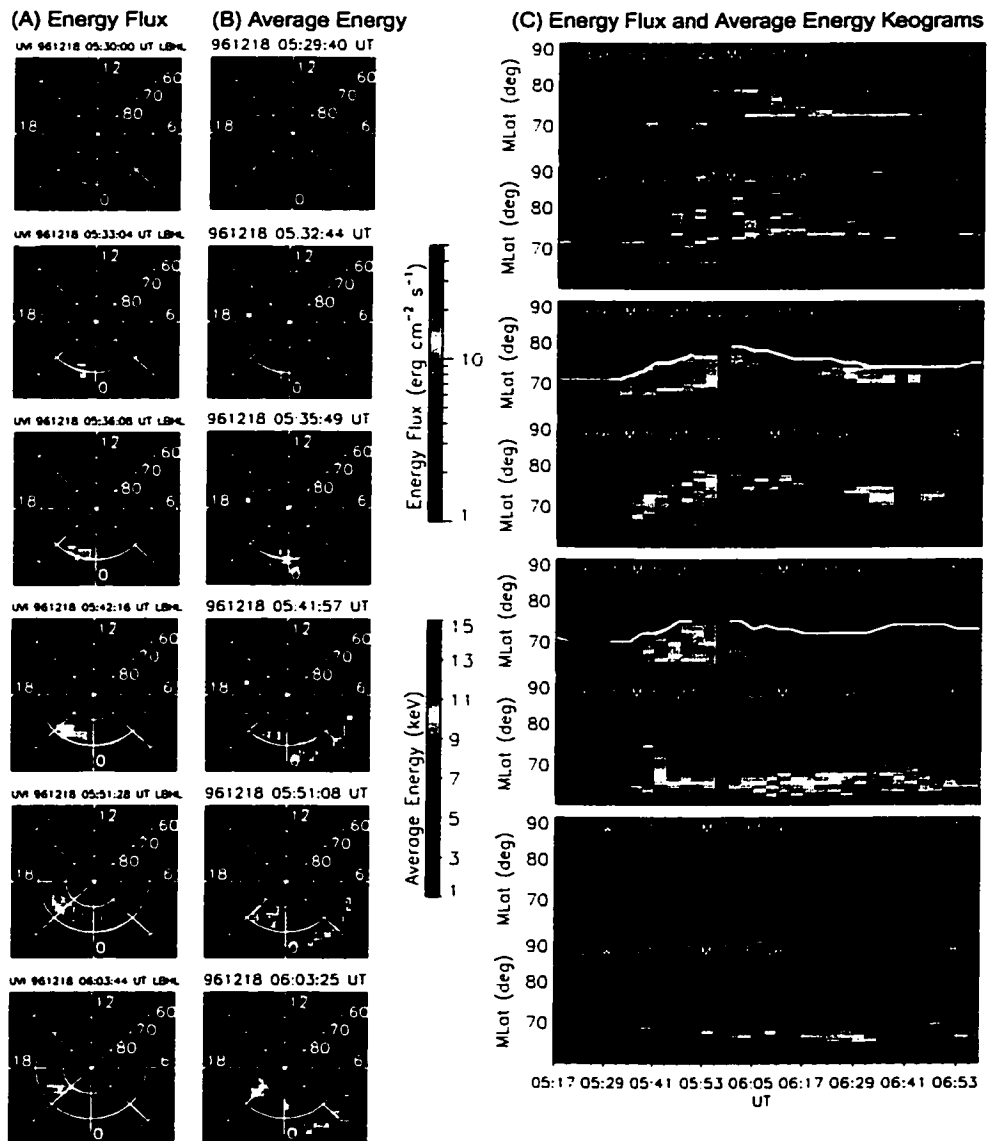


Figure 3.1: UVI observations of precipitating electron energy flux and average energy during an isolated substorm on December 18, 1996.

MLAT, which is where we observe the highest mean energy electron precipitation at these local times in the UVI E_{ave} images.

To support the assertion that the regions of enhanced average energy identified in the UVI observations are associated with discrete, accelerated precipitation, we examine coincident FAST and UVI observations during a substorm that occurred on January 30, 1998 (Figure 3.2). The energy flux and average energy images inferred from UVI are shown in the two left columns. The trajectory and footprint of the FAST spacecraft in the ionosphere is indicated in the energy flux images (left column). The right column shows FAST electron and ion energy-time and pitch angle spectrograms. As with the December 16, 1996 event, the UVI observations show that the poleward region of the pre-midnight (2100-2200 MLT) auroral oval is characterized by precipitation with energy flux above $10 \text{ ergs cm}^{-2} \text{ s}^{-1}$ and average energies near 9.0 keV. The FAST measurements of the downward electrons show that this region is associated with quasi-monoenergetic ($\sim 8 \text{ keV}$), inverted V-like precipitation that is characteristic of discrete aurora (top panel of FAST data). The average energies of the incident electrons derived from the UVI images agree well with those measured by FAST in this discrete auroral region. That there exists a field-aligned potential in this region accelerating the electrons downward is further corroborated by the observation of upgoing ion beams at energies of 7-9 keV as shown in fifth and eighth panels of the FAST data in Figure 3.2. Equatorward of 65° MLAT we see less structured electron precipitation in both the UVI and FAST data with average energies below 5.0 keV.

A common criticism of global auroral imaging is the inability to resolve individual discrete auroral arcs. While this is generally true of synoptic scale optical observations of the aurora, we have demonstrated that discrete and diffuse auroral regions can be discriminated when knowledge of both the average energy and energy flux of auroral electron precipitation can be derived from the auroral images. Our ability to identify discrete auroral regions over synoptic spatial scales and to quantify their energy characteristics as a function of both time and location using global auroral imaging enhances our ability to simultaneously describe both microphysical and macro-scale phenomena during substorms.

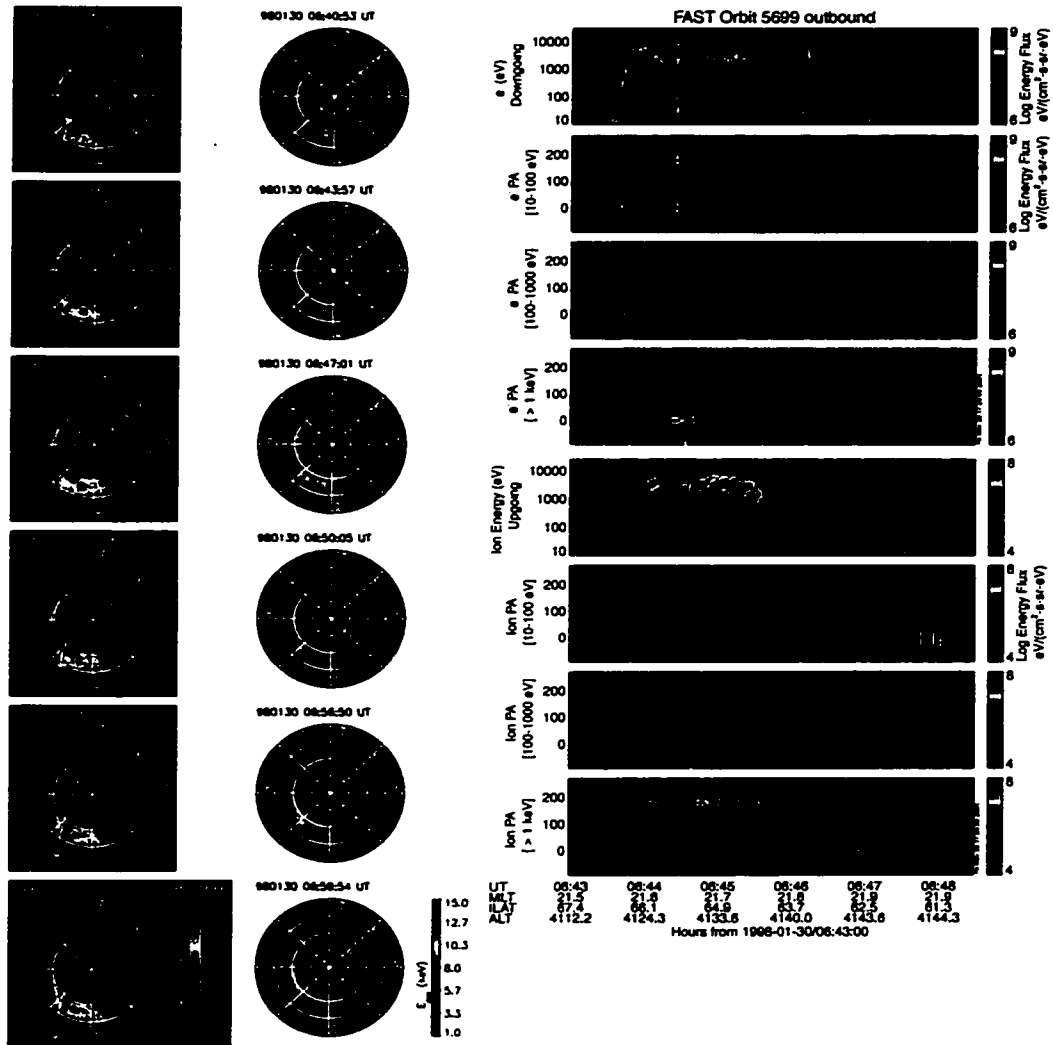


Figure 3.2: UVI and FAST observations for the January 30, 1988 substorm. The right column shows FAST electron and ion energy-time and pitch angle spectrograms. The two columns on the left show UVI derived precipitating electron energy flux and average energy.

3.2 Pressure Pulse Related Auroral Activity

We now wish to examine a class of auroral intensifications associated with the arrival of interplanetary pressure pulses and compare their characteristics with those of substorms described above. On August 26, 1998, at approximately 06:40 UT the Wind spacecraft encountered a CME-driven interplanetary shock at its upstream location of ($X_{GSE} = 117.0 R_E$, $Y_{GSE} = -21.6 R_E$, $Z_{GSE} = -7.6 R_E$). At this time, the solar wind dynamic pressure jumped from 2 nPa to above 10 nPa due to a four fold increase in proton density downstream of the shock and a jump in the solar wind velocity from about 450 kms^{-1} to above 650 kms^{-1} . This is shown in Figure 3.3 which gives a summary of the interplanetary conditions measured by Wind in addition to auroral and geomagnetic data during this magnetic storm event between August 25-27, 1998. The IMF magnitude increases by about a factor of three from 7 nT to 21 nT when Wind encounters the interplanetary shock. The IMF B_z component is initially strongly northward at about 15 nT. After about 09:30 UT on August 26 the IMF B_z component turns and remains predominantly southward throughout the main phase of the ensuing magnetic storm. The IMF B_x component is strongly negative (Earthward) during the initial Wind encounter with the interplanetary shock and remains so until about 10:00 UT on August 26. Further details of the *in situ* Wind observations of this interplanetary shock are given by *Bale et al.* [1999]. In Figure 3.3 the solar wind observations are propagated in time from the Wind spacecraft location to the dayside magnetopause as determined below.

In the following, we estimate the time delay between the arrival of the CME-driven, interplanetary shock at the dayside magnetosphere and the global auroral intensification observed near 06:53 UT. Using the empirical magnetopause model of *Petrinec and Russell* [1996], we estimate an equatorial magnetopause stand-off distance of about $7.8 \pm 0.2 R_E$ based on the solar wind conditions measured prior to the shock arrival by the Wind spacecraft (Figure 3.3). *Bale et al.* [1999] estimate a shock velocity of 1300 kms^{-1} and a shock normal direction of ($\hat{x}_{GSE} \approx -0.93$, $\hat{y}_{GSE} \approx -0.09$, $\hat{z}_{GSE} \approx 0.36$). Assuming these properties, we estimate the transit time of the interplanetary shock between the

Wind spacecraft location and the dayside magnetopause at the stand-off distance given above to be about 9 ± 1 minutes. This gives an arrival time of the pressure pulse at the magnetosphere between 06:48-06:50 UT.

The fourth panel of Figure 3.3 shows the D_{st} values throughout this event. At the arrival of the pressure pulse near 06:50 UT one sees a positive excursion of the D_{st} curve to values near 50 nT caused by the compression of the magnetosphere, a classic signature of a storm sudden commencement (SSC). D_{st} reaches a minimum value near -150 nT on August 27, 1998. The bottom two panels of Figure 3.3 show the UVI derived hemispheric power (energy flux integrated over the area of the auroral oval, described in more detail in Section 4.1) and a keogram (auroral intensity as a function of magnetic latitude and time for a specified local time sector) for the 2200-2400 MLT region. The keogram shows a strong auroral intensification associated with the arrival of the solar wind pressure pulse and the onset of the SSC. Intense auroral activity continues throughout this magnetic storm. As an aside, note that the equatorward boundary of the auroral oval tracks the D_{st} index throughout this storm event. This effect has been described by *Akasofu and Chapman* [1963]; *Schulz* [1997]; *Yokoyama et al.* [1998].

The Polar UVI observations of the auroral response to this interplanetary shock are given in Figure 3.4 and are shown in the same format as Figure 3.1. The data drop-out in the keograms between 07:50-08:10 UT is caused by the auroral oval moving out of the UVI field of view prior to a change in the Polar despun platform orientation.

Prior to the arrival of the interplanetary shock, we observe pre-existing activity in the 1800-2400 MLT sector with a mean energy flux of 5.3 ± 2.3 ergs $\text{cm}^{-2} \text{s}^{-1}$ and average energies between 5.7-9.7 keV of (Figure 3.4). This is the remnant of a previous auroral intensification that occurred between 04:50-06:00 UT (not shown). There is no significant motion of the auroral oval at all local times between 06:22-06:50 UT with incident energy flux and average energy values in the dayside aurora (0600-1800 MLT) mostly below 3.0 ergs $\text{cm}^{-2} \text{s}^{-1}$ and 6.0 keV, respectively. A localized region of higher auroral activity is observed at 06:50 UT near 1500 MLT with a mean energy flux of approximately 2.9 ± 1.7 ergs $\text{cm}^{-2} \text{s}^{-1}$. This region has been identified by previous studies as one of two maxima of dayside auroral activity [*Cogger et al.*, 1977; *Liou*

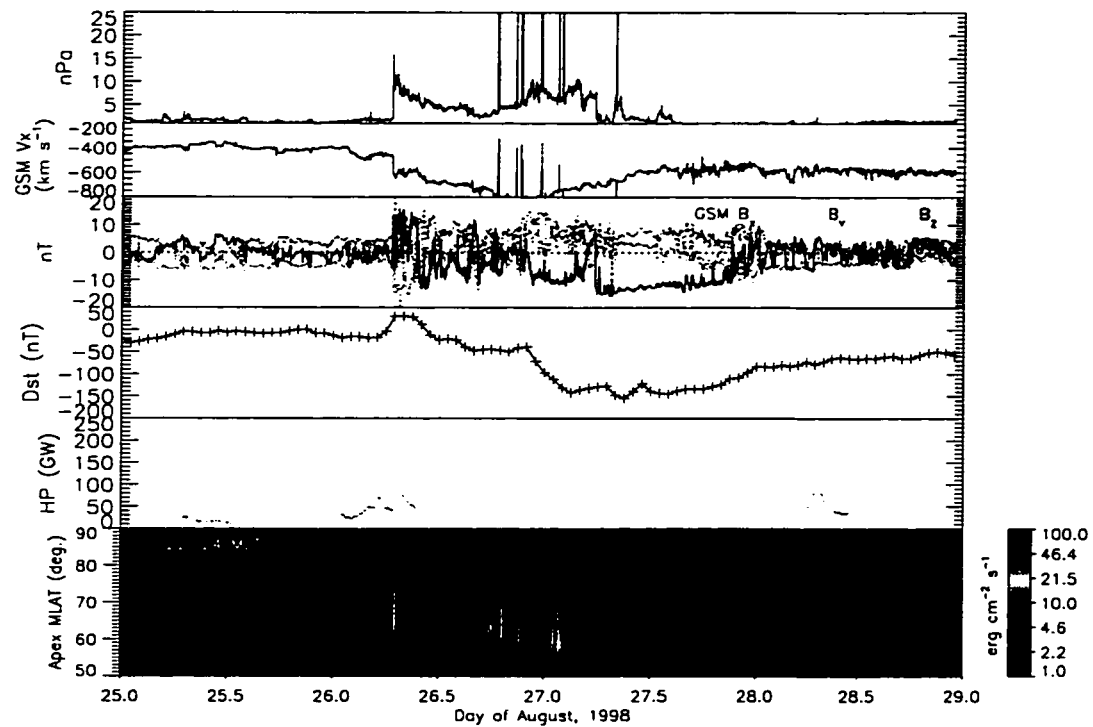


Figure 3.3: Solar wind and auroral zone data on August 25-27, 1998. Top panel: Solar wind dynamic pressure. Second panel: Solar wind x-component (GSM) velocity. Third panel: Interplanetary magnetic field in GSM components. Fourth panel: D_{st} . Fifth panel: Hemispheric power computed from UVI LBHI images. Bottom panel: Keogram derived from LBHI images in the 2200-2400 MLT sector.

et al., 1997, 1999].

The initial brightening of both dayside and nightside auroral zones near 06:53 UT occurred no later than five minutes following the arrival of the solar wind pressure pulse at the dayside magnetopause. The auroral response to the incident pressure pulse occurred on Alfvén wave time scales rather than convection time scales (tens of minutes) in the magnetosphere. At the location of the initial dayside auroral brightening between 1200-1500 MLT, incident energy flux increased by a factor of five to $8.8 \pm 2.9 \text{ ergs cm}^{-2} \text{ s}^{-1}$ with average energies between 4.6-7.7 keV (Figure 3.4a, 06:53:56 UT image). Another feature to note at this time is the transient brightening equatorward of the dayside auroral oval between 06-18 MLT at magnetic latitudes less than 70° . The energy flux in this region equatorward of the dayside oval has a maximum of $15.8 \pm 4.0 \text{ ergs cm}^{-2} \text{ s}^{-1}$ and average energies slightly higher than that in the main oval with values of 5.9-8.4 keV (Figure 3.4b). This feature persists equatorward of the post-noon auroral oval with incident energy flux of $7.3 \pm 2.7 \text{ ergs cm}^{-2} \text{ s}^{-1}$ until after the 06:57:00 UT image. The precipitation in the pre-midnight sector between 1800-2300 MLT intensifies with mean energy flux values of $9.6 \pm 3.1 \text{ ergs cm}^{-2} \text{ s}^{-1}$ and average energies of 10.4-12.5 keV between the 06:50:52 UT and 06:53:56 UT images (Figure 3.4a). This enhancement in incident energy flux in the pre-midnight sector is greater than three standard deviations above the mean energy flux measured in the pre-existing activity in this region prior to the arrival of the pressure pulse.

The spatial and temporal evolution of auroral activity in response to a solar wind pressure pulse is distinct from that observed during isolated substorms. The most distinguishing feature is the latitudinal expansion of the auroral oval and enhancement of incident energy flux at *all* local times rather than within a limited longitudinal region as in the isolated substorm described above. This can be seen by comparing the 06:50:52 UT and 06:53:36 UT images in Figure 3.4a which show a global enhancement in auroral activity. The global expansion of the auroral oval following the interplanetary shock arrival is further demonstrated by the energy flux keograms shown in Figure 3.4c (odd numbered panels).

In contrast to isolated substorms, the precipitating electron energy flux at high lat-

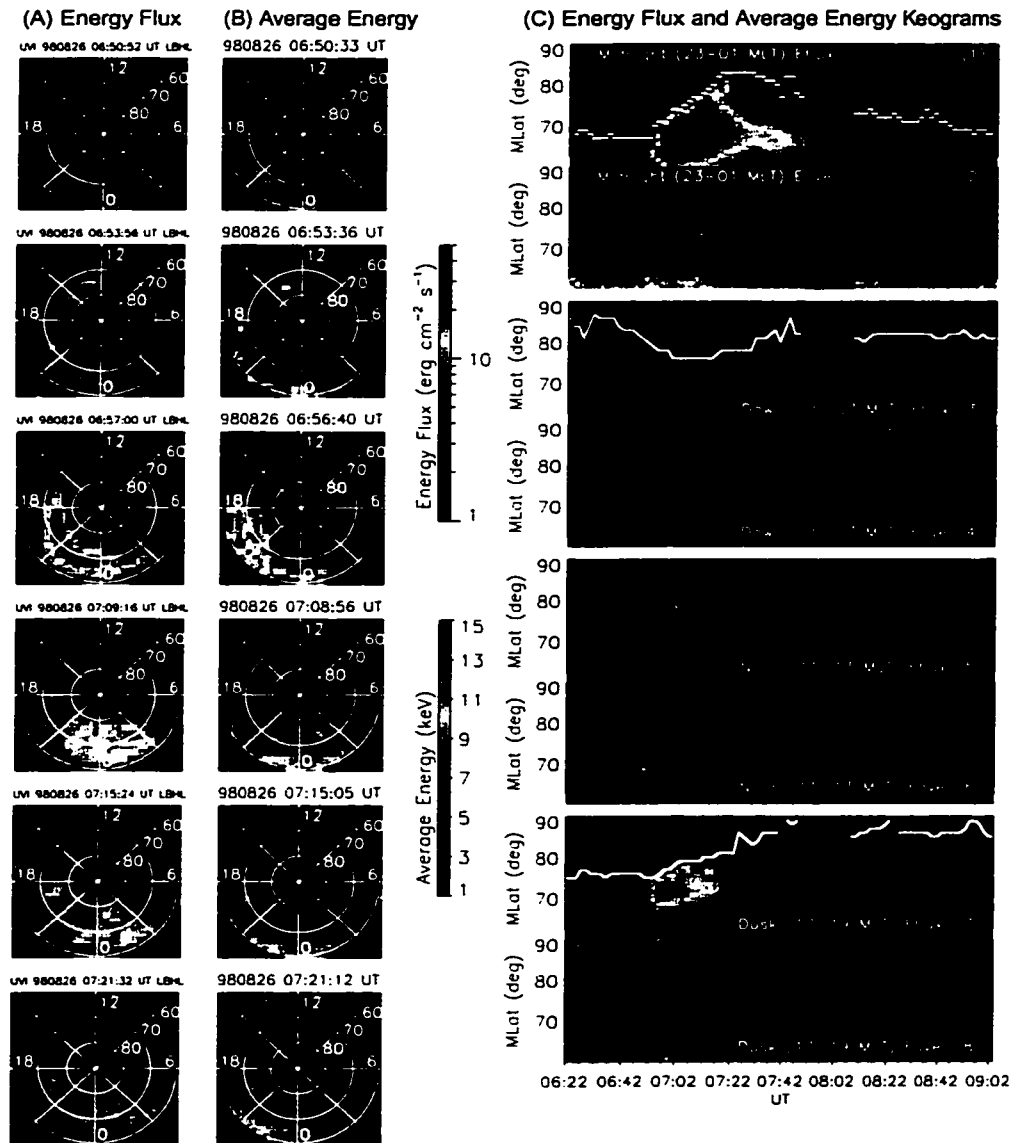


Figure 3.4: UVI observations of precipitating electron energy flux and average energy for August 26, 1998 CME event.

itudes and in the polar cap is significantly greater during this pressure pulse driven event. The electron precipitation following the arrival of the interplanetary pressure pulse was observed at mean energies below 7 keV poleward of 70° MLAT. The response of the high latitude auroral oval in the dusk (1700-1900 MLT) and dawn (0500-0700 MLT) sectors following the pressure pulse arrival is asymmetric. The UVI images between 06:54-06:57 UT show that the increase in auroral precipitation at high latitudes initially occurs in the dusk and pre-midnight auroral oval, expanding eastward toward the dawn sector, as well as broadening in latitude at all local times by 07:09:16 UT (Figure 3.4a). The dawn sector of the auroral oval is observed to shift slightly equatorward from 83° MLAT to 77° MLAT following the pressure pulse arrival, where it remains until 07:25 UT (Figure 3.4c, panel 3). No westward surge-like feature is observed during this pressure pulse driven intensification as is typically seen during substorms.

The auroral oval is much less structured at the resolution of the UVI images during this pressure pulse related intensification than during isolated substorms. The E_{ave} maps in Figure 3.4b between 07:08:56-07:21:12 UT show that the electron precipitation across the nightside auroral zone between 70-80° MLAT and 1800-0600 MLT has average energies between 4.5-7.1 keV. Within this region, the only structures that appear are two localized patches near local midnight at 72° MLAT with slightly higher mean energies between 8.6-10.8 keV (Figure 3.4, 07:09:18 UT image). These patches are coincident with localized enhancements in the incident energy flux. The average energy of the electron precipitation decreases to values ranging between 3.2-5.0 keV poleward of 80° MLAT at all local times.

The unstructured, diffuse nature of the electron precipitation during this pressure pulse related event is further supported by the simultaneous FAST electron measurements shown in Figure 3.5 for orbit 7954. The top three panels show pitch angle-time spectrograms for the energy ranges 10-100 eV, 100-1000 eV, and ≥ 1 keV respectively. The fourth panel shows the energy-time spectrogram for precipitating electrons (electrons in the loss cone at the FAST spacecraft, which is shown to be 34° wide). The corresponding UVI images with the FAST spacecraft position label are shown at the

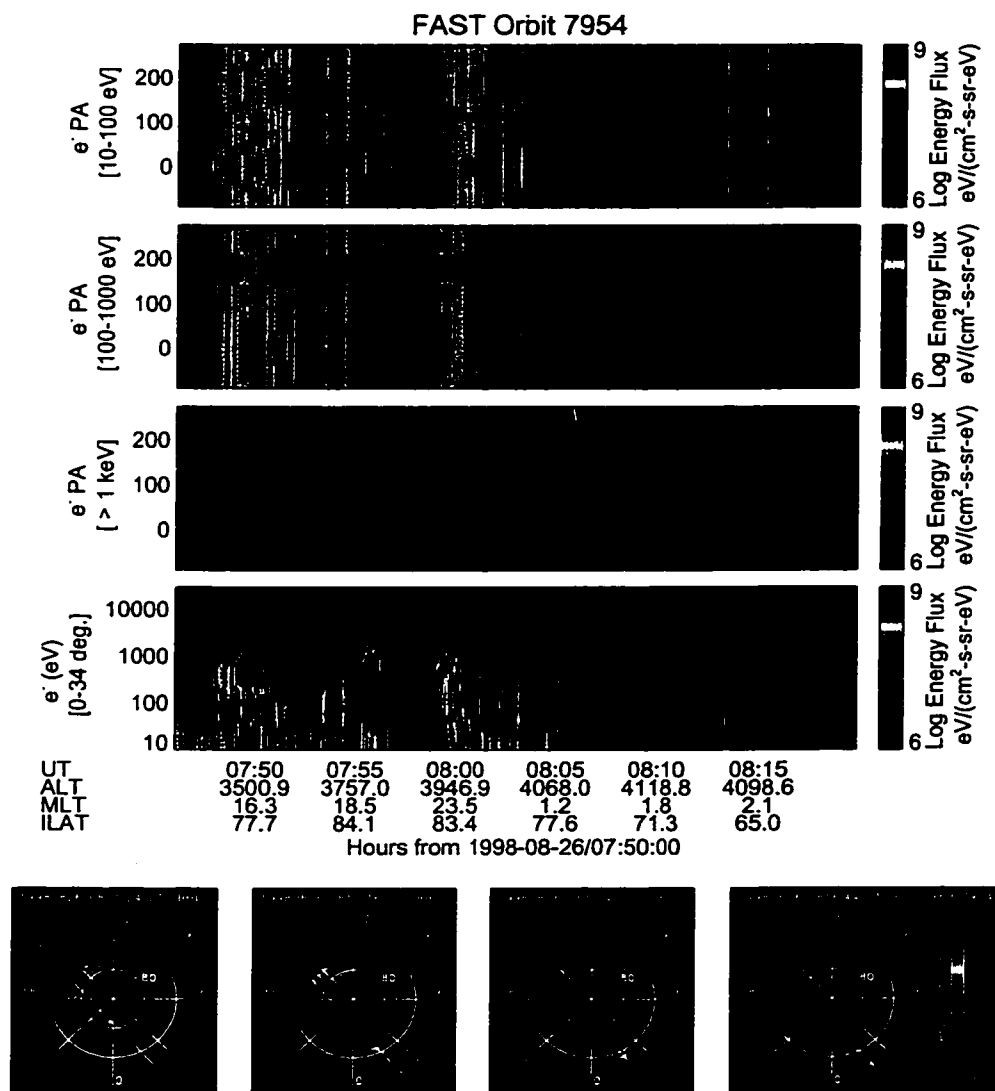


Figure 3.5: FAST electron pitch angle and energy-time spectrograms for the August 26, 1998 pressure pulse event (Orbit 7954). UVI images with the trajectory of the FAST ionospheric footprint are shown below.

bottom. The FAST data show unstructured diffuse precipitation throughout the post-midnight region of the auroral oval, consistent with the images shown below. The FAST pitch angle spectrograms for energies above 1 keV show isotropic distributions outside of the loss cone which can be seen around 180° pitch angle. Little indication of auroral acceleration is shown throughout the bulk of the nightside aurora except for a localized region just after 07:55 UT. We find that this corresponds to a transpolar arc feature that can be seen in the 08:01:24 UT UVI image.

Further evidence for the lack of field-aligned acceleration during this event comes when we examine the energy spectra in detail as shown in Figure 3.6. The pitch angles for each energy spectra shown are indicated to the right of each plot. The ordinate value of each spectrum is in units of $\#/(cm^2 - s - sr - eV)$. The black, dashed-lines in each plot show fits to the energy spectra using a power law plus a Maxwellian distribution (Equation 2.3). The modeled distributions show excellent fits to the observed energy spectra. The power law component dominates at energies below 300 eV. We interpret these as secondary electrons from the ionosphere and spacecraft photoelectrons *Heikkila [1970]; Frank and Ackerson [1971]; Evans and Moore [1979]*. The derived densities near $0.22 cm^{-3}$ and temperatures between 1.2-2.5 keV from the Maxwellian fit are characteristic of plasma sheet-like electrons. As FAST travels from high to low magnetic latitudes (Figure 3.5) or equivalently from higher to lower L-shells, the electron temperature is seen to increase (Figure 3.6).

In Figure 3.7 the UVI inferred precipitating electron average energies are compared with those measured directly by FAST over the morning sector oval between 0100-0200 MLT. The grey line shows the average energy of the downward going electrons (0-30° pitch angle) between 300 eV and 30 keV as computed from Equation 2.4. In selecting 300 eV as the lower limit of integration, we have chosen to include mostly plasma sheet-like electrons in computing the FAST mean energy values shown in Figure 3.7. The upper integration limit of 30 keV is determined by the highest energy detected by the FAST electrostatic analyzers. The FAST E_{ave} values are averaged over 40 seconds as shown by the black trace in Figure 3.7. Over this time interval, the FAST spacecraft traverses a distance of about 200 km near apogee. This is comparable to the size of the

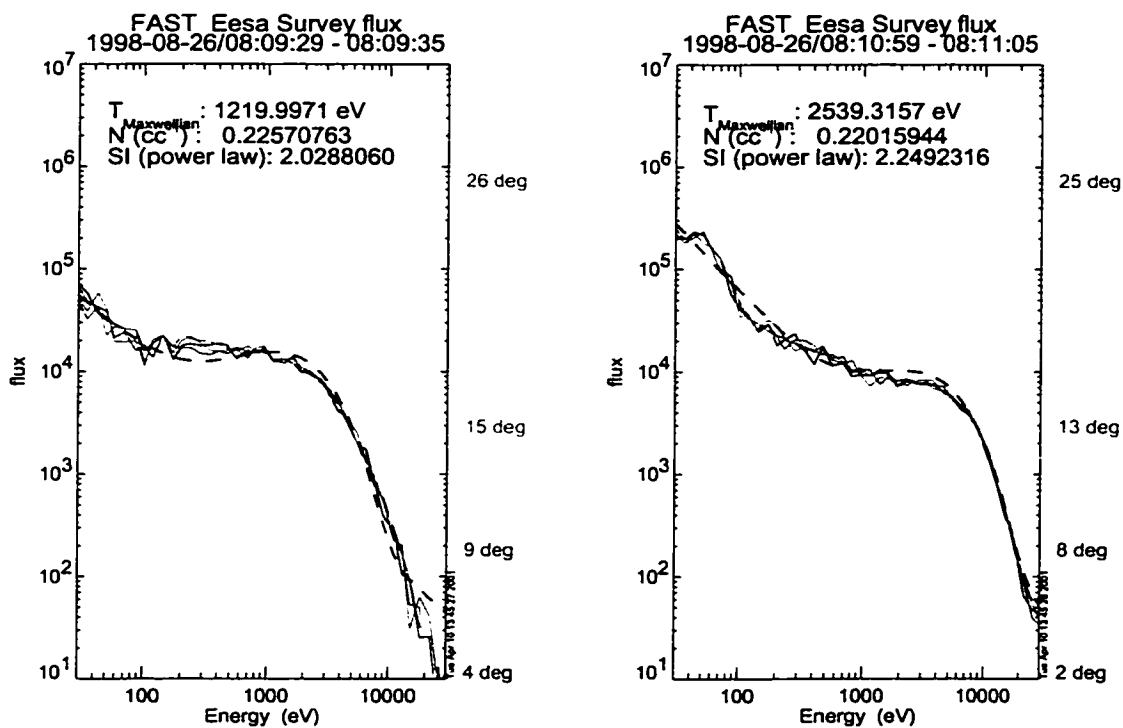


Figure 3.6: Electron energy spectra at the pitch angles indicated on the right side of each plot for the August 26, 1998 pressure pulse event. The energy spectra are modelled by a power law plus a Maxwellian distribution. The densities and temperatures of the modelled Maxwellian components are consistent with plasma sheet electrons. The ordinate values are in units of $\#/(cm^2 - s - sr - eV)$.

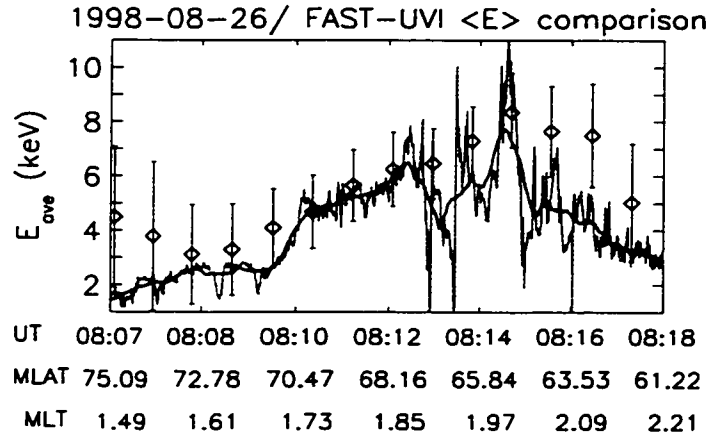


Figure 3.7: A comparison of UVI and FAST derived mean energy values for the August 26, 1998 pressure pulse event. The average energy of the precipitating electrons measured by FAST are shown by the grey line. A 40 second average of the FAST E_{ave} values is shown by the black trace. The data points (diamonds) are UVI derived E_{ave} values along the FAST trajectory

MLT-MLAT bins used in the UVI E_{ave} computation. The data points in Figure 3.7 are the UVI derived E_{ave} values along the FAST trajectory.

The precipitating electron average energies inferred from UVI are consistent with those measured by FAST, following a similar profile in latitude. However, the UVI E_{ave} values are systematically higher. As FAST moves equatorward from 75° MLAT to 71° MLAT, the average energy of the precipitating electrons gradually increases from about 1.5 keV to 2.5 keV. The UVI estimated E_{ave} values in this region are higher, increasing from 3.0 ± 1.9 keV at 74° MLAT to 3.4 ± 1.3 keV at 71° MLAT. The agreement between the FAST and UVI average energy values improves between 68-70° MLAT as both FAST and UVI show the mean energy of the electron precipitation increasing from about 5 keV near 70° MLAT to 6 keV at 68° MLAT. The 7.7 keV peak in the mean energy measured by FAST near 65.5° MLAT is not resolved by UVI. Instead, the UVI average energy profile shows a broader peak between 63-67° MLAT with a maximum value of 8.6 ± 1.9 keV. Equatorward of 63° MLAT, the average energies measured by FAST decrease below 4.0 keV. Near the equatorward portion of the FAST trajectory

(62° MLAT), the mean energy derived from UVI also decreases with a value of 4.9 ± 2.1 keV.

When comparing the FAST and UVI derived mean energies, we find that the UVI E_{ave} values are generally overestimated. We have considered whether the average energy signatures of the two events discussed above, particularly at the substorm onset and immediately following the pressure pulse arrival, are exaggerated by computing LBHL:LBHs ratios from images taken at different times during very dynamic auroral activity. *Germany et al.* [1998] point out that the mean energies derived from the UVI images can be inaccurate in situations where the aurora is changing rapidly between two UVI images, especially near boundaries of the auroral oval. However, the aurora is not very dynamic during this period as shown by the UVI keograms in Figure 3.4c between 08:07 UT and 08:18 UT. No significant auroral boundary motions are seen during this period when we compare the FAST and UVI E_{ave} observations.

The discrepancies between the FAST and UVI latitude profiles of E_{ave} values can be accounted for, in part, by the differences in spatial scales over which the E_{ave} values are determined between FAST and UVI. The UVI-derived mean energies are computed over 1.0° MLAT \times 0.5 MLT spatial bins while the FAST E_{ave} values are point measurements that only sample a portion of the morning sector oval observed by UVI. Moreover, the scale size of the auroral structures that we can resolve with the coarse spatial resolution of the UVI binned pixels (in MLT-MLAT) is at least two orders of magnitude larger than that which can be discerned with the FAST measurements. The UVI average energy estimation is also affected by the wobble of the Polar spacecraft (See Section 2.1.3. While the MLT-MLAT binning of the UVI images averages out the effects of the wobble, the regions of the images where lower photon fluxes are measured may have larger errors due to the wobble than in brighter portions of the images. Poleward of 71° MLAT where the UVI-derived mean energies are overestimated in comparison to the *in situ* FAST E_{ave} values (Figure 3.7), the auroral emissions measured by UVI decrease rapidly with increasing latitude (with an equivalent energy flux below $4.0 \text{ ergs cm}^{-2} \text{ s}^{-1}$) as shown in the midnight sector keogram for this period (Figure 3.4c, panel 1).

The degree to which the FAST and UVI average energy values agree also depends upon the limits of integration one uses when computing the mean energies via Equation 2.4. However, since the uncertainties in the UVI mean energy estimates are about 30% for the data shown in Figure 3.7, the choice of the minimum energy used in the FAST E_{ave} computation was not found to have a significant impact on the agreement between the FAST and UVI E_{ave} values for E_{min} between 100-500 eV. Moreover, if there was a substantial flux of electrons with energies greater than 30 keV during the period when we are comparing the FAST and UVI mean energy values, the FAST data would give no indication, since these are outside the electron energy range covered by FAST. The precipitation of these greater than 30 keV electrons would, however, contribute to the luminosity measured by UVI and result in an increased estimate for the average energy relative to FAST.

3.3 Summary

Auroral substorms represent the injection of magnetotail particles into the near-Earth environment and their subsequent precipitation. The location of an isolated substorm breakup is identified within a narrow region in local time, usually near the pre-midnight or midnight auroral zones (2100-0000 MLT). Auroral intensifications resulting from the compression of the magnetosphere by a strong solar wind pressure pulse behave differently from the usual auroral substorms. Pressure pulse driven auroral enhancements are much more global phenomena than isolated substorms, involving the precipitation of electrons from a larger portion of the magnetosphere with enhancements of precipitating electron energy flux and latitudinal expansion of both the dayside and nightside aurora.

The regions of the auroral oval with the highest energy flux during the December 18, 1996 isolated substorm are coincident with where the electron precipitation has the highest mean energy ($E_{\text{ave}} \geq 10$ keV). In comparison to the isolated substorm, the electron precipitation during the pressure pulse related intensification has lower average energies, less than 7.0 keV, in the regions where we observe the highest energy

flux. The spatial distribution of precipitation electron average energies is ordered in local time during the isolated substorm while less structure is seen in the E_{ave} maps for the pressure pulse related event for which the mean energy only varied in latitude. A westward surge and the hard electron precipitation associated with this substorm feature does not appear in the pressure pulse related auroral intensification.

The auroral brightening associated with the arrival of an interplanetary pressure pulse has superficial similarities to that observed during substorms, including the poleward excursion of the auroral oval and an increase in the energy flux of electron precipitation. However, we have presented new observations that point out key differences in the physical processes during these phenomena. The lower average energy of the electron precipitation observed following an interplanetary pressure pulse arrival and the lack of discrete structure in the E_{ave} images imply that the auroral acceleration region is not as important in governing the properties of electron precipitation during these pressure pulse related intensifications. There is no indication of electron injection and subsequent hard morningside precipitation for pressure pulse related auroral activity as there is during substorms. Furthermore, we do not find evidence for the closure of field-aligned currents in the ionosphere via the substorm current wedge (SCW) based on the lack of a westward surge-like feature during the pressure pulse related intensification. This also implies that the processes which may reconfigure the magnetotail are different for isolated substorms and pressure pulse associated intensifications. The differences in the characteristics of auroral intensifications in response to the arrival of an interplanetary pressure pulse from those of isolated substorms suggest that these solar wind structures do not trigger auroral substorms.

The essential distinction between the isolated substorm cases and the pressure pulse related aurora described here is the presence or absence of auroral acceleration between the magnetosphere and ionosphere. In the next chapter we will investigate in further detail the isolated substorm cases and the properties of auroral acceleration during these events.

Chapter 4

SEASONAL VARIATIONS IN AURORAL STRUCTURE AND TIME SCALES DURING SUBSTORMS

This chapter will investigate how the temporal and spatial characteristics of auroral substorms vary as a function of season. Seasonal differences in auroral precipitation have been demonstrated on long time scales, averaging quantities such as the precipitating electron energy flux [Newell *et al.*, 1996; Liou *et al.*, 2001] or auroral brightness [Shue *et al.*, 2001; Petrinec *et al.*, 2000] over many months or years. More intense energy flux values (or auroral brightness) and higher average energies observed during the winter (when the auroral zone is in darkness) than in summer is cited as evidence that auroral acceleration is less effective under conditions of enhanced ionospheric densities (conductivity). We showed in the previous chapter that auroral acceleration is an essential aspect of substorm precipitation. The study presented here extends previous work by examining if substorm dynamics are affected by this same mechanism.

To quantify auroral substorm time scales, the phases of a substorm will be defined using the UVI derived hemispheric power. This approach does not rely on ancillary measurements but will allow us to relate the time scales of observed substorm activity with those associated with magnetospheric processes such as bulk plasma motions and Alfvén wave propagation.

A superposed epoch analysis of precipitating electron energy flux and average energy inferred from UVI observations is performed using the temporal framework described below for substorms that occur in each season. The state of the ionosphere during each season is quantified by the level of background Pedersen conductivity in the auroral zone for conditions spanning winter solstice, equinox, and summer solstice.

4.1 Substorm phases defined by hemispheric power

We discuss the hemispheric power computed from the UVI auroral images to quantify the phases of a magnetospheric substorm. We will demonstrate that the exponential decay of the hemispheric power following an auroral breakup provides a characteristic time scale, τ , which defines epochs for different substorm phases. For completeness, the UVI derived hemispheric power is related to a more familiar substorm activity index, AE, in Appendix B.

For each pixel (or spatial bin) in the LBHI images, the energy flux (in units of $\text{ergs cm}^{-2} \text{s}^{-1}$) is inferred and the geometric area is known (assuming some emission altitude for the aurora). Multiplying the energy flux by the area in each pixel yields a measure of power. When integrated over the area of the auroral oval we obtain the hemispheric power (HP). The hemispheric power measures the rate at which energy is being deposited into the ionosphere by auroral particle precipitation. This is shown in Equation 4.1 where $Q_{i,j}$ is the energy flux and $A_{i,j}$ is the area for each pixel(i,j). Pixels in which the energy flux, $Q_{i,j}$, is below $1 \text{ erg cm}^{-2} \text{ s}^{-1}$ are thrown out of the summation so that any residual noise in the images do not contribute to the hemispheric power calculation. The computation of the hemispheric power from UVI images has also been previously described by *Lummerzheim et al.* [1997].

$$HP = \sum_{i=1}^{200} \sum_{j=1}^{228} Q_{i,j} A_{i,j} \quad (4.1)$$

The hemispheric power derived from the UVI images has a time resolution between 36.8 seconds and approximately six minutes depending on the mode in which UVI is operating. Since the hemispheric power is an integrated quantity, the spacecraft wobble has a negligible effect on this measurement under the assumptions that flux is conserved regardless of how the measured photons are spatially distributed in an image. We limit our use of the hemispheric power for the analysis of substorms to events for which the entire area of auroral oval is included in the field of view. This mitigates the need to normalize the hemispheric power for varying fields of view in the UVI observations.

An example of how the hemispheric power varies over an auroral substorm is given in Figure 4.1 for an event that occurred on January 25, 1998 (980125). The vertical axis denotes the hemispheric power in units of gigawatts (GW) and the horizontal axis is universal time. The dashed, vertical lines demarcate the substorm epochs as defined by the UVI derived hemispheric power. Selected UVI images are shown in Figure 4.1 to illustrate the global auroral morphology during each substorm epoch (phase). The B_z (GSM) component of the interplanetary magnetic field (IMF) measured by the Magnetic Field Instrument [Lepping *et al.*, 1995] aboard the Wind spacecraft is shown on the bottom panel of Figure 4.1. A propagation correction of 55 minutes has been applied to the IMF data since the Wind spacecraft was at a radial distance of 236 R_E during the onset of this substorm. Although the B_z component is southward during the onset of this substorm, it turns and remains northward for most of the event.

Using the hemispheric power as a metric, the onset (T_{onset}) of the auroral substorm is defined as the time when this parameter increases above one standard deviation of the values in the preceding 30 minutes. In Figure 4.1 the onset of the substorm occurs at 03:55:04 UT. In the corresponding image, the substorm breakup is observed as a localized enhancement of the precipitating energy flux near 2300 MLT (Figure 4.1, Image B).

The period of time between T_{onset} and the peak in the hemispheric power is defined as the next substorm epoch following onset ($T_{\text{onset}} - T_{\text{HP}_{\text{max}}}$). This epoch is equivalent to the canonical expansion phase of a substorm. In Figure 4.1 this is shown between 03:55:03-04:33:06 UT when the hemispheric power increases from about 40 GW to 115 GW. Both the precipitating electron energy flux and the observed surface area of the auroral oval increase during this interval (Figure 4.1, Images C-D) and the slope of HP curve is generally positive during this interval. The region of intense precipitating electron energy flux near the westernmost extent of the substorm expansion near 18 MLT is identified as the westward surge (Figure 4.1, Image D). The substorm epoch $T_{\text{onset}} - T_{\text{HP}_{\text{max}}}$ ends when the auroral oval has expanded to its greatest poleward and westward extent. This corresponds to the time when the precipitating electron energy flux is most intense (Figure 4.1, Image D) and the hemispheric power has risen to its

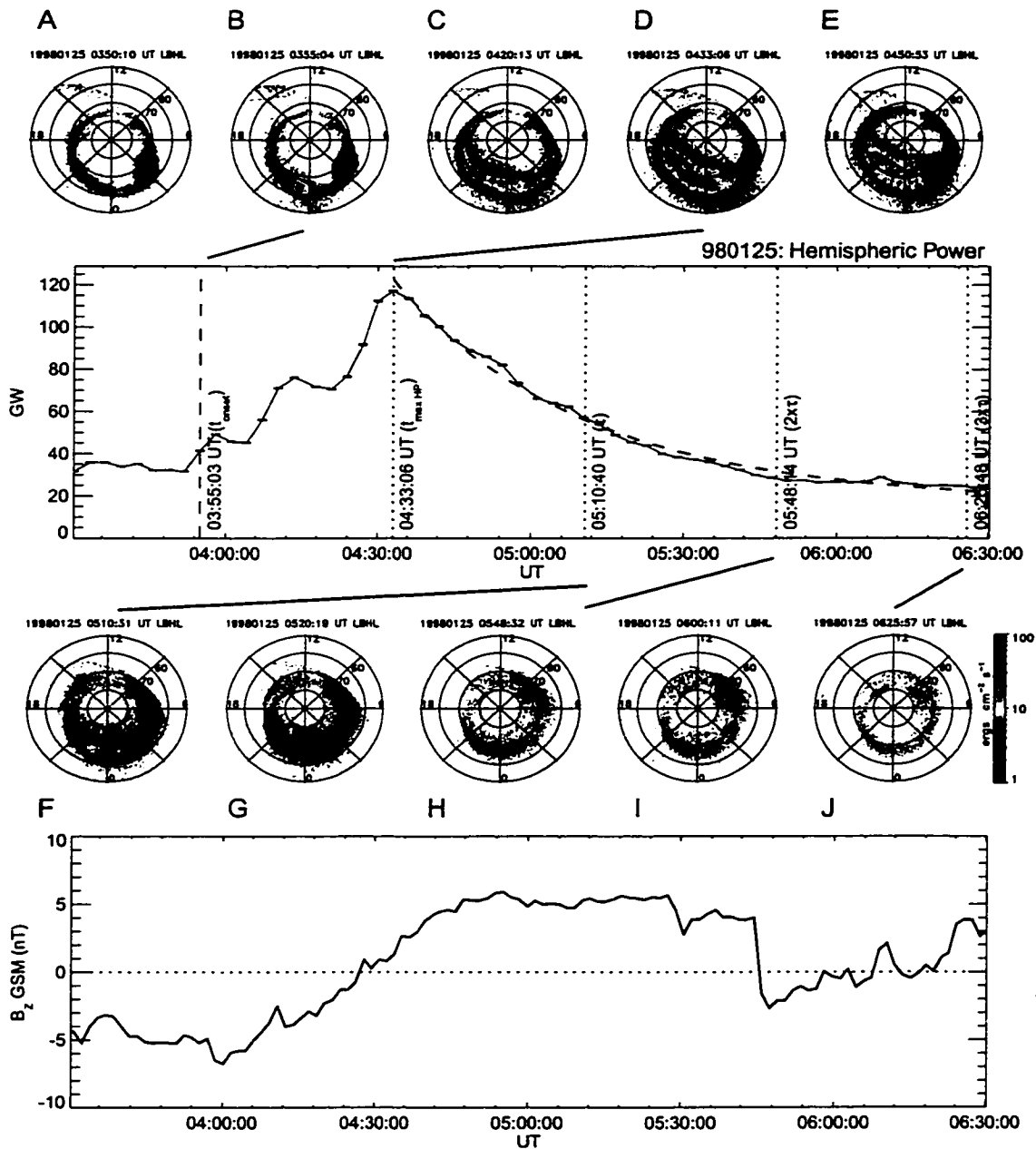


Figure 4.1: Hemispheric power for an isolated substorm on January 25, 1998 during a geomagnetically quiet period (D_{st} near -5 nT). This substorm event occurred during northward IMF conditions. The dashed line beginning at 04:33:06 UT ($T_{HP_{max}}$) shows the least-squares fit of the HP to an exponential function given by Equation 4.2. The vertical dotted lines denote the substorm epochs as described in the text. UVI images are shown at key times during the evolution of the substorm.

maximum value following the onset of the substorm.

Figure 4.1 shows that the rate at which energy is deposited in the upper atmosphere by auroral electrons slows exponentially after reaching its peak value. In some cases the hemispheric power exhibits aperiodic enhancements superposed upon the exponential decay. This decay of the hemispheric power is described by Equation 4.2.

$$HP(t) = HP_{max}e^{\frac{-t}{\tau}} + HP_o \quad (4.2)$$

Here HP_{max} is the maximum enhancement of the hemispheric power above its pre-onset value during a substorm, represented by HP_o . The e -folding time, τ , provides a convenient and natural fiducial time with which to define the next epoch of a substorm. This is the interval between the time of the maximum increase of the hemispheric power and the e -folding time ($T_{HP_{max}} - \tau$). In the example shown in Figure 4.1, the hemispheric power peaks at 04:33:06 UT. The e -folding time given by fitting the hemispheric power after $T_{HP_{max}}$ to Equation 4.2 is 37.6 minutes, shown at 05:10:40 UT. The epoch between $T_{HP_{max}}$ and τ is the beginning of substorm recovery. During this period, the hemispheric power decreases through the reduction of the precipitating electron energy flux since the area of the auroral oval does not change significantly between 04:50 UT and 05:10 UT (Figure 4.1, Images E-F).

Subsequent substorm epochs are defined as multiples of the hemispheric power e -folding time, τ : $\tau - 2\tau$ and $2\tau - 3\tau$. These are marked at 05:48:14 UT and 06:25:48 UT respectively in Figure 4.1. By 2τ the hemispheric power has recovered to its pre-onset value near 30 GW. This is typical of substorms that occur when the B_z component of the IMF is predominantly northward.

4.1.1 IMF influence on substorm hemispheric power

In contrast to the example shown in Figure 4.1, the hemispheric power behaves in a slightly different manner during substorms for which the IMF B_z is southward. An example of this is shown in Figure 4.2 which is in the same format as Figure 4.1. The IMF B_z component remains at a steady southward value near -6.5 nT throughout the duration of this substorm (Figure 4.2, bottom panel). Following the onset and

expansion of the auroral oval (Figure 4.2, Images B-E), the hemispheric power does not decay back to its pre-onset level as in the northward IMF case. By three e -folding times (3τ) the hemispheric power is still a factor of two higher than it was before substorm onset and is sustained primarily by aurora along the dawn and dusk flanks of the auroral oval with precipitating energy fluxes above $10.0 \text{ ergs cm}^{-2} \text{ s}^{-1}$.

Figures 4.1 and 4.2 illustrate that the hemispheric power is sustained above its pre-onset levels for longer time scales for substorms occurring during southward IMF than those where the IMF B_z is northward. To examine this behavior in a more general sense, we perform a superposed epoch analysis of the hemispheric power values for substorms occurring during northward IMF versus those that occur when the IMF is southward (Figure 4.3). The determination of the IMF orientation is made from Wind MFI measurements in GSM coordinates which are propagated in time from the spacecraft location to a nominal magnetopause location set at $10 R_E$. A substorm is determined to occur during northward (southward) IMF if the average value of B_z is positive (negative) during a 30-minute time window around the onset of a substorm and for a period of two hours following the onset time. Universal time during each event is normalized to the substorm epoch fiducial times described above (T_{onset} , T_{HPmax} , τ , 2τ , and 3τ). The hemispheric power data are normalized to the maximum values for each event and set to one. The hemispheric power values are averaged within each substorm epoch and at each fiducial time for 124 events with northward IMF and 227 substorms with southward IMF. Figure 4.3 shows that the hemispheric power is maintained at a level 10% above pre-onset values beyond three e -folding times of the HP parameter for substorms during southward IMF. Northward IMF events, on the other hand, see the hemispheric power fall near their pre-onset values by two e -folding times as the event in Figure 4.1 demonstrates.

The distributions of peak hemispheric power values sorted by IMF orientation are shown in Figure 4.4. The peak hemispheric power can be viewed as a measure of the "size" or intensity of substorm activity. The mean value of the hemispheric power distributions for northward IMF substorms is 61.5 GW with a standard deviation of 44.9 GW. The distribution of peak HP values for southward IMF substorms has a mean

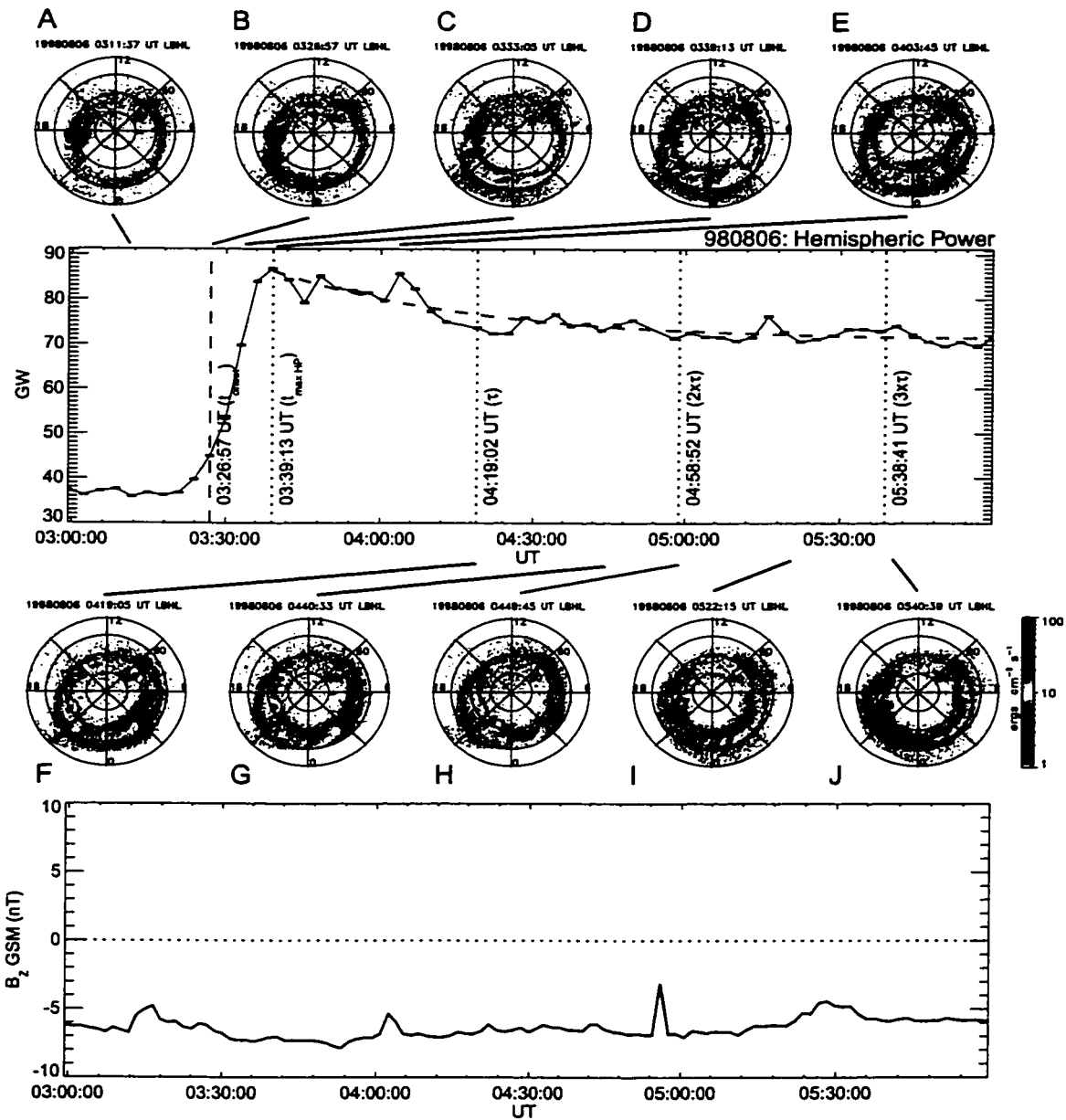


Figure 4.2: Same format as Figure 4.1 but for a substorm occurring during southward IMF. A propagation correction of 24 minutes is made to the IMF data since the Wind spacecraft was upstream in the solar wind at a radial distance of $92.8 R_E$. Note that the hemispheric power is sustained above its pre-onset level past three HP e -folding times.

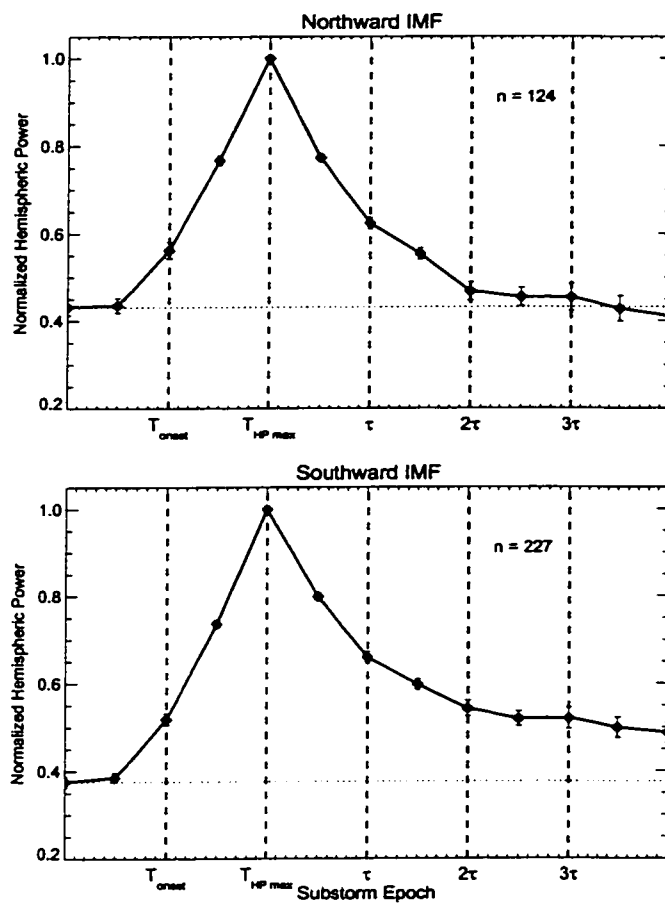


Figure 4.3: A superposed epoch analysis is performed on the hemispheric power for substorms that occur when the IMF is northward (**top panel**) versus southward (**bottom panel**). The hemispheric power values are normalized to the peak value for each event. Universal time is normalized to the substorm epochs defined in Section 4.1. The error bars are the standard deviation of mean hemispheric power value for each epoch.

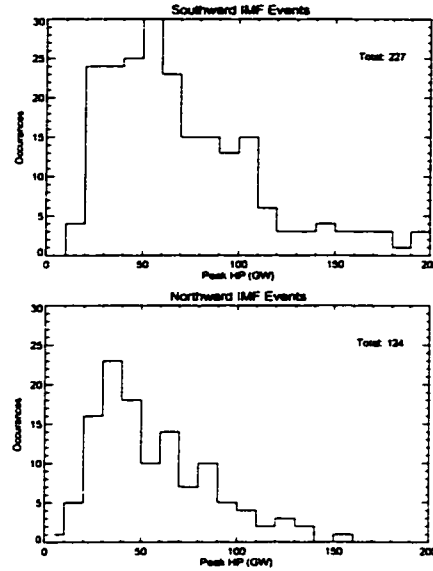


Figure 4.4: Histograms of the peak hemispheric power values for substorms sorted by IMF B_z orientation.

value and standard deviation of 78.2 GW and 54.9 GW respectively. The median values of the peak hemispheric power distributions are 49.5 GW and 63.3 GW for the northward and southward IMF cases, respectively. To determine whether or not the distributions of peak hemispheric power sorted by IMF B_z orientation are similar, we compute a reduced chi-squared parameter given by Equation 4.3.

$$\tilde{\chi}^2 = \frac{1}{d} \sum_{k=1}^n \frac{(D1_k - D2_k)^2}{D2_k} \quad (4.3)$$

Here d is the number of degrees of freedom, taken as the number of bins, n , used to compute each distribution minus one. $D1$ specifies some distribution of a quantity and $D2$ is another distribution against which $D1$ is to be tested. $\tilde{\chi}^2$ values on the order of one or less ($\tilde{\chi}^2 \leq 1$) indicate that the two distributions, $D1$ and $D2$, are similar. If $\tilde{\chi}^2$ is much larger than one ($\tilde{\chi}^2 \gg 1$) then we expect $D1$ and $D2$ to be different. The degree of similarity between $D1$ and $D2$ is quantified by computing $P(\tilde{\chi}^2 \geq \tilde{\chi}_0^2)$, the probability of obtaining a $\tilde{\chi}^2$ as large as that computed from the observed distributions, $\tilde{\chi}^2$, given

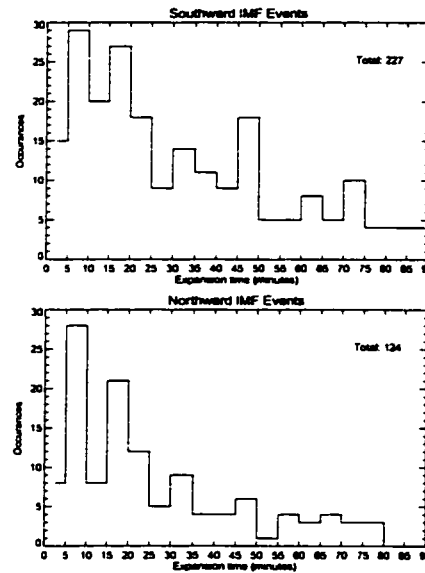


Figure 4.5: Histograms of substorm expansion times sorted by IMF B_z orientation.

the number of degrees of freedom. We use a standard criterion of specifying that two distributions disagree if $P(\chi^2 \geq \bar{\chi}_0^2)$ is less than 5% [Taylor, 1982, for example].

The reduced chi-squared value when comparing the peak hemispheric power distributions shown in Figure 4.4 is 2.75. This corresponds to $P(\chi^2 \geq \bar{\chi}_0^2)$ of less than 0.05%, indicating that the two distributions are different. We find that the peak hemispheric power is about 27% on average greater for substorms that occur under southward IMF conditions versus those for which the IMF B_z component is northward. It should be noted however that our sampling is largely biased toward substorms for which the IMF B_z is southward.

We now examine the the influence of IMF orientation on the times associated with substorm expansion ($T_{onset} - T_{HP_{max}}$) and recovery (τ). Figure 4.5 shows histograms of the substorm expansion times for substorms where the IMF B_z is southward (top panel) or northward (bottom panel). The substorm expansion times in the northward IMF case have an average value of 26.7 minutes with a standard deviation of 22.4 minutes. Similarly, in the distribution of substorms for which the IMF is southward,

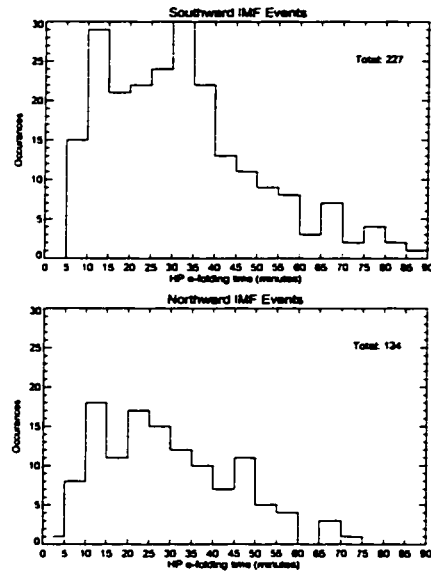
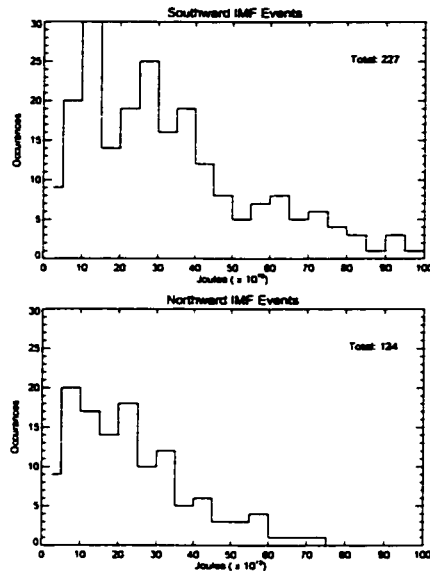


Figure 4.6: Histograms of the hemispheric power e -folding times sorted by IMF B_z orientation.

the mean expansion time is 36.6 minutes with a standard deviation of 34.9 minutes. In comparing the distributions of substorm expansion times for northward and southward IMF, we calculate a reduced chi-squared value of 2.17. This corresponds to a $P(\chi^2 \geq \bar{\chi}_0^2)$ of 0.1%, indicating that the two distributions of substorm expansion times sorted by IMF B_z orientation are not consistent. The mean substorm expansion time is roughly 37% longer for substorms during southward IMF.

Figure 4.6 shows histograms of the hemispheric power e -folding times for substorms where the IMF B_z is southward (top panel) or northward (bottom panel). The hemispheric power e -folding times for the northward and southward IMF cases have mean values and standard deviations of 30.32 ± 16.7 minutes and 33.4 ± 20.7 minutes respectively. Median values for τ for northward IMF events and τ for southward IMF events are 27.9 minutes and 30.7 minutes respectively. The reduced chi-squared value when comparing the northward and southward IMF cases for the τ distributions is 2.72, giving $P(\chi^2 \geq \bar{\chi}_0^2)$ less than 0.05%. The variation of the hemispheric power e -folding time



| Total Energy Deposited ($\times 10^{13}$ Joules) | Mean | Median | Standard Deviation |
|---|------|--------|--------------------|
| Northward IMF B_z | 23.3 | 21.2 | 15.7 |
| Southward IMF B_z | 37.4 | 29.1 | 33.7 |

Figure 4.7: Distributions of total energy dissipated during substorm events sorted by IMF B_z orientation

for different IMF B_z orientations is small with the mean value of τ being only about 10% longer during southward IMF conditions.

Knowing the hemispheric power during a substorm and having quantitative measures of the times scales over which that power is supplied, we can readily compute the total energy input into the ionosphere (in one hemisphere) by auroral electron precipitation for each event. We compute the hemispheric energy deposition in Joules by integrating the hemispheric power from the substorm onset time to three HP e -folding times (3τ):

$$J_{HP} = \int_{t_{onset}}^{3\tau} HP dt \quad (4.4)$$

We sort the total energy deposition by IMF B_z orientation and find that the energy input through auroral electron precipitation is greater for substorms in which the IMF

B_z is southward (Figure 4.7). The mean, median, and standard deviation values for the total substorm hemispheric energy deposition are given in Figure 4.7. A comparison of the total energy deposition distributions for northward versus southward IMF gives a χ^2 value of 2.95 and $P(\chi^2 \geq \chi_0^2)$ less than 0.05%. We find that the average energy deposition in auroral substorms is about 60% larger for those that occur under southward IMF than for those where the IMF is northward. This result follows from the tendency for substorms during which the IMF B_z is southward to sustain a higher level of hemispheric power during substorm recovery as demonstrated in Figures 4.2 and 4.3.

4.2 Seasonal variations of auroral substorm characteristics

Building on previous statistical studies of seasonal variability (as described in Section 1.2.2), we investigate how substorm time scales and auroral precipitation characteristics vary with season. The objective here is to evaluate the hypothesis that ionospheric conductivity plays a major role in determining large-scale auroral structure and how this varies in time during substorm activity.

The seasonal periods used in this study are centered on each solstice and equinox and are defined conveniently by day of year (DOY), similar to those used by *Petrinec et al.* [2000]. *Winter* is defined as DOY 309-34 (November 5 - February 3), spring is then DOY 35-125 (February 4 - May 5), summer follows as DOY 126-217 (May 6 - August 5), and autumn is DOY 218-308 (August 6 - November 4)¹. The seasonal variations in the height-integrated ionospheric Hall and Pedersen conductivities (conductance) due to incident solar UV photoionization are shown in Figure 4.8. These conductances are computed using the empirical model of *Rasmussen et al.* [1988] which is parameterized by solar zenith angle (Φ_{sza}), solar F10.7 cm flux ($f_{10.7}$), and the magnetic field magnitude (B) at the altitude where the conductances are evaluated. The solar F10.7 cm flux is a proxy for the level of solar EUV flux.

$$\Sigma_H = \frac{5.6}{B} (1 - 0.000111\Phi_{sza}^2) (1 - 0.15f_{10.7} + 0.05f_{10.7}^2) \quad (4.5)$$

¹Calendar dates are valid for non-leap years

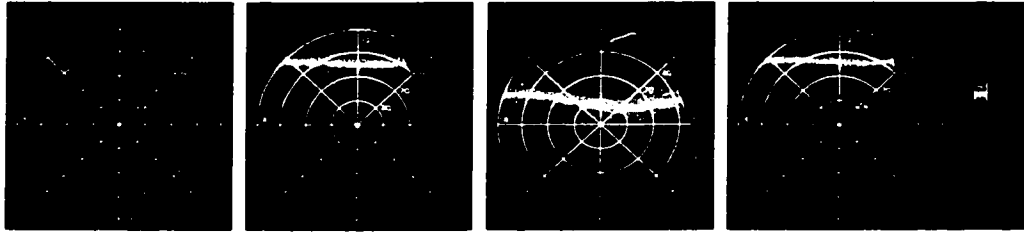


Figure 4.8: Seasonal variations in ionospheric Pedersen conductance computed from the model of *Rasmussen et al.* [1988]. From left to right, the Pedersen conductances are shown for winter, spring, summer, and autumn.

$$\Sigma_P = \frac{4.5}{B} (1 - 0.000105 \Phi_{sza}^2) (1 - 0.15 f_{10.7} + 0.05 f_{10.7}^2) \quad (4.6)$$

B is evaluated with the International Geomagnetic Reference Field (IGRF) model at an altitude of 120 km, the assumed auroral emission height. The units of the Hall and Pedersen conductances in Equations 4.5 and 4.6 are mhos. From the conductance point of view, the conditions in the ionosphere are similar during each equinox period. For this reason, we combine the events for the spring and autumnal equinoxes into one seasonal category. Using the seasonal criteria above, we have a distribution of 105 events in the winter, 107 during the summer, and 120 substorms for the equinoctial periods. These are all isolated substorm cases, meaning they are not associated with magnetic storm periods.

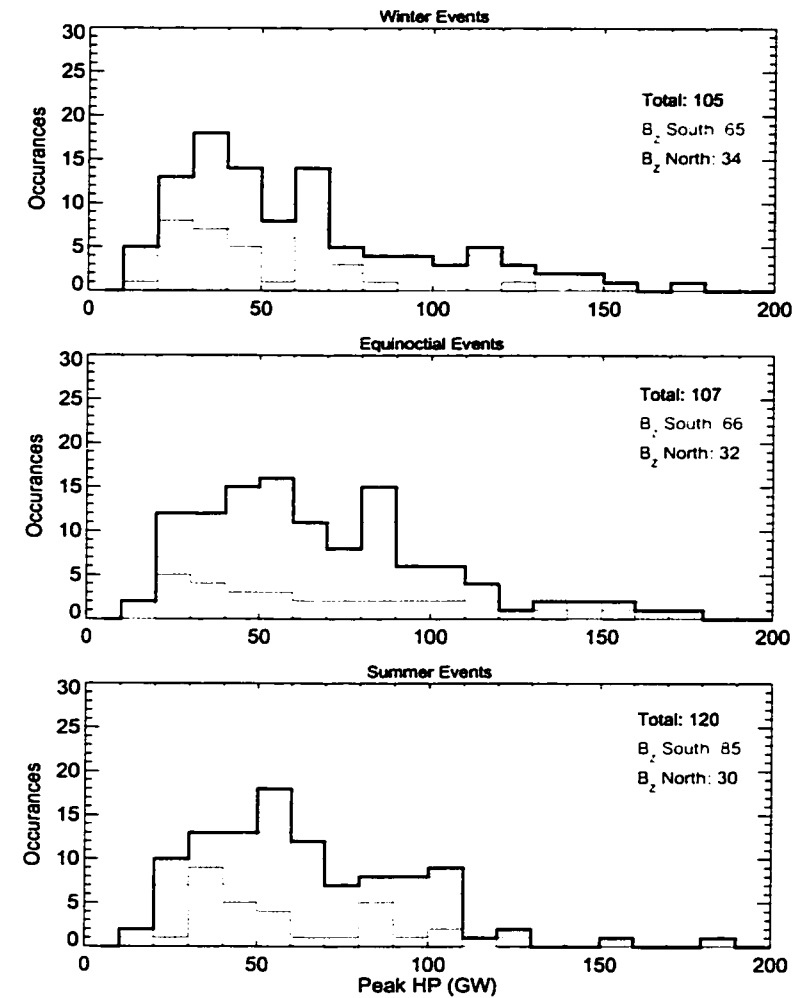
To examine how the magnitudes of the substorms vary with season, we plot histograms of the peak hemispheric power for the events in each seasonal category (Figure 4.9). The peak power histograms are further subdivided by orientation within each seasonal category with the red (blue) histograms denoting events for which the IMF B_z was southward (northward). The mean, median, and standard deviation values are given for each seasonal category in Figure 4.9. On average, the peak hemispheric power values are shown to be slightly higher during equinox and summer than during winter. The winter and equinoctial peak hemispheric power distributions both have tails that extend to large values greater than 150 GW which is lacking in the

summer distribution. Testing the similarity between the winter and equinox distributions of peak hemispheric power gives a reduced chi-squared value of 1.30. This gives $P(\tilde{\chi}^2 \geq \tilde{\chi}_0^2) = 17.5\%$, indicating that these distributions are consistent under the 5% criterion. Similarly, $\tilde{\chi}^2 = 0.70$ and $P(\tilde{\chi}^2 \geq \tilde{\chi}_0^2) = 82\%$ in the comparison of the equinox to summer peak hemispheric power distributions. The summer-time and winter distributions of peak hemispheric power are not consistent with $\tilde{\chi}^2 = 2.15$ and $P(\tilde{\chi}^2 \geq \tilde{\chi}_0^2) = 0.3\%$. However, the mean values of the peak hemispheric power during summer and winter differ by less than 3% with comparable standard deviations.

We do not find large differences in the seasonal distributions of peak hemispheric power. Further sorting by IMF B_z orientation does not reveal any additional relationships between season and peak hemispheric power. Moreover, Figure 4.9 suggests that our comparisons of seasonal substorm characteristics are not biased by substorms being more intense one season versus another based on the peak rate of auroral energy deposition during each event.

Next we examine variations of substorm expansion times sorted by season. Figure 4.10 shows that the distributions of this parameter sorted by season are broad with large standard deviation for all three seasonal categories. The mean, median, and standard deviation values of these substorm expansion time distributions are given in Figure 4.10. The mean and median expansion times for substorms occurring during summer periods is almost a factor of two shorter than those occurring during equinox and 30% shorter than those during winter. The reduced chi-squared statistic shows that the winter and equinox expansion time distributions are similar with $\tilde{\chi}^2 = 0.67$ and $P(\tilde{\chi}^2 \geq \tilde{\chi}_0^2) = 84\%$. The reduced chi-squared values when comparing winter-time expansion times to summer and equinox expansion times to summer are 1.71 and 1.96, respectively. These $\tilde{\chi}^2$ values each give $P(\tilde{\chi}^2 \geq \tilde{\chi}_0^2)$ less than 2%, indicating a dissimilarity between the summer distribution of expansion times to those during the winter and equinox. In further subdividing the events in each seasonal category by IMF B_z orientation, we find that in all cases, the substorms with the longest expansion times are those where the IMF B_z was southward.

The largest difference in the seasonal characteristics of substorms comes when we



| Peak Hemispheric Power (GW) | Mean | Median | Standard Deviation |
|-----------------------------|------|--------|--------------------|
| Winter | 66.2 | 56.1 | 46.5 |
| Summer | 68.2 | 59.4 | 43.7 |
| Equinox | 75.1 | 64.0 | 51.6 |

Figure 4.9: The peak enhancement of the hemispheric power above its pre-onset values for substorms occurring in winter (**top panel**), equinox (**middle panel**), and summer (**bottom panel**) conditions are shown in these histograms. One sees that the distributions of peak HP enhancement are not significantly different for events occurring in different seasons.

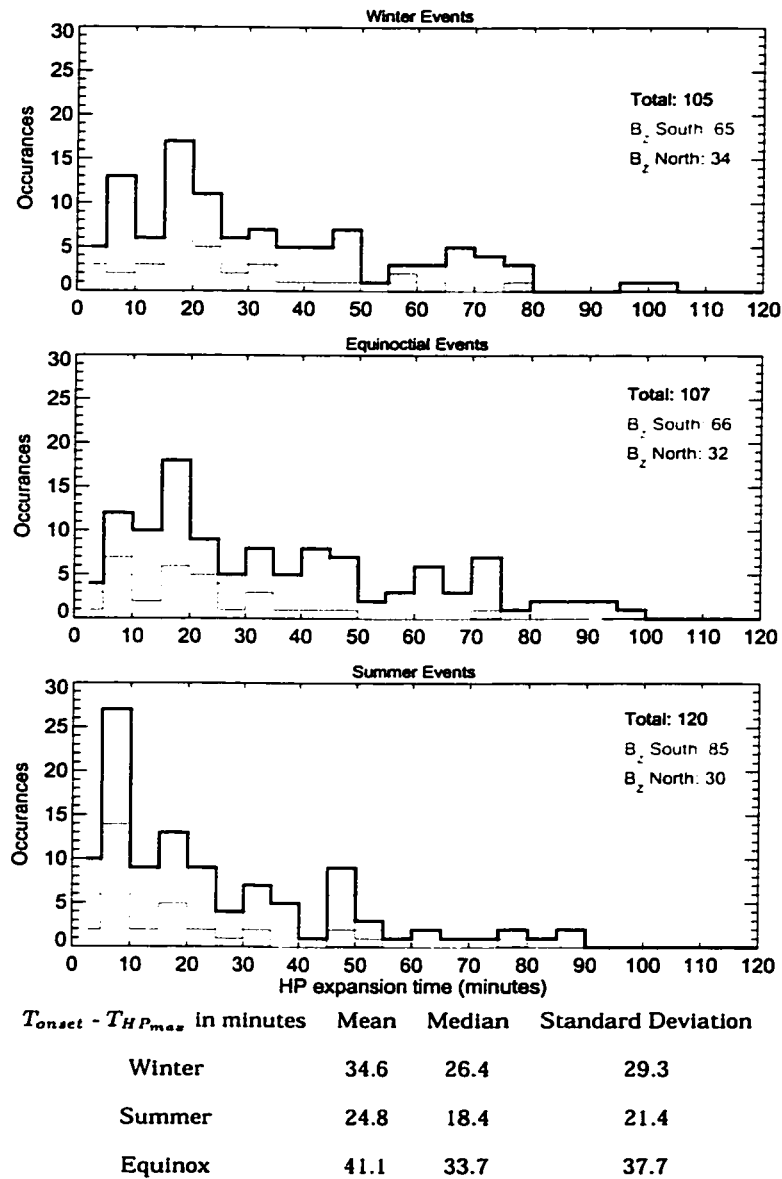


Figure 4.10: Seasonal distributions of substorm expansion times. The histogram in the **top** panel shows the distribution of substorm expansion times for events occurring in a dark (winter) ionosphere. The **middle** and **bottom** panel shows the expansion times for events occurring in equinox and summer (sunlit) conditions, respectively.

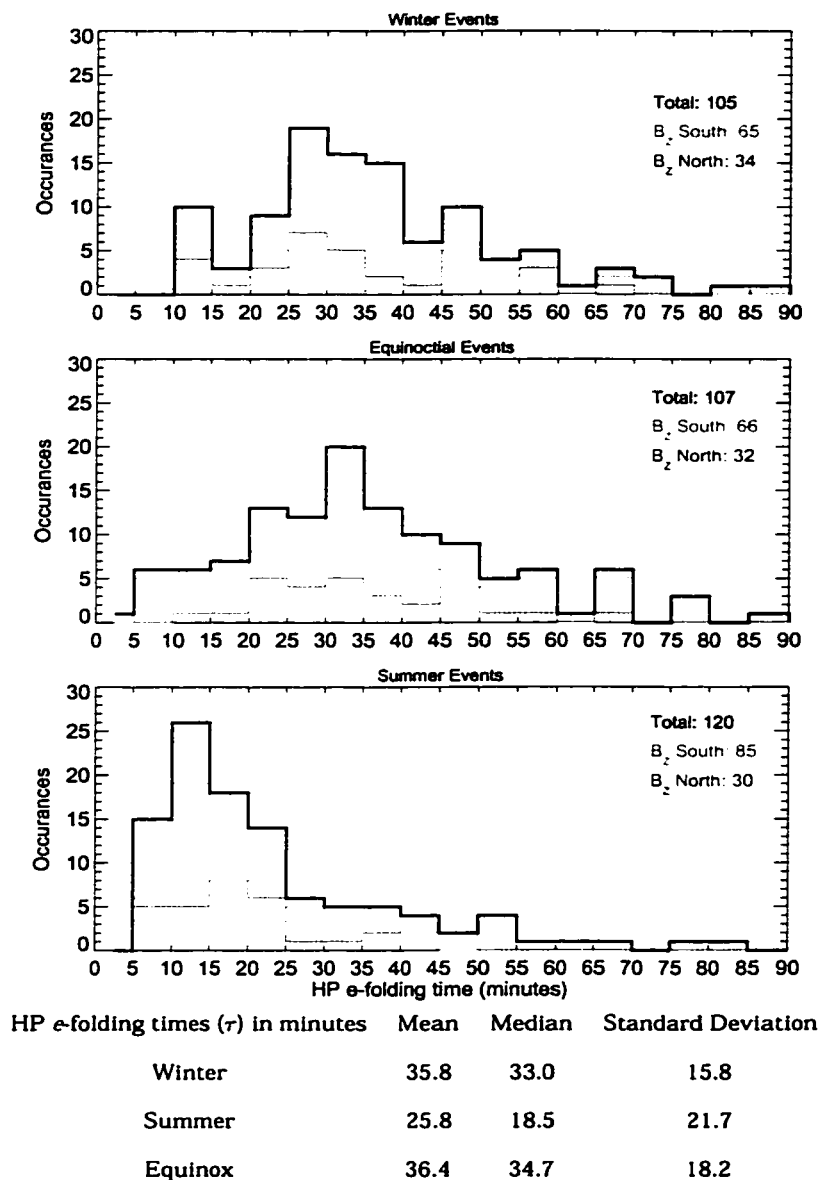
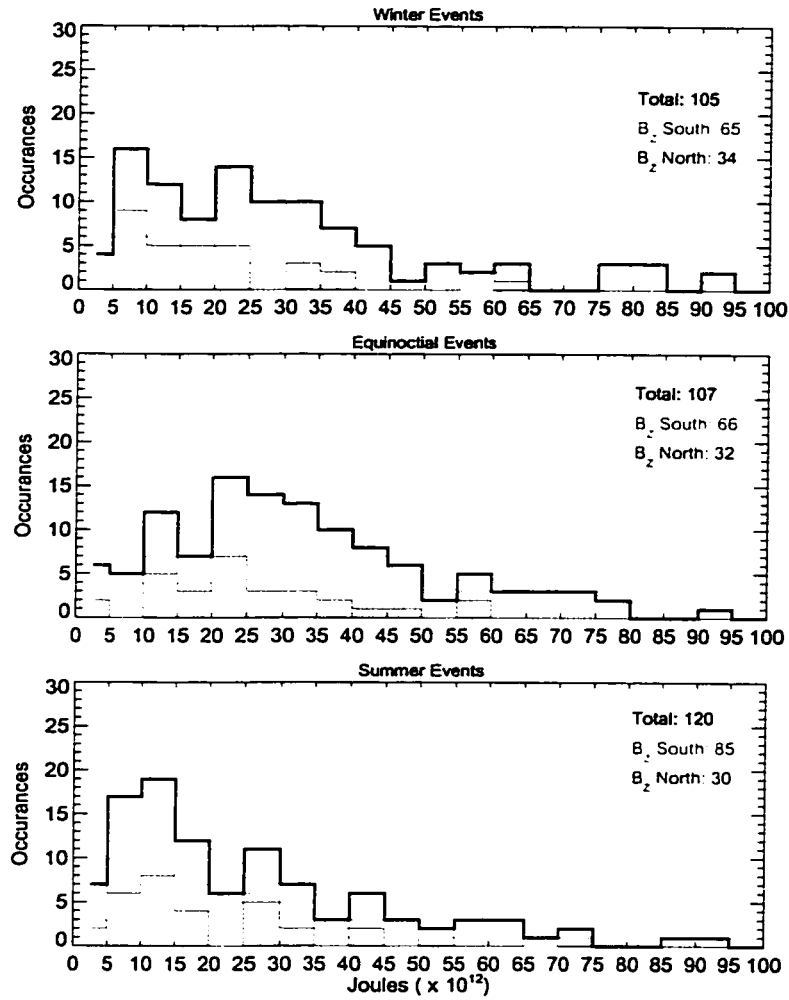


Figure 4.11: Seasonal distributions of substorm recovery τ -folding times. The histogram in the **top** and **middle** panels show the distributions of τ -folding times for events occurring in a dark (winter) and equinoctial ionosphere, respectively. The **bottom** panel shows a histogram of τ values for events occurring during summer. Within the seasonal categories, substorms are further subdivided according to the IMF B_z orientation during each event. Events that occur when B_z is southward (northward) are shown in red (blue).



| Total Energy Deposited ($\times 10^{13}$ Joules) | Mean | Median | Standard Deviation |
|---|------|--------|--------------------|
| Winter | 31.1 | 23.8 | 24.9 |
| Summer | 27.4 | 18.8 | 23.1 |
| Equinox | 37.8 | 30.1 | 36.6 |

Figure 4.12: Histograms of total energy deposited by auroral electron precipitation, sorted by season.

examine the hemispheric power e -folding times Figure 4.11. We find that the decay time for the hemispheric power is about a factor of two longer for substorms that occur during the winter and equinox periods than during summer. The distribution of substorm decay times for substorms in sunlit conditions is peaked between 10-15 minutes, with a median value of 18.5 minutes. The mean and median values of τ are similar for the winter and equinoctial substorms, about 35 minutes. The reduced chi-squared value when comparing the winter-time τ values to those during summer is 9.33. Likewise, $\bar{\chi}^2 = 7.44$ when comparing the hemispheric power e -folding times during equinox and summer. These reduced chi-squared values correspond to $P(\bar{\chi}^2 \geq \bar{\chi}_0^2)$ values less than 0.05%. We find that the winter-time and equinox distributions of τ are similar with $\bar{\chi}^2 = 1.44$ and $P(\bar{\chi}^2 \geq \bar{\chi}_0^2) = 12\%$.

The time scale for the persistence of substorm activity is a factor of two longer when the nightside auroral zone is in darkness (winter and equinox) than when it is sunlit. The hemispheric power decay times show a much larger variation when sorted by season than when separated by IMF B_z orientation. There is some indication in Figure 4.11 that a southward IMF extends the decay times to longer values in each seasonal category, particularly in the summer period where all events with τ greater than 50 minutes are during southward IMF.

The total energy deposited by auroral electrons during substorms is found to be greatest for equinoctial substorms, lower for winter substorms, and lowest for substorms occurring in sunlit conditions (Figure 4.12). This is consistent with the observation that substorms during all seasonal conditions have similar energy deposition rates (Figure 4.9) but different decay times (Figure ref-efold-dist): the total energy deposited during a substorm in the equinoctial and winter periods is higher than during the summer because the enhanced hemispheric power associated with auroral electron precipitation is sustained for longer periods of time. The winter-time and summer total energy deposition distributions are comparable with a $\bar{\chi}^2$ value of 1.5 and $P(\bar{\chi}^2 \geq \bar{\chi}_0^2) = 7.7\%$. The equinoctial distribution of total energy deposition differ from both the winter-time and summer distributions. The mean total energy deposition during the equinox periods is 38% greater than that in summer and 22% larger than that during

winter. When testing the equinox distribution of total energy deposition with each of the winter-time and summer ones, the reduced chi-squared values are greater than 2.35, giving $P(\tilde{\chi}^2 \geq \tilde{\chi}_0^2)$ less than 0.05%.

4.3 Superposed epoch analysis of auroral electron energy flux and average energy

Having now established a quantitative means to define substorm phases (epochs) directly from our imaging data and to measure the time scales associated with each phase, we perform a superposed epoch analysis of the UVI derived auroral electron energy flux and average energy during substorms for each seasonal category. The electron energy flux and average energy measurements used in this superposed epoch analysis are binned in 0.5° MLAT \times 0.5 MLT hour segments as described in Section 2.1.3. After determining the fiducial times to demarcate the substorm epochs for each event, a weighted average of the energy flux and average energy is performed using the known uncertainties in each parameter as the weights (Equation 4.7).

$$w_{(Eflux;Eave)} = \frac{1}{\sigma_{(Eflux;Eave)}^2} \quad (4.7)$$

Representative FAST electron measurements are shown to illustrate the main features in the precipitation during each substorm epoch and seasonal category. Since we observe the most auroral variation during substorms in the pre-midnight to midnight sector (2200-2400 MLT), the FAST observations shown below are all taken in this local time sector. The UVI images corresponding to each set of FAST data shown below can be found in Appendix C.

4.3.1 Pre-onset ($t < T_{onset}$)

Figure 4.13 represents the characteristics of the auroral precipitation observed in the 30 minutes prior to the onset of each substorm. On average, we observe little significant seasonal variation in the auroral electron energy flux prior to the onset of substorms. This epoch implicitly includes quiet auroral periods. However, we do find

that the boundaries of the summer-time auroral oval are contracted poleward relative to where we observe the average oval location during the winter and equinoctial periods. This difference is most pronounced in the evening sector (2100 MLT) where the statistical, pre-onset auroral oval is shifted poleward by as much as 5° MLAT.

The average energy of the pre-onset electron precipitation shows a higher degree of variability with season, especially in the poleward region of the pre-midnight sector between 2100-2400 MLT. The average energies of the incident electrons are highest in this region during the winter with typical E_{ave} values near 8.0 keV. The FAST data reveal that the high average energy precipitation in the poleward, pre-midnight region is associated with discrete auroral structures that are present prior to the onset of substorms. The FAST observations in the winter-time case (FAST orbit 1719) show quasi-monoenergetic energy spectra at a few keV between 68.0 - 70.5° MLAT, indicative of field-aligned potential acceleration. At the poleward edge of the auroral oval during this orbit, two field-aligned electron beams are observed: a downward beam extending in energy to about 5.0 keV followed by an upward beam with a peak energy of 100 eV. Field-aligned electron beams are also observed equatorward of the discrete auroral region with energies up to about 1.0 keV. These are embedded in diffuse precipitation less than about 5.0 keV.

The precipitating electron average energies prior to substorm onset during the equinoctial and summer periods are about a factor of two less in the high-latitude, pre-midnight auroral oval than in the winter-time case (Figure 4.13) although the global pattern of E_{ave} values is similar in each case. The FAST electron observations in the pre-midnight, pre-onset auroral oval for the equinoctial and summer cases are both characterized by small-scale discrete structures with peak energies between about 800 eV (summer) and 3.0 keV (equinox). Equatorward of these weak, discrete auroral features is diffuse precipitation as is typically observed.

Note that the average energy of the auroral electrons is also significantly higher by a factor of three on the dayside oval (0900-1500 MLT) during the winter in comparison with the equinoxes and summer. The precipitating electron energy flux on the other hand is greater during the summer than in either winter or the equinoxes. We will

discuss the characteristics of this dayside region separately in Section 4.3.7 since this part of the auroral oval is not involved in substorms.

4.3.2 Onset ($t = T_{\text{onset}}$)

The initial increase in incident energy flux (brightening of the aurora) near substorm onset is observed to be most intense during the winter periods and decrease in intensity during the equinoxes and summer (Figure 4.14, top row). The average energy of the electron precipitation in the onset region (2100-2400 MLT, 60-70° MLAT) is also highest for the winter-time events with values near 7.0 keV. We interpret the high E_{ave} values near 10.0 keV at the poleward edge of the pre-midnight winter-time aurora as the hardening of the precipitation in the discrete auroral region that is present prior to onset as shown in Figure 4.13. The average energy of the incident electrons at substorm onset for the equinoctial events is comparable to those observed during winter periods. We observe the lowest increase in the average energy in the electron precipitation during onset in the summer-time substorms where E_{ave} is typically less than 5.0 keV in breakup region.

Because the onset of substorm occurs over a short time scale (seconds to a few minutes) relative to the other substorm epochs, it is difficult to find coincident *in situ* observations within the onset region as an auroral breakup commences. However, we have identified a few fortuitous cases in which FAST traverses the pre-midnight auroral zone just as the onset of substorm commences. The bottom half of Figure 4.14 shows FAST electron measurements in the auroral onset region for the winter and equinox cases. We were not able to find coincident FAST observations at the onset of any substorm events observed during the summer periods in our study.

The winter-time example shows in Figure 4.14 occurred during at the onset of a substorm on January 26, 1997. Note that the color scale for the log energy flux for this event is increased by one decade over that used in the previously shown FAST spectra. The FAST measurements shown for the equinoctial case were taken during the onset of a substorm on September 10, 1997. The UVI images corresponding to these FAST

orbits are shown in Figures C.4 and C.5.

The most distinct feature observed in the electron measurements during substorm onset is intense, strongly field-aligned electron beams that are both upward and downward going at the poleward edge of the pre-midnight aurora that is just starting to expand toward higher latitudes. This feature is clearly seen between 13:35:30-13:36:30 UT during orbit 1710 (winter) and near 10:58 UT for orbit 4164 (equinox). The downward going electron beams extend to higher energies, up to 10.0 keV, than the upward going electron beams observed at the same time. Equatorward of these intense electron beams, the auroral structure is similar to that shown in the pre-onset examples for both cases shown in Figure 4.14: quasi-monoenergetic, discrete precipitation poleward of a region of diffuse precipitation. Field-aligned electron beams are also observed equatorward of this region but at lower energies, generally less than 300 eV.

4.3.3 Substorm expansion ($T_{\text{onset}} - T_{\text{HPmax}}$)

The global structure of the aurora shows the least seasonal differences during substorm expansion periods. Previous studies have noted that the precipitating energy flux is more intense by a factor of three for aurorae occurring in darkness versus those occurring when the nightside auroral oval is sunlit [Newell *et al.*, 1996, 2001; Liou *et al.*, 2001]. Figure 4.15 shows that incident energy flux values during substorm expansions in summer periods are only less than their winter and equinoctial counterparts by about 30%. The peak energy fluxes during the summer in the pre-midnight sector (2200-2400 MLT) have values near 7.0-8.0 ergs cm⁻² s⁻¹ while the winter-time and equinoctial energy flux has typical values near 10.0 ergs cm⁻² s⁻¹. The extent to which the substorms expand appears also to have little variation by season. The area in which the incident energy flux is greater than about 5.0 ergs cm⁻² s⁻¹ is comparable for the winter, equinoctial, and summer substorms.

Larger seasonal variations are observed when we examine the average energy of the electron precipitation during substorm expansion. The electron precipitation in the poleward region of the pre-midnight auroral oval is most energetic for the winter-

time substorms, reaching values upwards of 10.0 keV. The average energies in this region for the equinoctial and summer-time events are comparable during this substorm phase with values near 7.0 keV. During substorm expansion we observe a smaller variation, about 30%, in the average energy values between seasons than has been reported previously. The high average energy precipitation region extends toward earlier local times in each seasonal category to about 1800 MLT. The appearance of the highest E_{ave} values within the 1800-2100 MLT local time region is biased by the intense, high-energy (10.0-15.0 keV) electron precipitation associated with the westward surge as described in Section 3.1.

Another feature that emerges during the substorm expansion period is the appearance of 5.0-7.0 keV electron precipitation in the equatorward region of the post-midnight (0000-0300 MLT) auroral oval. This feature was also seen in the substorm case study presented in Section 3.1 and is interpreted as the precipitation of dawnward drifting electrons that have been injected earthward following substorm onset.

As the auroral oval continues to expand towards higher latitudes in the pre-midnight sector, the coincident FAST electron measurements reveal similar features to those observed near substorm onset. Intense, upward and downward going field-aligned electron beams continue to be seen at the poleward edge of the expanding aurora in the winter-time and equinoctial FAST orbits (1759 and 12443 respectively) shown in Figure 4.15. The peak energies of these electron beams are typically less than what is seen during onset, generally a few keV or less. In the winter-time and equinoctial FAST orbits, inverted-V structures are observed equatorward of the electron beams (Figure 4.15). The diffuse aurora observed equatorward of the discrete structures in each seasonal case is more intense by an order of magnitude in energy flux during substorm expansion than before onset.

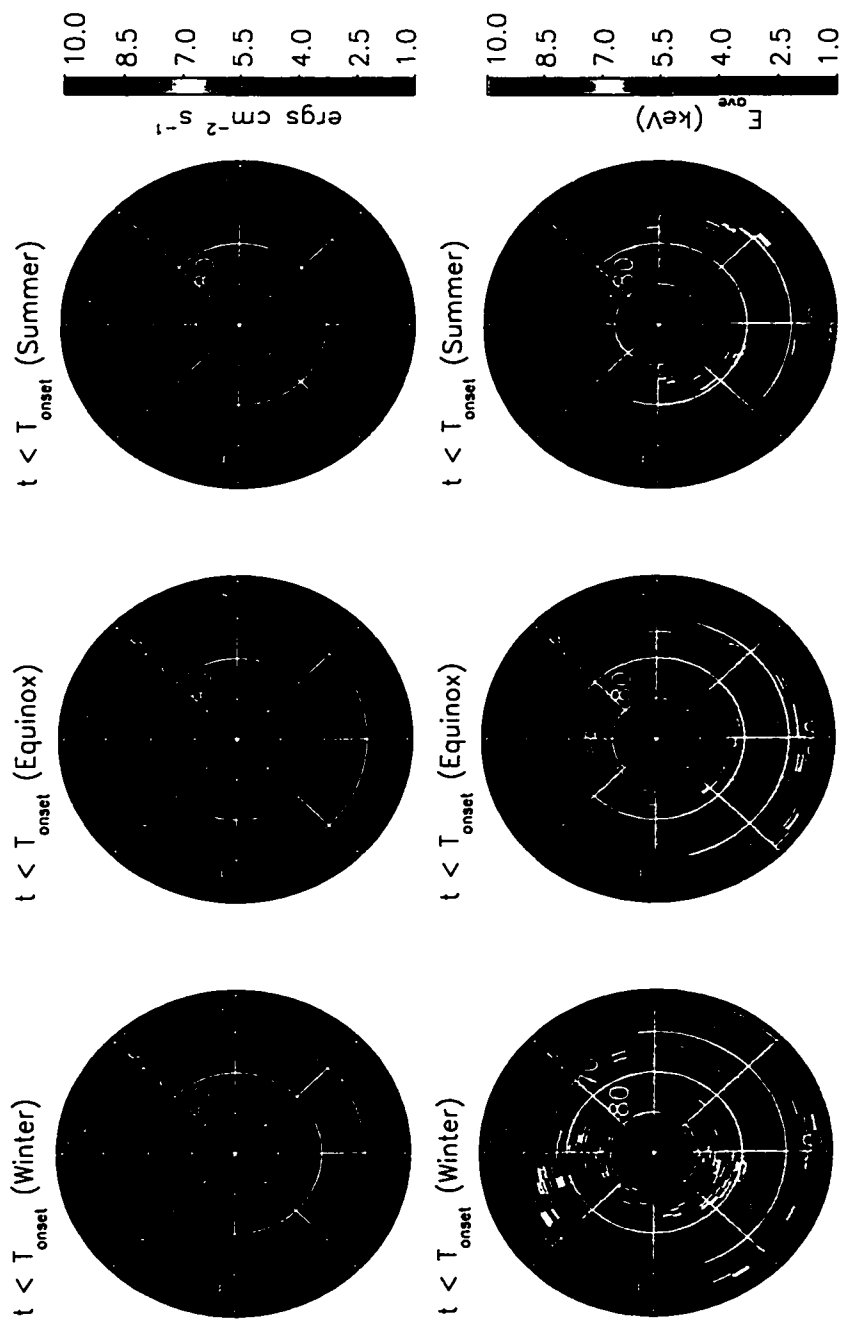
The intense inverted-V structure observed between 02:47:20-02:47:40 UT during FAST orbit 11102 shows that discrete aurora with peak energies 10.0 keV do occur during summer periods in contrast to the general results of previous studies describing the suppression of such structures when the auroral oval is sunlit. The FAST observations shown during the summer-time orbit of 11102 stands out from the winter-time

and equinoctial examples by the lack of field-aligned upward and downward electron beams at the poleward, expanding edge of the auroral oval. Note that the color scale has been adjusted in this case so as to not saturate the plots at the most intense energy flux values. The burst-like feature observed near 02:47:40 UT shows a broader distribution in pitch angle for the downward going electrons and appears nearly isotropic below 100 eV (fourth panel). Downward field-aligned electron beams are sometimes observed by FAST near the poleward expanding, pre-midnight auroral oval (see Figure C.10 in Appendix C for examples). However, we have not found any summer-time substorm cases where the FAST electron measurements have shown the upward and downward field-aligned electron beams typical of auroral expansions during the winter and equinoxes.

4.3.4 $T_{\text{HPmax}} - \tau$

After one e -folding time in the decay in hemispheric power during substorm recovery, we begin to see a departure between the characteristics of the sunlit substorm aurora and that observed in darkness during winter and the equinoxes. The energy flux of the precipitation during the winter and equinoctial substorms shows about a 25% reduction between expansion ($T_{\text{onset}} - T_{\text{HPmax}}$) and τ . In contrast, the energy flux during the summer time events is seen to fall by as much as a factor of two after one e -folding time of the hemispheric power.

The average energy of the electron precipitation in the pre-midnight substorm bulge has not changed significantly between the previous epoch and one HP e -folding time for the winter and equinox substorms. Electron precipitation with energies greater than 8.0 keV persists in the westward surge region near the poleward edge of the 1800-2200 MLT auroral oval for the winter-time substorms. Slightly less energetic precipitation, between 6.0-7.0 keV is seen during the equinoctial events. In this substorm epoch we observe a broad region across the midnight sector auroral oval with average energies between 5.5-7.0 keV in the winter-time and equinox periods. During this time we continue to observe higher average energy values along the equatorward portion of



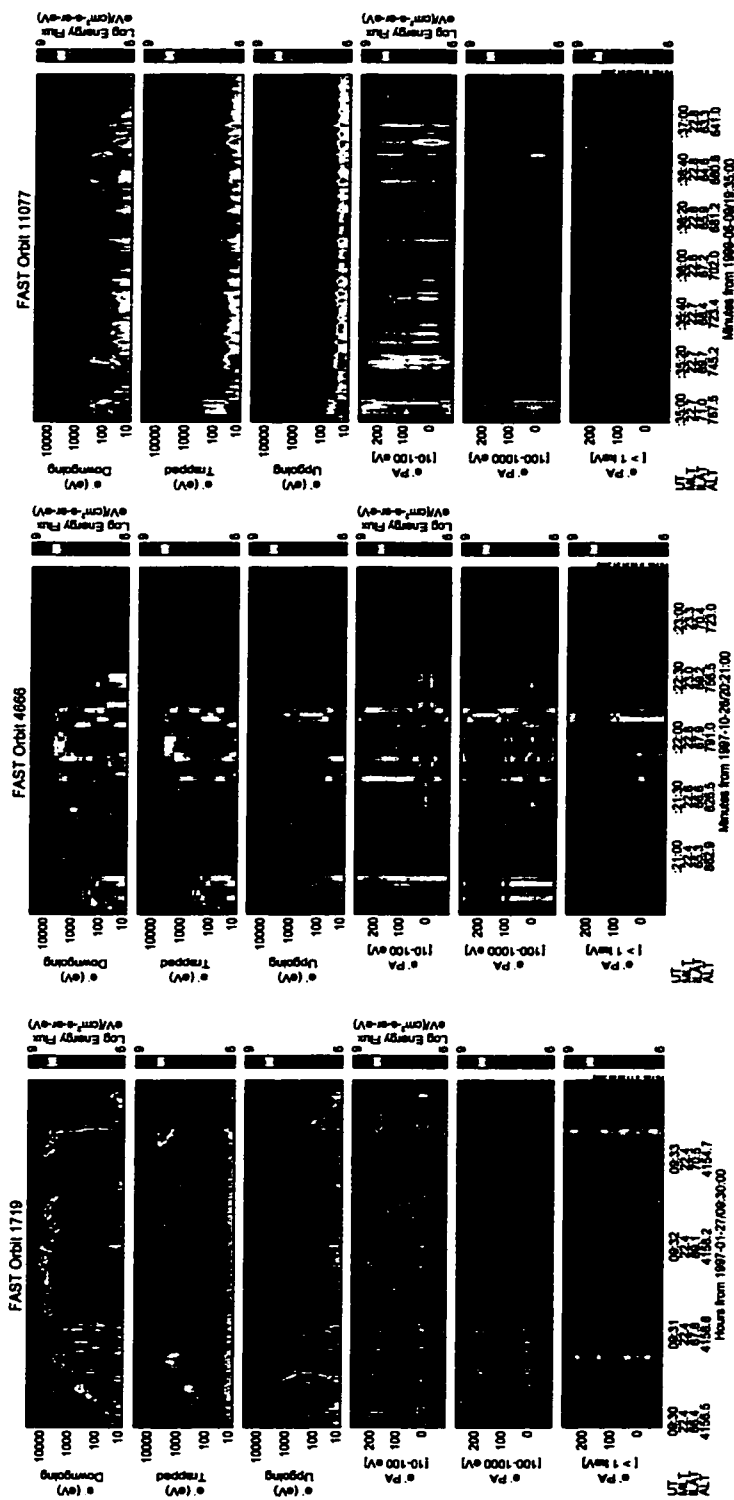
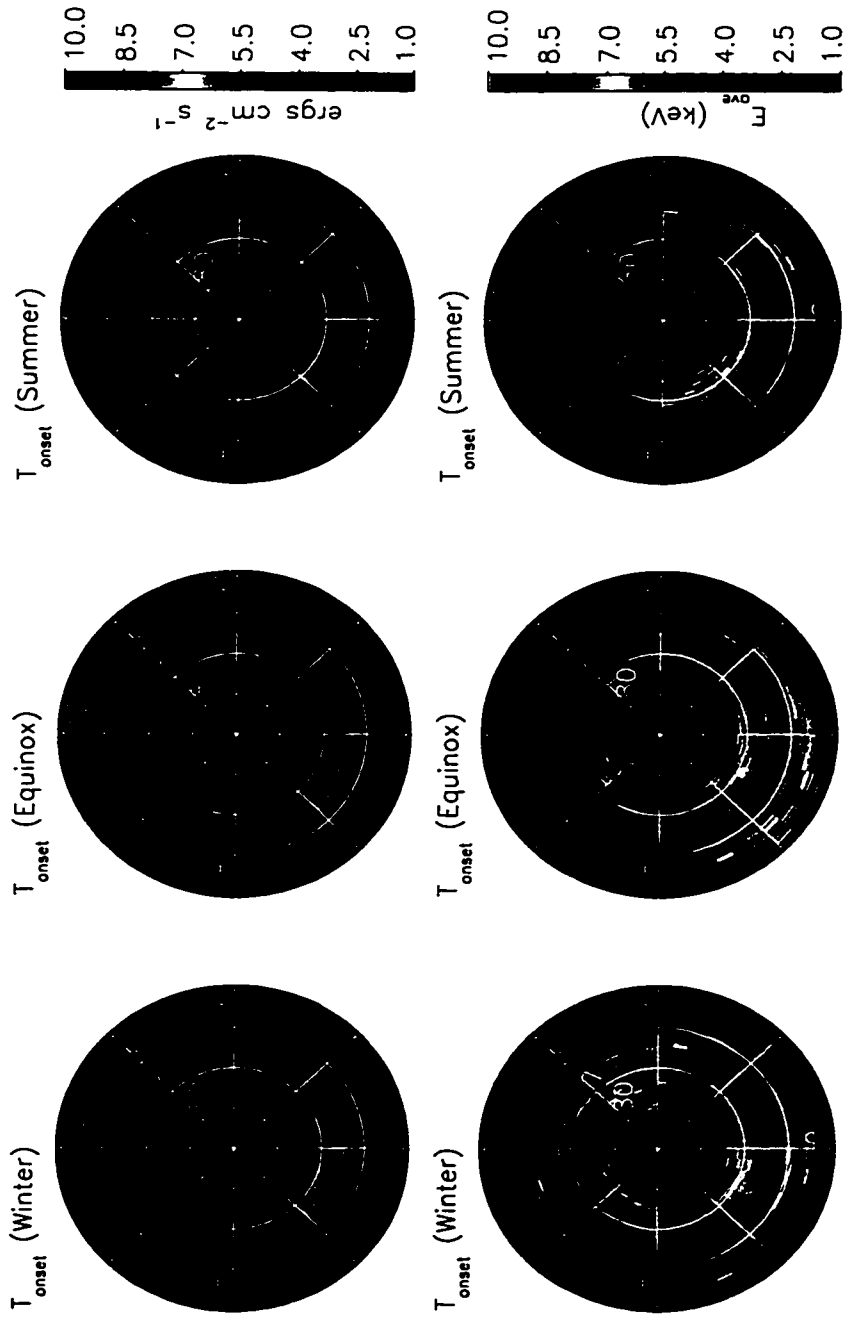


Figure 4.13: **Opposite Page:** Weighted averages of UVI derived auroral electron energy flux (top row) and average energy (bottom row) for winter (left column), equinoctial (middle column), and summer (right column) substorms during the pre-onset epoch ($t < T_{onset}$). **This Page:** Representative FAST electron energy-time and pitch angle spectrograms in the midnight sector during this epoch for each seasonal category.



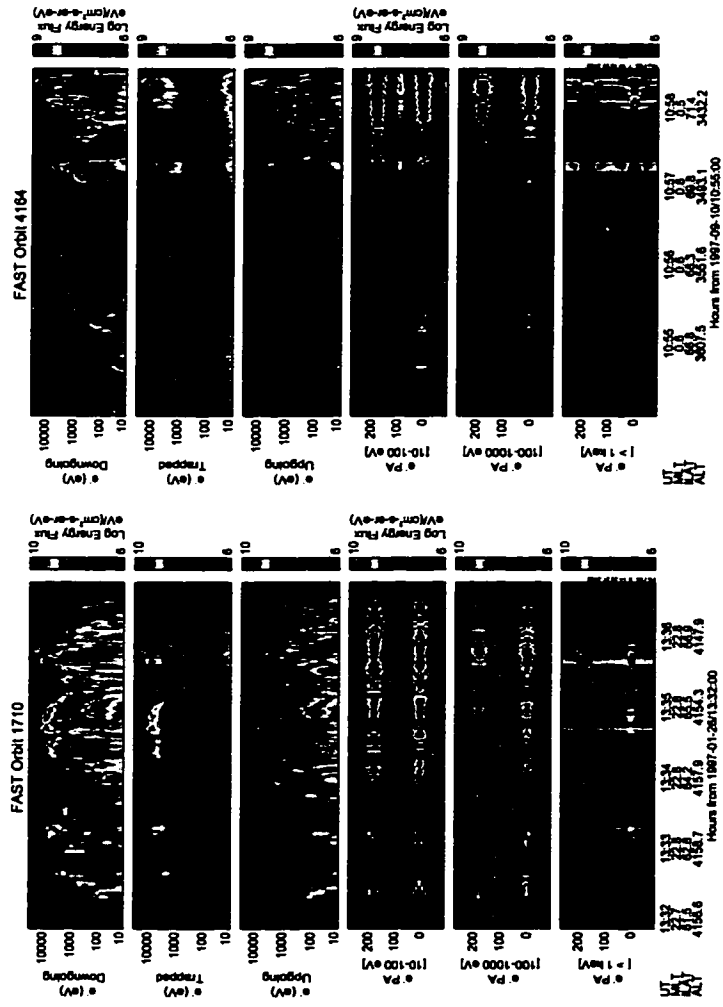
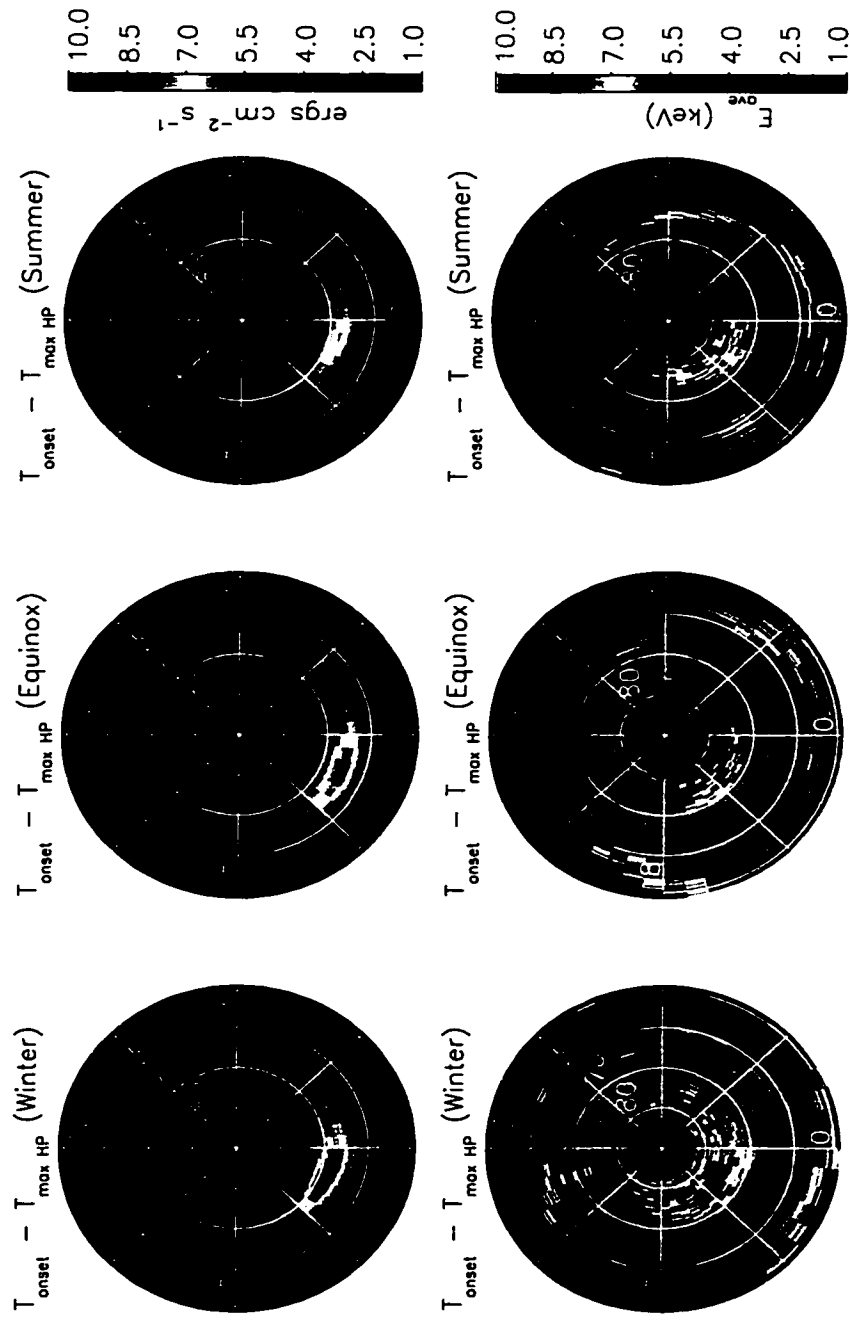


Figure 4.14: **Opposite page:** Weighted averages of UVI derived auroral electron energy flux (top row) and average energy (bottom row) for winter (left column), equinoctial (middle column), and summer (right column) events at substorm onset ($t = T_{\text{onset}}$). **This page:** FAST electron energy-time and pitch angle spectrograms over the substorm onset location for the winter (left) and equinox (middle), cases.



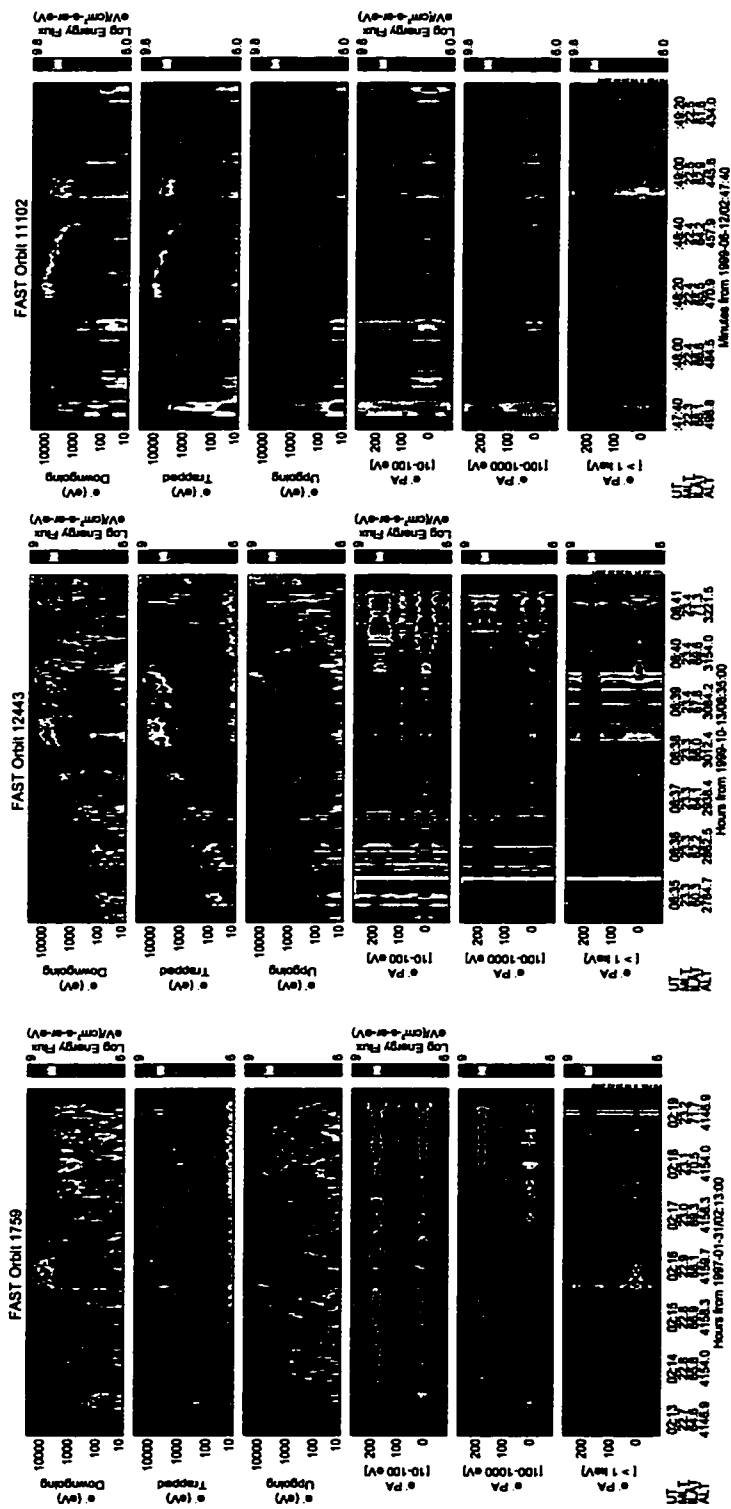
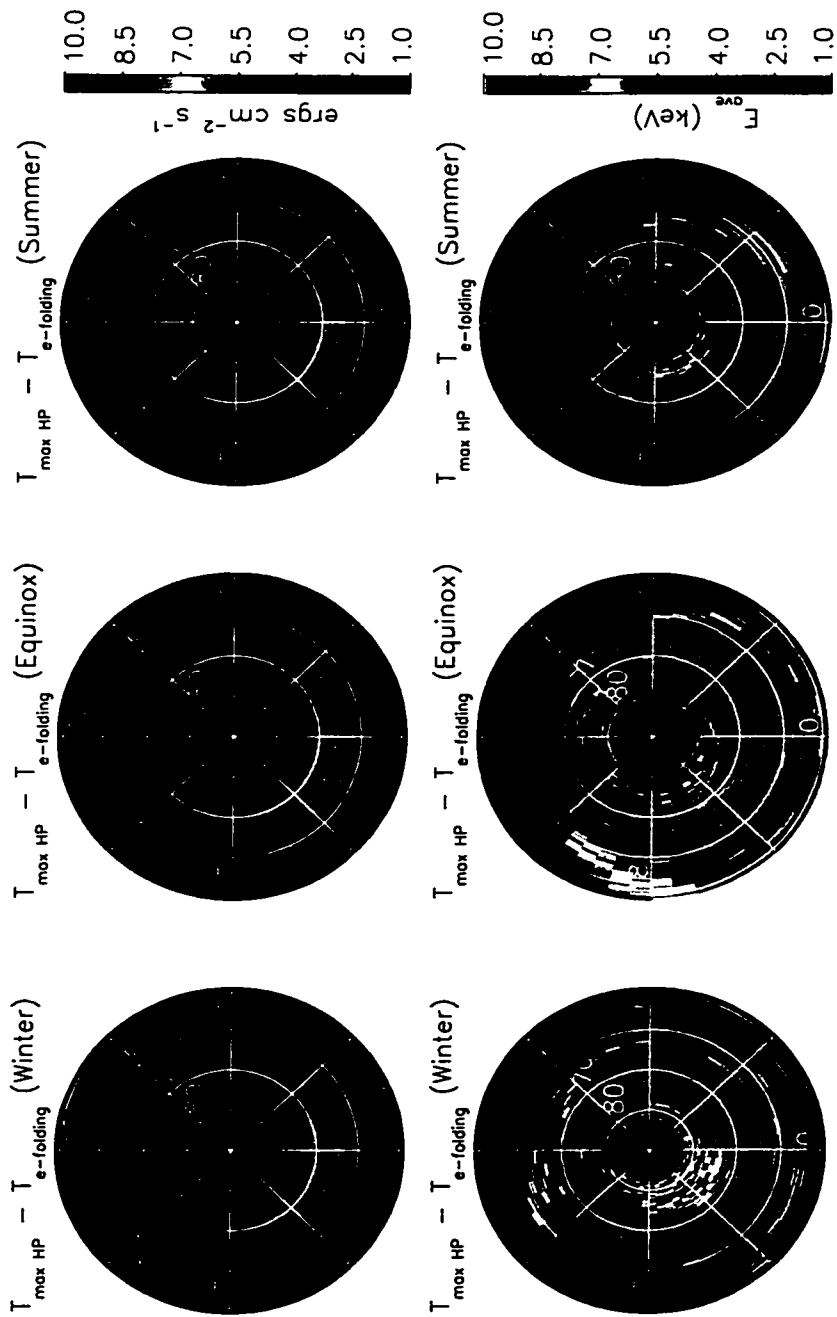


Figure 4.15: **Opposite page:** Weighted averages of UVI derived auroral electron energy flux (top row) and average energy (bottom row) for winter (left column), equinoctial (middle column), and summer (right column) events during substorm expansion ($T_{\text{onset}} - T_{\text{HPmax}}$). **This page:** Representative FAST electron energy-time and pitch angle spectrograms in the midnight sector for the winter (left), equinox (middle), and summer (right) cases. Note that the color scale for FAST orbit 11102 is extended to accommodate the intense energy flux values observed near 02:47:40 UT.



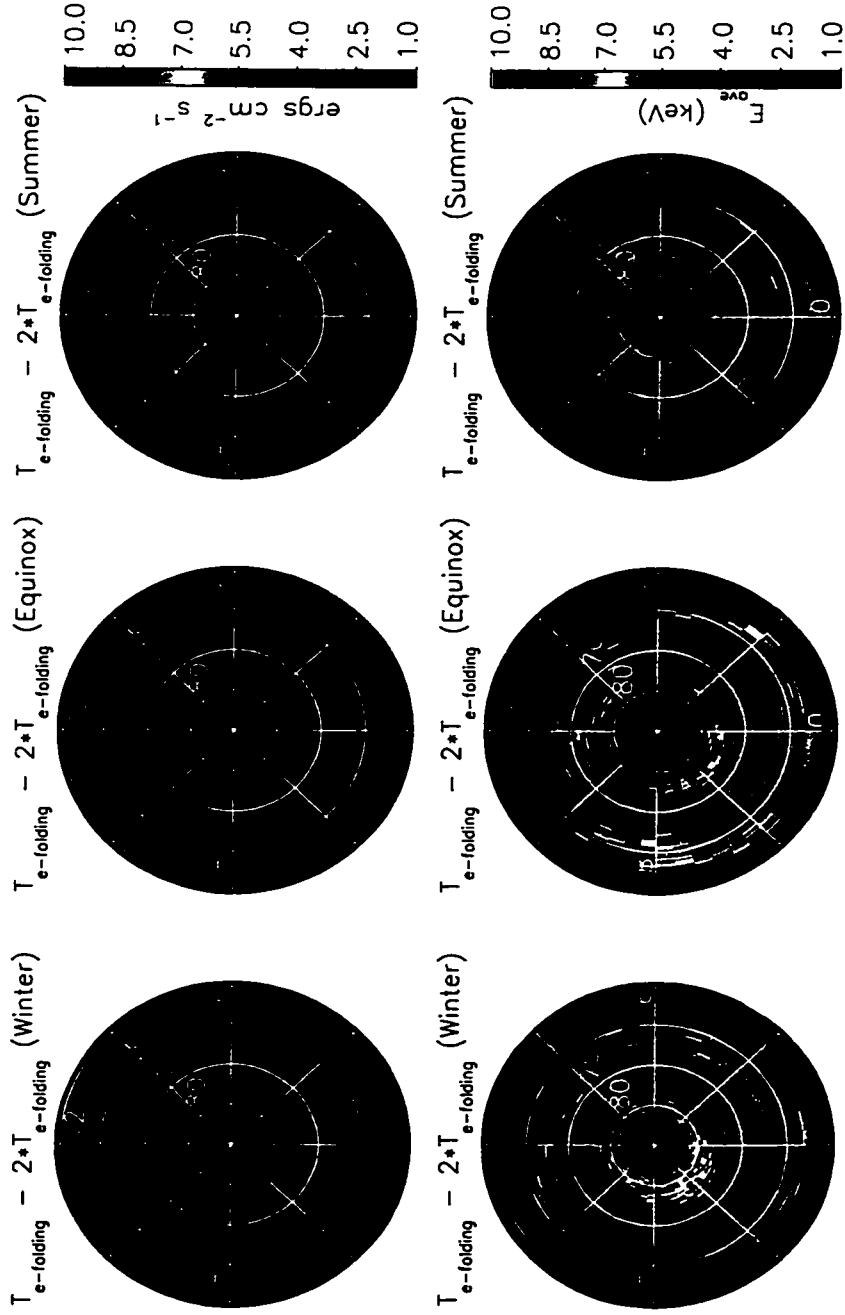
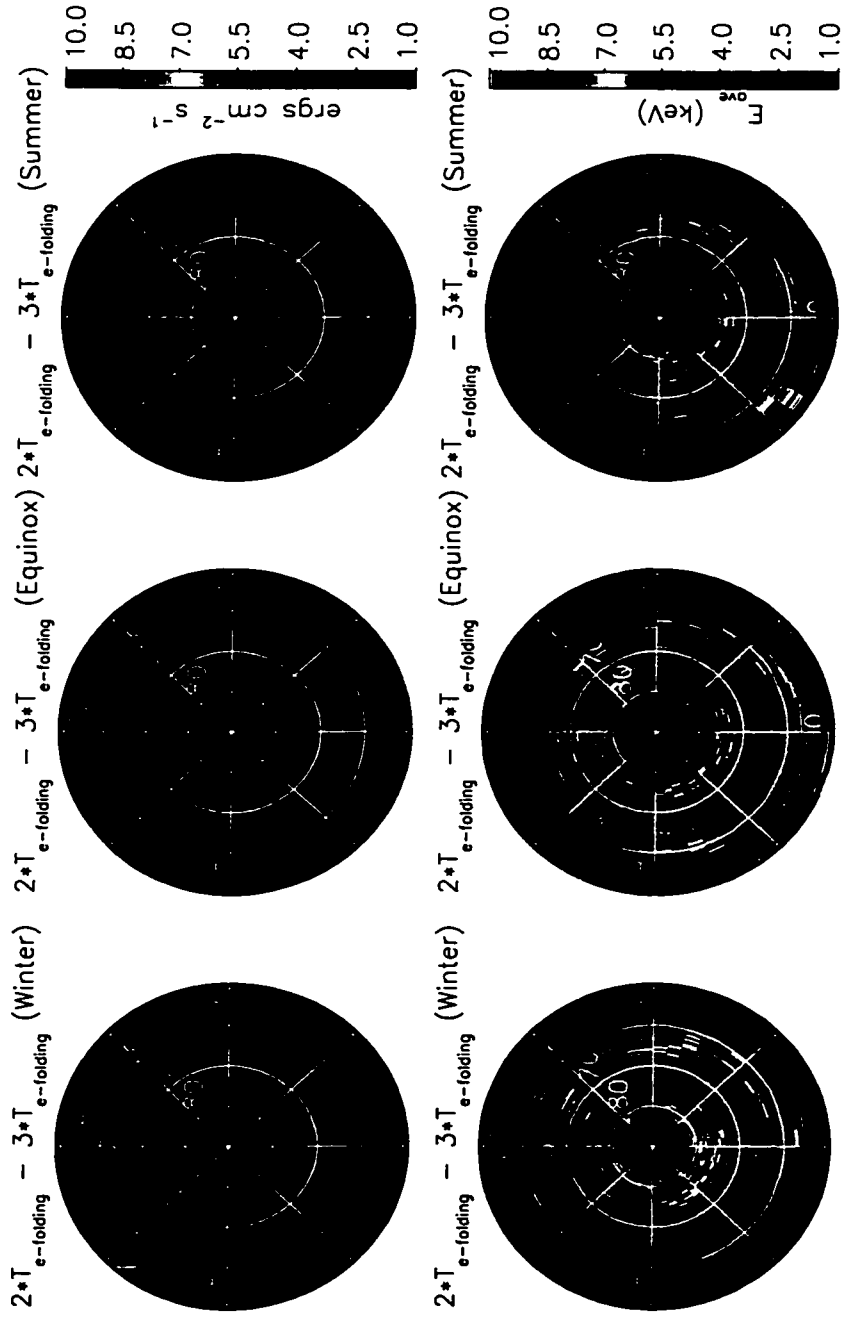




Figure 4.17: **Opposite page:** Weighted averages of UVI derived auroral electron energy flux (top row) and average energy (bottom row) for winter (left column), equinoctial (middle column), and summer (right column) events between $\tau - 2\tau$. **This page:** Representative FAST electron energy-time and pitch angle spectra in the midnight sector for each seasonal category.



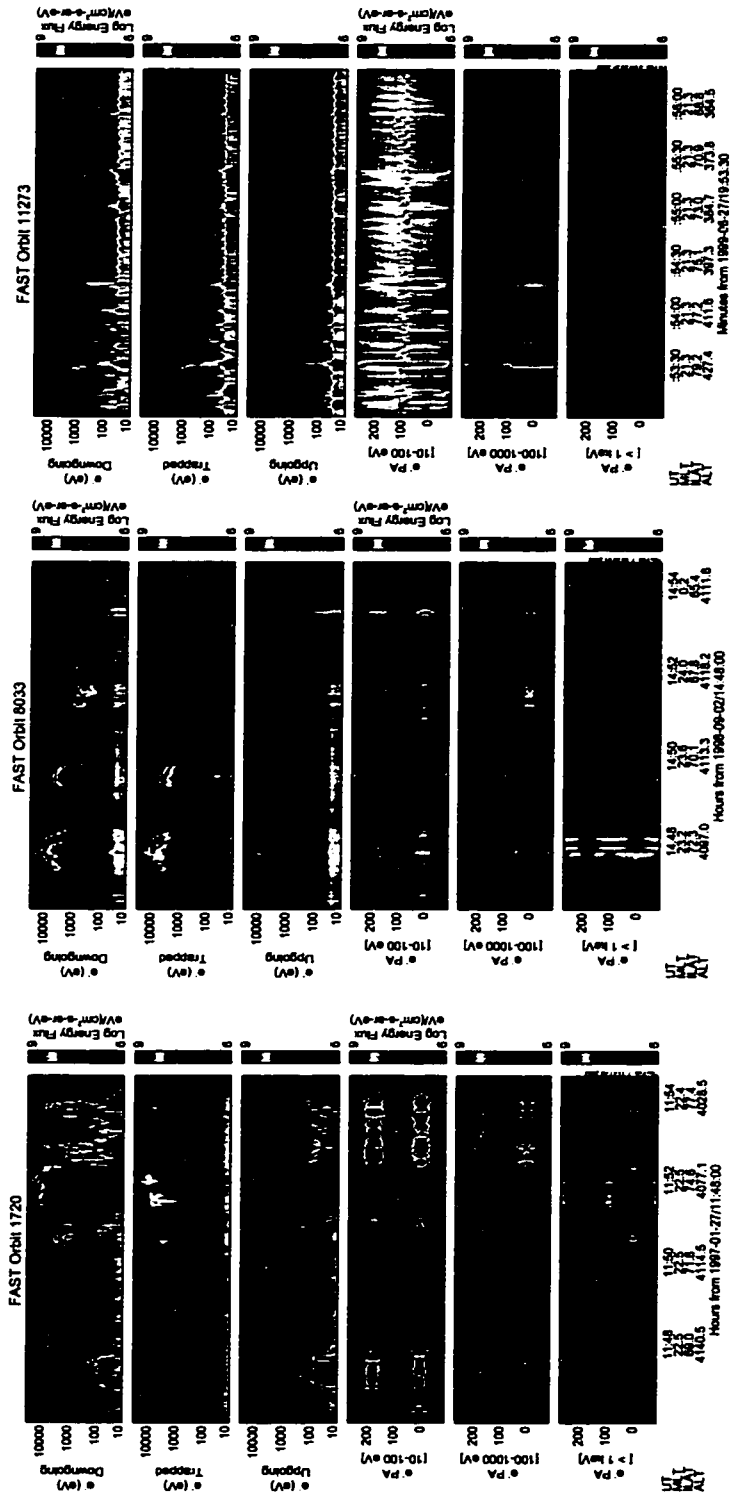


Figure 4.18: Opposite page: Weighted averages of UVI derived auroral electron energy flux (top row) and average energy (bottom row) for winter (left column), equinoctial (middle column), and summer (right column) events between 27 – 37). This page: Representative FAST electron energy-time and pitch angle spectra in the midnight sector for each seasonal category.

the morning sector oval between 60-65° MLAT in the winter-time and equinoctial substorms.

In contrast, the summer-time average energy image in Figure 4.16 shows that most of the energetic (> 8.0 keV) precipitation observed previously during substorm expansion in the westward surge region has largely diminished by one HP e -folding time. Precipitating electrons with average energies greater than 6.0 keV are only seen in a localized region near 75° MLAT between 1800-2100 MLT and near the equatorward portion of the morning sector oval. Average energy values throughout the midnight sector are generally less than 5.5 keV for the summer-time substorms in the $T_{\text{HPmax}} - \tau$ phase.

The FAST electron measurements in the pre-midnight sector during this substorm epoch ($T_{\text{HPmax}} - \tau$) show similar features as those taken during substorm expansion (Figure 4.15) for the winter and equinox cases. Intense, bi-directional field-aligned electron beams at the poleward edge of the auroral oval continue to be seen in the winter and equinox periods when the nightside aurora is in darkness. Equatorward of this region we generally now observe diffuse aurora as shown in orbits 5644 and 1910 for the winter and equinox cases. This is consistent with the broad, unstructured regions of precipitation with average energies between 5.5-7.0 keV seen in the UVI average energy plots. The FAST electron measurements for the summer-time example in Figure 4.16 reveals diffuse precipitation throughout the pre-midnight sector during this substorm phase. There is some indication of field-aligned structure for electrons below 1.0 keV near 12:02:09 UT during orbit 14999 but these are unlike the intense bi-directional electron beams extending to a few keV energies seen at the poleward edge of the pre-midnight winter and equinox aurora.

4.3.5 $\tau - 2\tau$

By the time substorms have reached two e -folding times of the hemispheric power, the incident energy flux is comparable for events occurring in each of the three seasonal categories with typical values across the nightside aurora of $3.0\text{-}4.0$ ergs cm^{-2} s^{-1} .

However, we observe a strong seasonal variance in the average energy of the precipitation after two HP e -folding times. The global distribution of average energies for the summer events during this epoch more closely resembles that prior to substorm onset whereas enhanced average energies relative to pre-onset values persist through this period for the winter and equinox cases. Electron precipitation with average energies greater than 6.0 keV persists through this substorm phase in the pre-midnight substorm oval for both the winter and equinox cases. The winter-time and equinoctial average energy images in Figure 4.17 have not changed significantly since the previous substorm phase. In contrast, the region of enhanced electron precipitation energies in the pre-midnight sector is no longer observed during summer-time substorms after two e -folding times of the hemispheric power.

The winter-time FAST data for orbit 5590 (Figure 4.17 shows similar features to those observed during expansion and early recovery: bi-directional field-aligned electron beams at the poleward boundary of the auroral oval, inverted-V forms with 4.0-5.0 keV peak energies, and diffuse auroral precipitation equatorward of the discrete structures. The FAST measurements during orbit 7979 in the equinoctial example show the familiar discrete, inverted-V signature near the poleward portion of the oval followed by diffuse precipitation that extends to the top of the energy range (30 keV) for the electrons in this case. In the summer-time orbit of 3207, diffuse precipitation dominates what is observed throughout the auroral oval during this pass. A weak inverted-V signature is observed near 23:55 UT during this orbit in addition to an intense and localized downward electron beam with energies extending up to about 3.0 keV at the poleward boundary. No accompanying downward beam is seen however as in most of the winter-time FAST observations throughout substorms.

4.3.6 $2\tau - 3\tau$

After three e -folding times of the hemispheric power, we observe little difference in the global characteristics of the auroral oval from the previous substorm epoch. The same seasonal differences in the precipitating electron average energies seen after 2τ

continue through this period.

The upward and downward field-aligned electron beams observed by FAST throughout winter-time substorm events continue to be seen through this substorm phase as shown in data for orbit 1720 (Figure 4.18). However, we see that the peak energies in the electron beams are only about 100 eV in this case. Discrete auroral forms continue to be observed for equinoctial FAST measurements in this substorm epoch. The summer-time FAST example during this period (orbit 11273) reveals mostly diffuse aurora throughout the auroral oval.

4.3.7 Dayside auroral characteristics

Although not directly related to the substorm variations described above, we also observe seasonal variations of the characteristics of the auroral precipitation on the dayside oval as shown in Figures 4.13 -4.18. The average incident energy flux in the 0900-1500 MLT sector during the winter and equinoctial periods is below $1.0 \text{ erg cm}^{-2} \text{ s}^{-1}$ which is less than the nominal threshold of the UVI instrument. We therefore typically observe an absence of auroral emissions in this local time sector during the winter and equinoxes. This feature has been previously identified by *Dandekar and Pike* [1978] as the midday auroral gap. In contrast, the precipitating electron energy flux is enhanced to values between $1.0\text{-}3.0 \text{ ergs cm}^{-2} \text{ s}^{-1}$ during the summer intervals.

The average energy of the dayside electron precipitation has the opposite variation in this local time sector. The average energy of the winter-time, dayside electron precipitation increases with decreasing latitude, ranging from about 5.0 keV near 70° MLAT to 8.0-9.0 keV at 60° . The average energy images for the equinoctial and summer-time observations do not exhibit the latitudinal variation on the dayside. The average energy of the dayside electron precipitation appears slightly higher during the equinoctial periods, between 5.0-7.0 keV, than during the summer when the values are typically below 3.0 keV. In general we observe a higher flux of lower energy electron precipitation during summer periods. The opposite is true for winter-time observations when the dayside auroral oval is in darkness: a lower flux of higher average energy

precipitation is seen.

4.3.8 Comparison to earlier studies

As a check on the superposed epoch analysis presented above, we average our seasonal values for auroral energy flux and mean energy over each substorm epoch (phase) for comparison with the results of *Liou et al.* [2001] who computed bulk averages of these two quantities over the winter and summer seasons without regard to substorms. Our gross seasonal averages of incident energy flux and mean energy are shown in Figure 4.19.

The winter-time incident energy flux averaged over substorm phase has typical values in the pre-midnight sector of $5.0 \text{ ergs cm}^{-2} \text{ s}^{-1}$. The equinoctial energy flux values in this region are slightly less, around $4.8 \text{ ergs cm}^{-2} \text{ s}^{-1}$. The summer-time energy flux in the pre-midnight region has an average value near $3.8 \text{ erg cm}^{-2} \text{ s}^{-1}$, lower than the winter-time values by a factor of 1.3. The average energy values of the winter-time electron precipitation in the pre-midnight auroral oval are typically 7.0-9.0 keV. This is roughly a factor of two greater than the incident electron average energies observed in the summer time in this region which are generally near 5.0-5.5 keV. In the pre-midnight region, *Liou et al.* [2001] obtained a ratio of about 1.33 in the winter to summer energy flux. Their ratio in winter to summer precipitating electron average energy in the pre-midnight sector is about two. These results are in good agreement with our seasonal averages of incident energy flux and mean energy shown in Figure 4.19.

On the dayside, between 0900-1500 MLT, the bulk seasonal averages of the energy flux and mean energy show the same features as we noted when examining these quantities in each substorm phase. The dayside incident energy flux values during the summer are generally between $1.6\text{-}2.0 \text{ ergs cm}^{-2} \text{ s}^{-1}$ whereas during the winter they range between $0.5\text{-}1.0 \text{ ergs cm}^{-2} \text{ s}^{-1}$ (Figure 4.19). The precipitating electron average energies on the dayside are higher in the winter versus summer by about a factor of two. The gross seasonal averages of the characteristics of electron precipitation that

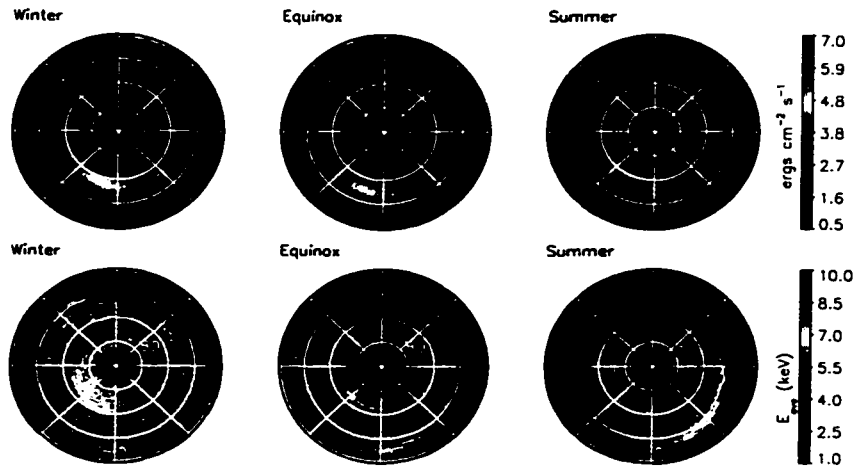


Figure 4.19: UVI inferred energy flux and mean energy averaged over all substorm epochs and sorted by season. We reproduce the results of *Liou et al.* [2001] when averaging the energy flux and E_{ave} over substorm phase.

we compute on the dayside are consistent with those described by *Liou et al.* [2001] who give the winter to summer ratio of energy flux as about 1.5. Their winter to summer ratio in the precipitating electron average energy on the dayside is 2.0-2.5. The differences in the winter to summer dayside electron precipitation characteristics obtained by UVI are also consistent with earlier studies of seasonal variations in dayside cusp precipitation that used particle measurements [*Newell and Meng, 1988*].

Our results are consistent with those of *Liou et al.* [2001] who examined long-term, seasonal averages of the UVI inferred energy flux and average energy. When averaging the incident energy flux and mean energy values over the substorm epochs (phases) defined in Section 4.1, we are able to reproduce the earlier results of *Liou et al.* [2001].

4.4 Summary of observations

The shape of the hemispheric power versus time curve during substorms varies according to the orientation of the IMF B_z component. The hemispheric power is shown to decay back to its pre-onset values during substorm recovery under northward IMF

conditions while it is sustained well above pre-onset values during southward IMF. We find that substorms that occur under southward IMF conditions have longer expansion and decay times than events for which the IMF was northward. The variations in the substorm time scales with IMF B_z orientation were less than 40%.

Our analysis of the hemispheric power derived from UVI images has shown that substorm time scales show the strongest variation as a function of season. The substorm recovery time scale, τ , derived from the exponential decay of the hemispheric power, is shorter by a factor of two when the auroral zone is sunlit. Equinoctial and winter-time substorms, periods when the nightside auroral oval is in darkness have comparable time scales. Auroral acceleration signatures in both the UVI and FAST observations persist in the pre-midnight substorm region through three HP e -folding times in the winter-time and equinoctial cases. Indications of auroral acceleration during summer-time substorms are largely diminished after just one e -folding time in the hemispheric power.

The strongly field-aligned, bi-directional electron beams observed by FAST at the poleward edge of the auroral oval have been identified by *Chaston et al.* [2000]; *Chaston* [2001] as the result of field-aligned acceleration by Alfvén waves that have a field-aligned component of their electric field. Our observations suggest that this is a winter-time phenomenon associated with small-scale discrete auroral structures during substorms. Downward electron beams are observed when the auroral zone is sunlit but simultaneously occurring upward beams are not generally seen.

Table 4.1: The main auroral features during each substorm epoch are given for events in each of the three seasonal categories. The canonical substorm phases are indicated in parentheses.

| Substorm epoch defined by HP | Canonical Substorm Phase | Winter | Equinox | Summer |
|--|--------------------------|---|---|--|
| $t < T_{\text{onset}}$ | Pre-onset (growth phase) | Quiet discrete arcs near poleward portion of auroral oval in 2000-2300 MLT region. Diffuse aurora elsewhere. | Quiet discrete arcs near poleward portion of auroral oval in 2000-2300 MLT region. Diffuse aurora elsewhere. | Mostly diffuse aurora throughout auroral oval. |
| T_{onset} | Onset, Breakup | Bi-directional, field-aligned electron beams with energies up to 10 keV. Localized brightening of aurora (enhancement of precipitating electron energy flux). | Bi-directional, field-aligned electron beams with energies up to 10 keV. Localized brightening of aurora (enhancement of precipitating electron energy flux). | Brightening of aurora (enhancement in incident electron energy flux) not as intense as winter/equinoctial substorm onsets. |
| $T_{\text{onset}} - T_{\text{HP max}}$ | Expansion | Increase in auroral oval area and incident energy flux. Bi-directional field-aligned e^- beams with energies 5 keV. Discrete (inverted-V) structures equatorward of e^- beams. Enhancement of energy flux and average energy in diffuse aurora equatorward of discrete structures. | Increase in auroral oval area and incident energy flux. Bi-directional field-aligned e^- beams with energies 5 keV. Discrete (inverted-V) structures equatorward of e^- beams. Enhancement of energy flux and average energy in diffuse aurora equatorward of discrete structures. | Increase in auroral oval area and incident energy flux. Downward electron beams. Discrete (inverted-V) structures equatorward of e^- beams. Enhancement of energy flux and average energy in diffuse aurora equatorward of discrete structures. |

| | | | | |
|--------------------|-----------------|--|--|---|
| $T_{HPmax} - \tau$ | Recovery | <p>Decrease in incident energy flux.; only slight decrease in average energy</p> <p>Bi-directional field-aligned e⁻ beams with energies 1 keV.</p> <p>Discrete (inverted-V) structures equatorward of e⁻ beams.</p> <p>Diffuse auroral precipitation equatorward of discrete structures.</p> | <p>Decrease in incident energy flux; only slight decrease in average energy.</p> <p>Bi-directional field-aligned e⁻ beams with energies 1 keV.</p> <p>Discrete (inverted-V) structures equatorward of e⁻ beams.</p> <p>Diffuse auroral precipitation equatorward of discrete structures.</p> | <p>Decrease in precipitating electron energy flux and average energy.</p> <p>Downward e⁻ beams in poleward, pre-midnight oval.</p> <p>Weak discrete structures with peak energies a few keV.</p> |
| $\tau - 2\tau$ | Recovery | <p>Decrease in incident energy flux and average energy.</p> <p>Bi-directional field-aligned e⁻ beams with energies 500 eV.</p> <p>Discrete (inverted-V) structures equatorward of e⁻ beams.</p> <p>Diffuse auroral precipitation equatorward of discrete structures.</p> | <p>Decrease in incident energy flux and average energy.</p> <p>Discrete (inverted-V) structures equatorward of e⁻ beams.</p> <p>Diffuse auroral precipitation equatorward of discrete structures.</p> | <p>Precipitating electron energy flux and average energy near pre-onset levels.</p> <p>Weak discrete structures with peak energies a few keV.</p> |
| $2\tau - 3\tau$ | Recovery | <p>Same as above</p> | <p>Same as above.</p> | <p>Diffuse aurora dominates.</p> |

Chapter 5

SUMMARY AND CONCLUSIONS

The quantitative analysis of global auroral images from Polar UVI in this dissertation reveals differences in the mechanisms producing global scale auroral brightenings during isolated substorms and storm-time, pressure pulse driven intensifications. UVI observations of auroral electron energy flux and average energy show that these two parameters are structured in both magnetic local time (longitude) and magnetic latitude during substorms. Regions where we observe electron precipitation with average energies on the order of 10 keV are found along the poleward boundary of the pre-midnight auroral oval and the equatorward portion of the post-midnight, morning sector oval. This pattern is consistent with where one expects to find upward field-aligned current regions [Iijima and Potemra, 1978]. *In situ* FAST electron measurements reveal that these are regions of discrete aurora with signatures such as inverted-V structures that indicate field-aligned potential acceleration. Two features suggest that the auroral acceleration region is not as important in governing the properties of electron precipitation during magnetic storm-time, pressure pulse related intensifications: the lower average energy of the electron precipitation and the lack of discrete structure in the E_{ave} images. In the cases that we have studied, we find that CME-related pressure pulses do not trigger auroral intensifications that are well-described as substorms.

We have devised a new method for defining substorm phases based on the temporal behavior of the UVI derived hemispheric power. Calculations of hemispheric power allows us to quantitatively measure four global parameters important to substorms from our optical observations: (1) the peak hemispheric power value, which is used as a proxy for substorm intensity or magnitude, (2) substorm expansion time, (3) the hemispheric power characteristic decay time (τ), and (4) the total energy deposition by auroral electron precipitation during each substorm. These parameters were computed

for over 300 substorms which were sorted by season (summer, winter, and equinox) and IMF B_z orientation (northward or southward). On average we find that the peak hemispheric power was about 25% larger for substorms occurring during southward IMF B_z . We showed the peak hemispheric power did not vary significantly as a function of season. This also indicates that our seasonal comparison of the other global substorm parameters was not biased by any variations of substorm intensity with season.

We demonstrated that the characteristic decay time of the hemispheric power during substorms varied more strongly with season than IMF B_z orientation. We find that τ is a factor of two shorter on average for substorms occurring when the nightside auroral zone is sunlit in comparison to when it is darkness during the winter and equinox periods. The average hemispheric power e -folding time was only about 37% larger for substorms when the IMF was southward versus when it was northward. We find that the suppression of discrete aurora under enhanced ionospheric conductivity is better explained by the observation that such discrete structures have shorter lifetimes in the summer hemisphere. Earlier statistical studies of the seasonal dependence of auroral precipitation averaged out variations in the aurora on substorm time scales which in this study is measured by τ , the characteristic decay time of the hemispheric power.

Previous statistical studies of the seasonal dependence of auroral structure have focused on contrasting the characteristics of the aurora near winter and summer solstice when the nightside auroral oval is either in complete darkness or sunlit. We generalized our seasonal analysis of the aurora to include events occurring near the equinoxes in addition to periods near winter and summer solstice. We do not find any substantial differences in the characteristics of auroral precipitation during winter-time and equinoctial substorms. Our examination of substorm events that occurred in summer-time ionospheric conditions revealed indications of discrete auroral features such as inverted-V signatures that were generally thought to be suppressed when the aurora is sunlit. In fact, the observed energy flux and average energy of auroral electron precipitation during substorm expansion show little differences with season. However, we showed that these discrete auroral features during the summer-time events were short lived relative to those observed during winter and the equinoxes when the auroral zone

is in darkness. The departure of the summer-time substorm characteristics from those observed during winter and the equinoxes supports the hypothesis that enhanced levels of ambient ionospheric conductivity retards the mechanisms involved in producing intense, discrete auroral forms via field-aligned acceleration of precipitating electrons.

Our study of seasonal variations in auroral substorm dynamics adds a new level of understanding to previous statistical studies on the effect of enhanced ionospheric conductivity on aurora. Moreover, when we averaged our observations of precipitating electron energy flux and average energy over substorm phase, we were able to reproduce the results of earlier studies of seasonal variations in the aurora: a winter to summer ratio in energy flux of about 1.3 and a factor of two increase in average energy from summer to winter [Liou *et al.*, 2001]. This dissertation provides further evidence for the emerging view that the ionospheric boundary conditions at the foot of auroral field lines play a significant role in determining both the synoptic scale structure of the aurora and the dynamical time scales of magnetospheric substorms.

5.1 Future work

The results presented in this thesis point to the importance of conjugate auroral studies in fully understanding the electrodynamics of the aurora and the coupling of the magnetosphere and ionosphere. Some observations that diffuse auroral forms are conjugate but discrete structures are not [Stenbaek-Nielsen and Otto, 1997] point to further examinations of the role of ionospheric conductivity. Simultaneous, global observations of both northern and southern auroral zones will be essential in validating the idea that the boundary conditions in the ionosphere play a large role in determining both the spatial and temporal evolution of aurora.

We also showed in a qualitative sense that intense, bi-directional electron beams extending to keV energies are common features near the poleward boundary of the nightside auroral oval. These electron beams are thought to be the result of field-aligned acceleration by Alfvén waves [Chaston *et al.*, 2000; Chaston, 2001]. The association of these features with substorm expansion activity implies that the acceleration

of electrons by Alfvén waves may play a larger role in determining discrete auroral structures than is currently recognized.

The strong bias in the appearance of intense, bi-directional electron beams at the poleward boundary of the aurora during conditions of low ambient ionospheric conductivity remains to be explained in detail. Under the assumption that these structures are associated with Alfvén waves, one possible explanation may be found in the behavior of these waves at the ionospheric boundary. The reflection of Alfvén waves at the ionospheric boundary is largely controlled by the ratio of the height integrated conductivities to an effective Alfvén conductivity defined as $\Sigma_A = c^2/4\pi V_A$, where V_A is the Alfvén velocity [Lysak, 1991, and references therein]. Another way to look at this is to consider the large jump in the Alfvén velocity between the ionosphere and magnetosphere. The reflection coefficient is given in Lysak [1991] as

$$R = \frac{\Sigma_A - \Sigma_P}{\Sigma_A + \Sigma_P} \quad (5.1)$$

Therefore, when the effective Alfvén conductivity and the Pedersen conductivity match, there is no reflection of the Alfvén wave. If this condition applies for the summer-time auroral zone, this could explain why electron beams observed during this season were only observed in the downward direction if they were seen at all. A synthesis of models describing Alfvén wave propagation and their effects on auroral electron acceleration with auroral observations such as that presented in this thesis is needed to better understand the role of Alfvénic structures in the aurora.

BIBLIOGRAPHY

- Ajello, J. M., and D. E. Shemansky, A reexamination of important N₂ cross sections by electron impact with applications to the dayglow: The Lyman-Birge-Hopfield band system and NI (119.99 nm), *J. Geophys. Res.*, *90*, 9845, 1985.
- Akasofu, S.-I., The development of the auroral substorm, *Planet. Spa. Sci.*, *12*, 273, 1964.
- Akasofu, S.-I., *Polar and Magnetospheric Substorms*, D. Reidel Publishing Company, Dordrecht, Holland, 1968.
- Akasofu, S.-I., and S. Chapman, The lower limit of latitude (US sector) of northern quiet auroral arcs, and its relation to D_{st}(H), *J. Atmos. Terr. Phys.*, *25*, 9, 1963.
- Akasofu, S.-I., and C.-I. Meng, A study of polar magnetic substorms, *J. Geophys. Res.*, *74*, 293, 1969.
- Akasofu, S.-I., S. Chapman, and C.-I. Meng, The polar electrojet, *J. Atmos. Terr. Phys.*, *27*, 1275, 1965.
- Akasofu, S.-I., D. S. Kimball, and C.-I. Meng, Dynamics of the aurora, 5, Poleward motions, *J. Atmos. Terr. Phys.*, *28*, 497, 1966a.
- Akasofu, S.-I., C.-I. Meng, and D. S. Kimball, Dynamics of the aurora, 4, Polar magnetic substorms and westward traveling surges, *J. Atmos. Terr. Phys.*, *28*, 489, 1966b.
- Akasofu, S.-I., R. H. Eather, and J. N. Bradbury, The absence of the hydrogen emission (H β) in the westward traveling surge, *Planet. Spa. Sci.*, *17*, 1409, 1969.
- Anger, C. D., et al., An ultraviolet auroral imager for the Viking spacecraft, *Geophys. Res. Lett.*, *14*, 387, 1987.

- Arnoldy, R. L., and K. W. Chan, Particle substorms observed at the geostationary orbit, *J. Geophys. Res.*, *74*, 5019, 1969.
- Bale, S. D., M. J. Reiner, J. L. Bougeret, M. L. Kaiser, S. K. an D. E. Larson, and R. P. Lin, The source region of an interplanetary type II radio burst, *Geophys. Res. Lett.*, *26*, 1573, 1999.
- Barcus, J. R., and T. J. Rosenberg, Energy spectrum for auroral-zone x-rays, 1, Diurnal and type effects, *J. Geophys. Res.*, *71*, 803, 1966.
- Berko, F. W., and R. A. Hoffman, Dependence of field-aligned electron precipitation occurrence on season and altitude, *J. Geophys. Res.*, *79*, 3749, 1974.
- Boyd, J. S., Rocket-borne measurements of auroral electrons, *Rev. Geophys.*, *13*, 735, 1975.
- Brice, N., Morphology of elementary magnetospheric substorms, *Conjugate Point Symposium, ESSA Tech. Mem., IERTM-ITSA*, *72*, 1967.
- Brittnacher, M., M. Wilber, M. Fillingim, D. Chua, G. Parks, J. Spann, and G. Germany, Global auroral response to a solar wind pressure pulse, *Adv. Space Res.*, *25*, 1377, 2000.
- Bryant, D. A., G. M. Courtier, and A. D. Johnstone, Modulation of auroral electrons at large distances from the Earth, *J. Atmos. Terr. Phys.*, *31*, 579, 1969.
- Carlson, C. W., R. F. Pfaff, and J. G. Watzin, The Fast Auroral Snapshot Mission, *Geophys. Res. Lett.*, *25*, 2013, 1998a.
- Carlson, C. W., et al., FAST observations in the downward auroral current region: Energetic upgoing electron beams, parallel potential drops, and ion heating, *Geophys. Res. Lett.*, *25*, 2017, 1998b.
- Chaston, C. C., Accelerated electrons in the polar cap boundary, *Eos Trans. AGU*, *82*, F1078, 2001.

- Chaston, C. C., C. W. Carlson, R. E. Ergun, and J. P. McFadden, Alfvén waves, density cavities, and electron acceleration observed from the FAST spacecraft, *Physica Scripta*, T84, 64, 2000.
- Chiu, Y. T., and M. Shulz, Self-consistent particle and parallel electrostatic field distributions in the magnetospheric-ionospheric auroral region, *J. Geophys. Res.*, 83, 629, 1978.
- Chua, D., G. Parks, M. Brittnacher, W. Peria, G. Germany, J. Spann, and C. Carlson, Energy characteristics of auroral electron precipitation: A comparison of substorms and pressure pulse related auroral activity, *J. Geophys. Res.*, 106, 5945, 2001.
- Cogger, L. L., J. S. Murphree, S. Ismail, and C. D. Anger, Characteristics of dayside 5577 Å and 3914 Å aurora, *Geophys. Res. Lett.*, 4, 413, 1977.
- Coroniti, F. V., R. L. McPherron, and G. K. Parks, Studies of the magnetospheric substorms, 3, Concept of the magnetospheric substorm and its relation to electron precipitation and micropulsations, *J. Geophys. Res.*, 73, 1715, 1968.
- Cummer, S. A., et al., Global multispectral auroral imaging of an isolated substorm, *Geophys. Res. Lett.*, 27, 637, 2000.
- Cummings, W. D., J. N. Barfield, and P. J. Coleman, Magnetospheric substorms observed at the synchronous orbit, *J. Geophys. Res.*, 73, 6687, 1968.
- Dandekar, B. S., and C. P. Pike, The midday, discrete auroral gap, *J. Geophys. Res.*, 83, 4227, 1978.
- Daniell, R. E., and D. J. Strickland, Dependence of auroral middle UV emissions on the incident electron spectrum and neutral atmosphere, *J. Geophys. Res.*, 91, 321, 1986.
- Datlowe, D. W., W. L. Imhof, and H. D. Voss, Kilometer scale structures in auroral X-ray arcs detected by combining satellite X-ray images with in situ energetic electron flux profiles, *J. Geophys. Res.*, 98, 9259, 1993.

- DeForest, S. E., and C. E. McIlwain, Plasma clouds in the magnetosphere, *J. Geophys. Res.*, *76*, 3587, 1971.
- Evans, D. S., Precipitating electron fluxes formed by a magnetic field aligned potential difference, *J. Geophys. Res.*, *79*, 2853, 1974.
- Evans, D. S., and T. E. Moore, Precipitation electrons associated with the diffuse aurora: Evidence for electrons of atmospheric origin in the plasma sheet, *J. Geophys. Res.*, *84*, 6451, 1979.
- Fedder, J. A., S. P. Slinker, and J. G. Lyon, Geomagnetic substorms and magnetospheric dynamics caused by solar wind variability, *EOS Trans. AGU*, *75*, 315, 1994.
- Fox, N. J., M. Peredo, and B. J. Thompson, Cradle to grave tracking of the January 6-11, 1997 Sun-Earth connection event, *Geophys. Res. Lett.*, *25*, 2461, 1998.
- Frank, L. A., and K. L. Ackerson, Observations of charged particle precipitation into the auroral zone, *J. Geophys. Res.*, *76*, 3612, 1971.
- Frank, L. A., J. D. Craven, J. L. Burch, and J. D. Winningham, Polar views of the Earth's aurora with Dynamics Explorer, *Geophys. Res. Lett.*, *9*, 1001, 1982.
- Frank, L. A., J. B. Sigwarth, J. D. Craven, J. P. Craven, J. S. Dolan, M. R. Dvorsky, P. K. Hardebeck, J. D. Harvey, and D. W. Muller, The Visible Imaging System (VIS) for the Polar Spacecraft, *Space Sci. Rev.*, *71*, 297, 1995.
- Fritz, H., *Verzeichnis Beobachteter Polarlichter*, Akademie (Wien), 1873.
- Germany, G. A., M. R. Torr, P. G. Richards, and D. G. Torr, The dependence of modeled OI and N_2 Lyman Birge Hopfield auroral emissions on the neutral atmosphere, *J. Geophys. Res.*, *95*, 7725, 1990.
- Germany, G. A., D. G. Torr, P. G. Richards, M. R. Torr, and S. John, Determination of ionospheric conductivities from FUV auroral emissions, *J. Geophys. Res.*, *99*, 23,297, 1994a.

- Germany, G. A., M. R. Torr, D. G. Torr, and P. G. Richards, Use of FUV auroral emissions as diagnostic indicators, *J. Geophys. Res.*, *99*, 383, 1994b.
- Germany, G. A., J. F. Spann, G. K. Parks, M. J. Brittnacher, R. Elsen, L. Chen, D. Lummerzheim, and M. H. Rees, Auroral observations from the Polar Ultraviolet Imager (UVI), in *AGU Monograph, Encounter Between Global Observations and Models in the ISTP Era*, edited by J. Horwitz, D. Gallagher, and W. Peterson, p. 143, AGU, Washington, D. C., 1998.
- Hedin, A. H., MSIS-86 thermospheric model, *J. Geophys. Res.*, *92*, 4649, 1987.
- Heikkila, W. J., Photoelectron escape flux observed at midlatitudes, *J. Geophys. Res.*, *75*, 4877, 1970.
- Holzworth, R. H., and C.-I. Meng, Mathematical representation of the auroral oval, *Geophys. Res. Lett.*, *2*, 377, 1975.
- Iijima, T., and T. A. Potemra, Large-scale characteristics of field-aligned currents associated with substorms, *J. Geophys. Res.*, *83*, 599, 1978.
- Imhof, W. L., et al., The Polar Ionospheric X-ray Imaging Experiment, *Space Sci. Rev.*, *71*, 1995.
- Ishimoto, M., C.-I. Meng, G. J. Romick, and R. E. Huffman, Auroral electron energy and flux from molecular nitrogen ultraviolet emissions observed by the S3-4 satellite, *J. Geophys. Res.*, p. 9854, 1988.
- Johnstone, A. D., Pulsating Aurora, *Nature*, *274*, 119, 1978.
- Kahler, S. W., Solar flares and coronal mass ejections, *Annu. Rev. Astron. Astrophys.*, *30*, 113, 1992.
- Kamide, Y., and G. Rostoker, The spatial relationship of field-aligned currents and auroral electrojets to the distribution of nightside auroras, *J. Geophys. Res.*, *82*, 5589, 1977.

- Lepping, R. P., et al., The WIND magnetic field investigation, *Space Sci. Rev.*, 71, 207, 1995.
- Liou, K., P. T. Newell, C.-I. Meng, A. T. Y. Lui, M. Brittnacher, and G. Parks, Synoptic auroral distribution: A survey using Polar ultraviolet imagery, *J. Geophys. Res.*, 102, 27,197, 1997.
- Liou, K., P. T. Newell, C.-I. Meng, T. Sotirelis, M. Brittnacher, and G. Parks, Source region of 1500 MLT auroral bright spots: Simultaneous Polar UV-images and DMSP particle data, *J. Geophys. Res.*, 104, 24,587, 1999.
- Liou, K., P. T. Newell, and C.-I. Meng, Seasonal effects on auroral particle acceleration and precipitation, *J. Geophys. Res.*, 106, 5531, 2001.
- Lui, A. T. Y., and C. D. Anger, A uniform belt of diffuse auroral emissions seen by the ISIS-2 scanning photometer, *Planet. Spa. Sci.*, 21, 809, 1973.
- Lummerzheim, D., M. Brittnacher, D. Evans, G. A. Germany, G. K. Parks, M. H. Rees, and J. F. Spann, High time resolution study of the hemispheric energy flux carried by energetic electrons into the ionosphere during the May 19/20, 1996 auroral activity, *Geophys. Res. Lett.*, 44, 987, 1997.
- Lyatsky, W., P. T. Newell, and A. Hamza, Solar illumination as cause of the equinoctial preference for geomagnetic activity, *Geophys. Res. Lett.*, 28, 2353, 2001.
- Lysak, R. L., Feedback instability of the ionospheric resonant cavity, *J. Geophys. Res.*, 96, 1553, 1991.
- Maggs, J. E., and T. N. Davis, Measurements of the thicknesses of auroral structures, *Planet. Spa. Sci.*, 16, 205, 1968.
- McFadden, J., C. W. Carlson, M. H. Boehm, and T. J. Hallinan, Field-aligned electron flux oscillations that produce flickering aurora, *J. Geophys. Res.*, 92, 11,133, 1987.
- McIntosh, D. H., On the annual variation of magnetic disturbances, *Phil. Trans. Roy. Soc. London*, 251, 525, 1959.

- McPherron, R. L., G. K. Parks, and F. Coroniti, Relation of correlated magnetic micropulsations and electron precipitation to the auroral substorm, *Conjugate Point Symposium, ESSA Tech. Mem., IERTM-ITSA, 72*, 1967.
- Meng, C.-I., and S. Chakrabarti, Extreme ultraviolet emissions for monitoring auroras in dark and daylight hemispheres, *J. Geophys. Res.*, *90*, 4261, 1985.
- Meng, C.-I., and R. E. Huffman, Ultraviolet imaging from space of the aurora under full sunlight, *Geophys. Res. Lett.*, *11*, 315, 1984.
- Meng, C.-I., and R. Lundin, Auroral morphology of the midday oval, *J. Geophys. Res.*, *91*, 1572, 1986.
- Meng, C.-I., and B. H. Mauk, Global auroral morphology: Quadrennial report to the I.U.G.G. on U.S. contributions, *Rev. Geophys.*, p. 1028, 1991.
- Meng, C.-I., R. H. Holzworth, and S.-I. Akasofu, Auroral circle - Delineating the poleward boundary of the quiet auroral belt, *J. Geophys. Res.*, *82*, 164, 1977.
- Meng, C.-I., A. L. Snyder, and H. W. Kroehl, Observations of auroral westward traveling surges and electron precipitation, *JGR*, *83*, 575, 1978.
- Moore, T. E., et al., Ionospheric mass ejection in response to a CME, *Geophys. Res. Lett.*, *26*, 2339, 1999.
- Newell, P. T., and C.-I. Meng, Hemispherical asymmetry in cusp precipitation near solstices, *J. Geophys. Res.*, *93*, 2643, 1988.
- Newell, P. T., C.-I. Meng, and K. M. Lyons, Suppression of discrete aurorae by sunlight, *Nature*, *381*, 766, 1996.
- Newell, P. T., R. A. Greenwald, and J. M. Ruohoniemi, The role of the ionosphere in aurora and space weather, *RoG*, *39*, 137, 2001.
- Ogawa, S., and M. Ogawa, Absorption cross sections of $O_2(a^1\delta_g)$ and $O_2(X^3\sigma_g)$ in the region from 1087 to 1700 Å, *Can. J. Phys.*, *53*, 1845, 1975.

- Ostgaard, N., J. Stadsnes, J. Bjordal, R. R. Vondrak, S. A. Cummer, D. L. Chenette, G. K. Parks, M. J. Brittnacher, and D. L. McKenzie, Global-scale electron precipitation features seen in UV and X-rays during substorms, *J. Geophys. Res.*, *104*, 10,191, 1999.
- Ostgaard, N., J. Stadsnes, J. Bjordal, G. A. Germany, R. R. Vondrak, G. K. Parks, S. A. Cummer, D. L. Chenette, and J. G. Pronko, Auroral electron distributions derived from combined UV and X-ray emissions, *J. Geophys. Res.*, *106*, 26,081, 2001.
- Parks, G. K., *Physics of Space Plasmas*, first ed., Addison-Wesley, 1991.
- Parks, G. K., and J. R. Winckler, Acceleration of energetic electrons observed at the synchronous altitude during magnetospheric substorms, *J. Geophys. Res.*, *73*, 5786, 1968.
- Parks, G. K., F. V. Coroniti, R. L. McPherron, and K. A. Anderson, Characteristics of modulated energetic electron precipitation occurring during auroral substorms, *J. Geophys. Res.*, *73*, 1685, 1968.
- Petrinec, S. M., and C. T. Russell, Near-Earth magnetotail shape and size as determined from the magnetopause flaring angle, *J. Geophys. Res.*, *101*, 137, 1996.
- Petrinec, S. M., W. L. Imhof, D. L. Chenette, J. Mabilia, and T. J. Rosenberg, Day-side/nightside auroral X-ray emission differences - implications for ionospheric conductance, *Geophys. Res. Lett.*, *27*, 3277, 2000.
- Puetter, R. C., Pixon-based multiresolution image reconstruction and the quantification of picture information content, *Int. J. Image Sys. and Tech.*, *6*, 314, 1995.
- Rasmussen, C. E., R. E. Schunk, and V. B. Wickwar, A photochemical equilibrium model for ionospheric conductivity, *J. Geophys. Res.*, *93*, 9831, 1988.
- Rees, M. H., and D. Luckey, Auroral electron energy derived from ratio of spectroscopic emissions, *J. Geophys. Res.*, *79*, 5181, 1974.

- Rees, M. H., D. Lummerzheim, R. G. Roble, J. D. Winningham, J. D. Craven, and L. A. Frank, Auroral energy deposition rate, characteristic electron energy, and ionospheric parameters derived from Dynamics Explorer 1 images, *J. Geophys. Res.*, *93*, 12,841, 1988.
- Rème, H., and J. M. Bosqued, Rocket observations of electron precipitation in a westward-traveling surge, *J. Geophys. Res.*, *78*, 5553, 1973.
- Richards, P. G., and D. G. Torr, Auroral modeling of the 3371 Å emission rate: Dependence on characteristic electron energy, *J. Geophys. Res.*, *95*, 10,337, 1990.
- Richmond, A. D., Ionospheric electrodynamics using magnetic apex coordinates, *J. Geomag. Geoelectr.*, *47*, 191, 1995.
- Richmond, A. D., et al., Global measures of ionospheric electrodynamic activity inferred from combined incoherent scatter radar and ground magnetometer observations, *J. Geophys. Res.*, *95*, 1061, 1990.
- Robinson, R. M., R. R. Vondrak, K. Miller, T. Dabbs, and D. Hardy, On calculating ionospheric conductances from the flux and energy of precipitating electrons, *J. Geophys. Res.*, *92*, 2565, 1987.
- Royrvik, O., and T. Davis, Pulsating aurora: local and global morphology, *J. Geophys. Res.*, *82*, 4270, 1977.
- Russell, C. T., and R. L. McPherron, Semiannual variation of geomagnetic activity, *J. Geophys. Res.*, *78*, 98, 1973.
- Russell, C. T., X. W. Zhou, P. J. Chi, H. Kawano, T. E. Moore, W. K. Peterson, J. B. Cladis, and H. J. Singer, Sudden compression of the outer magnetosphere associated with an ionospheric mass ejection, *Geophys. Res. Lett.*, *26*, 2343, 1999.
- Schulz, M., Direct influence of ring current on auroral-oval diameter, *J. Geophys. Res.*, *102*, 14,149, 1997.

- Shephard, G. G., J. H. Whitteker, J. D. Winningham, J. H. Hoffman, E. J. Maier, L. H. Brace, J. R. Burrows, and L. L. Cogger, The topside magnetospheric cleft ionosphere observed from the ISIS-2 spacecraft, *J. Geophys. Res.*, *81*, 6092, 1976.
- Shue, J.-H., P. T. Newell, K. Liou, and C.-I. Meng, The quantitative relationship between auroral brightness and solar EUV Pedersen conductance, *J. Geophys. Res.*, *106*, 5883, 2001.
- Spann, J. F., M. Brittnacher, R. Elsen, G. K. Parks, and G. A. Germany, Initial response and complex polar cap structures of the aurora in response to the January 10, 1997 magnetic cloud, *Geophys. Res. Lett.*, *25*, 2577, 1998.
- Stadsnes, J., K. Aarsnes, and J. Bjordal, X-ray imaging of the aurora, *Adv. Space Res.*, *20*, 1043, 1997.
- Steele, D. P., D. J. McEwen, and J. S. Murphree, On the possibility of auroral remote sensing with the Viking Ultraviolet Imager, *J. Geophys. Res.*, *97*, 2845, 1992.
- Stenbaek-Nielsen, H. C., and A. Otto, Conjugate auroras and the interplanetary magnetic field, *J. Geophys. Res.*, *102*, 2223, 1997.
- Stenbaek-Nielsen, H. C., T. Hallinan, D. Osborne, J. Kimball, C. Chaston, J. McFadden, G. Delory, M. Temerin, and C. Carlson, Aircraft observations conjugate to FAST: Auroral arc thicknesses, *Geophys. Res. Lett.*, *25*, 2073, 1998.
- Störmer, C., *The Polar Aurora*, Clarendon Press, Oxford, 1955.
- Strickland, D. J., J. R. Jasperse, and J. A. Whalen, Dependence of auroral FUV emissions on the incident electron spectrum and neutral atmosphere, *J. Geophys. Res.*, *88*, 8051, 1983.
- Strickland, D. J., R. R. Meier, J. H. Hecht, and A. B. Christensen, Deducing composition and incident electron spectra from ground-based auroral optical measurements: Theory and model results, *J. Geophys. Res.*, *94*, 13,527, 1989.

- Strickland, D. J., T. Majeed, A. B. Christensen, and J. H. Hecht, Remote sensing of atomic oxygen in auroral rocket experiments using topside zenith viewing O/N₂ brightness ratios, *J. Geophys. Res.*, *102*, 2475, 1997.
- Strickland, D. J., R. J. Cox, R. R. Meier, and D. P. Drob, Global O/N₂ derived from DE-1 FUV imaging dayglow data: technique and examples from two storm periods, *J. Geophys. Res.*, *104*, 4251, 1999.
- Summers, D., and R. M. Thorne, The modified plasma dispersion function, *Phys. Fluids B*, *8*(3), 1835, 1991.
- Tanskanen, P. J., The pulsating aurora and its relationship to fields and charged-particle precipitation, in *Auroral Physics*, edited by C.-I. Meng, M. J. Rycroft, and L. A. Frank, p. 351, Cambridge University Press, 1991.
- Taylor, J. R., *An Introduction to Error Analysis, The Study of Uncertainties in Physical Measurements*, University Science Books, 1982.
- Torr, M. R., et al., A far ultraviolet imager for the International Solar-Terrestrial Physics Mission, *Space Sci. Rev.*, *71*, 329, 1995.
- Vestine, E. H., The geographical incidence of aurora and magnetic disturbance, northern hemisphere, *Terr. Mag. Atmos. Electr.*, *49*, 77, 1944.
- Walker, R. J., T. Ogino, and M. Ashour-Abdalla, Using global magnetohydrodynamic simulation to model auroral dynamics, 1993.
- Winglee, R. M., D. Chua, M. Brittnacher, and G. K. Parks, Ionospheric outflows during the Sept. 24-25, 1998 magnetic cloud event, 2000.
- Yokoyama, N., Y. Kamide, and H. Miyaoka, The size of the auroral belt during magnetic storms, *Ann. Geophys.*, *16*, 566, 1998.
- Zandt, T. E. V., W. L. Clark, and J. M. Warnock, Magnetic apex coordinates: A magnetic coordinate system for the ionospheric F2 layer, *J. Geophys. Res.*, *77*, 2406, 1972.

Zhou, X., and B. T. Tsurutani, Rapid intensification and propagation of the dayside aurora: Large scale interplanetary pressure pulses (fast shocks), *Geophys. Res. Lett.*, *26*, 1097, 1999.

Zukic, M., D. G. Torr, J. Kim, J. F. Spann, and M. R. Torr, Filters for the International Solar Terrestrial Physics Mission far-ultraviolet imager, *Optical Engineering*, *32*, 3069, 1993.

Appendix A

DATA PROCESSING TECHNIQUES FOR THE QUANTITATIVE ANALYSIS OF UVI IMAGES

Before computing the energy flux and average energy from the UVI images a number of calibrations and corrections to the raw UVI images are necessary. In this Appendix we describe the details of these data processing steps. These include line of sight (van Rhijn effect) and dayglow corrections. Moreover, we discuss in the uncertainties in the data introduced by imperfections in the Polar spacecraft motion and how these are dealt with in the data processing.

A.1 Line of Sight Correction

The viewing geometry of the UVI camera changes drastically at different points along Polar's orbit when observing the aurora. Unless Polar is near apogee with nadir viewing of the aurora, the UVI line of sight (LOS) is a slant path through an extended object. If we include only geometric factors, the intensity of the off-nadir pixels must be multiplied by a factor of $\cos(\theta_{i,j})$ where $\theta_{i,j}$ is the look angle for a given pixel(i,j). $\theta_{i,j}$ can be defined as the angle between the local zenith direction and the vector pointing from that location to each pixel(i,j). This is to compensate for the increased optical path length when viewing the column-integrated emissions from an off-nadir perspective.

Germany et al. [1998] has shown, however, that there are filter dependent effects which are important for the line of sight correction. For increasing look angles, the LBH emissions must traverse increasingly longer ray paths through O₂ in the upper atmosphere and thus suffer a greater degree of extinction. Figure A.1 (From *Germany et al.* [1998]) shows the line of sight enhancement factor as a function of look angle for the LBHl and LBHs filters. The LOS enhancement from purely geometric factors

is given by the cosine curve shown by the solid line. The apparent LOS enhancement increases for increasing look angle because the length of the optical path increases through a given emission layer as one views farther away from nadir. For the emission observed in the LBHI filter a minor degree of O₂ absorption in the short wavelength portion of the LBHI bandpass produces a slight departure from the geometric factor above as shown in Figure A.1. An empirical fit to the LBHI line of sight enhancement (LOS_{LBHI}) gives

$$LOS_{LBHI} = \frac{e^{0.061(1 - \frac{1}{\cos \theta_{i,j}})}}{\cos \theta_{i,j}} \quad (\text{A.1})$$

where $\theta_{i,j}$ is the look angle for pixel(i,j). For the emissions in the LBHs bandpass, the LOS correction is subject to two competing factors: (1) decreasing throughput from more O₂ absorption as the look angle increases and (2) increase in apparent brightness from changes in the viewing geometry as described above. From Figure A.1 one sees that these two factors approximately negate one another. For look angles less than about 50° the empirical LOS enhancement curve for the LBHs response is near unity. Thus, no LOS correction is applied to pixels in the LBHs images for look angles less than 50°. Quantitative analysis of LBHs images where look angles exceed 50° is not performed because the LOS correction is not well characterized for such oblique viewing geometries.

A.2 Dayglow Correction

In general, the images taken by UVI have contributions from both auroral and thermospheric airglow sources. Airglow observed by UVI is created by thermospheric photoelectrons produced by solar EUV radiation as well as resonantly scattered solar UV photons¹. The FUV airglow emissions observed by UVI are thus a function of solar EUV flux, solar zenith angle², and the UVI look direction. Because the FUV airglow emissions observed by UVI originate from the primary constituents of thermosphere,

¹A solar UV photon can be resonantly scattered if its frequency is near an energy level transition frequency of a molecular or atomic constituent of the upper atmosphere

²The solar zenith angle is defined as the angle between the local zenith direction for a given point on the Earth and the line between that point and the sun

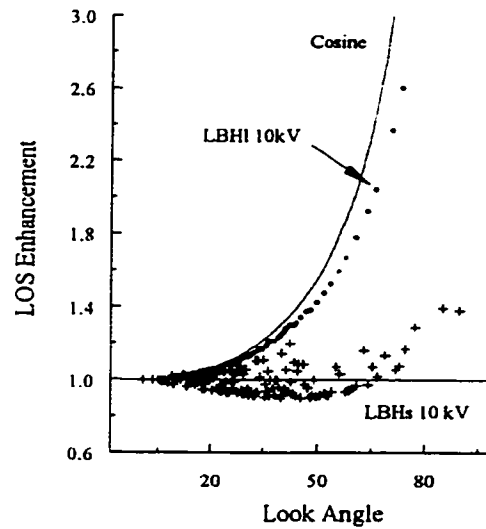


Figure A.1: Filter dependent line of sight enhancements (From *Germany et al.* [1998])

in principle, the Polar UVI dayglow observations are ideal for doing studies of thermospheric variability as a function of solar EUV inputs over long time scales (such as over a solar cycle). *Strickland et al.* [1997, 1999] has demonstrated a technique for inferring thermospheric compositional variations from FUV airglow observations.

For auroral studies the airglow is treated as a contaminant and is removed by a technique similar to that described by *Lummerzheim et al.* [1997]. Here it is assumed that pixels at the same solar zenith angle will record similar airglow intensities. Thus, pixels in the dayside portion of an image affected by airglow are binned according to solar zenith angle, excluding the auroral contribution. An example is shown in Figure A.2 for dayglow observations on June 1, 1999. The binned airglow flux as a function of solar zenith angle is then modeled using least-squares fit to a cosine squared function of the form

$$I_{dayglow} = I_0 \cos^2(I_1 \Phi_{sza}) \quad (\text{A.2})$$

where ϕ_{sza} is the solar zenith angle. I_0 and I_1 are the two parameters returned by the

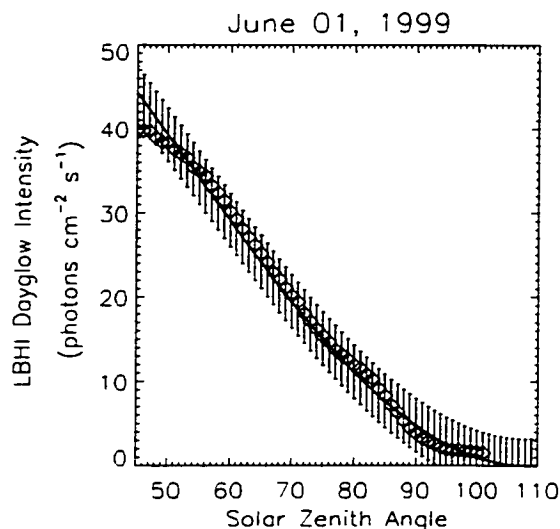


Figure A.2: Observed dayglow flux as a function of solar zenith angle (diamonds) on June 1, 1999. The least-squares fit using a cosine-squared model is shown by the solid line with the $1-\sigma$ uncertainties of the fit parameters shown by the error bars.

least-squares fitting algorithm (along with the $1-\sigma$ uncertainties of each fit parameter). I_0 is the dayglow intensity at zero solar zenith angle and I_1 is a dimensionless factor that governs how fast the dayglow intensity falls off for increasing solar zenith angles. The cosine squared model is truncated for Φ_{sza} greater than 100° since the dayglow flux is negligible at these large solar zenith angles. The functional form used to fit the observed dayglow was determined empirically. The solid line in Figure A.2 shows the least-squares, modeled fit to the binned dayglow intensities with the error bars showing the $1-\sigma$ uncertainties in the dayglow model at each solar zenith angle.

The least-squares fit dayglow model (dayglow intensity versus solar zenith angle) is then projected into a two-dimensional image to match the viewing geometry of solar zenith angles for a given UVI image. This modeled surface is then subtracted from the uncorrected image to remove the dayglow contributions. This is demonstrated in Figure A.3. The left image shows an uncorrected UVI image with both auroral and airglow contributions, the middle image is the modeled dayglow surface, and the right

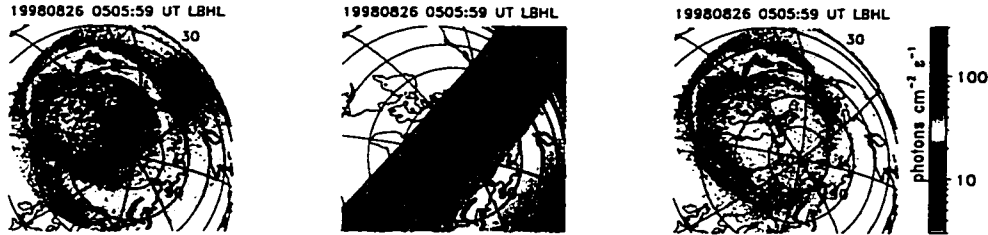


Figure A.3: **Left:** UVI image with both auroral and airglow contributions. **Middle:** Modeled dayglow surface assuming that the dayglow intensity is constant at a given solar zenith angle. **Right:** UVI image with dayglow subtracted.

image shows the UVI image with the dayglow subtracted. The remaining flux in the sunlit portion of the images following the removal of the nominal dayglow emissions is attributed to dayside aurora as can be seen in the right panel of Figure A.3.

A.3 UVI image binning

Before computing the LBHI:LBHs ratio each pixel in the LBHI and LBHs images is mapped into 0.5° MLAT \times 0.5 MLT hour bins over all local times and magnetic latitudes between 50 - 90° using Apex magnetic coordinates [Zandt *et al.*, 1972; Richmond, 1995]. The right panel of Figure A.4 shows an example of an image binned in this manner. In each bin we compute the average photon flux ($\text{photons cm}^{-2} \text{s}^{-1}$) observed through the LBH filters in addition to the incident energy flux inferred from the LBHI images. This binning is used to overcome not having a one-to-one spatial correspondence between the pixels in the LBHI and LBHs images which are acquired at different times. Because of spacecraft motion, the geographic coordinates of pixel(i, j) at time t_1 are not necessarily the same at time t_2 . This spatial binning also averages over the image smearing due to the spacecraft wobble. UVI images in geographic projections are also mapped into Apex magnetic coordinates on a per-pixel basis. The three projections of the UVI images used in this study (geographic, Apex Magnetic, and binned

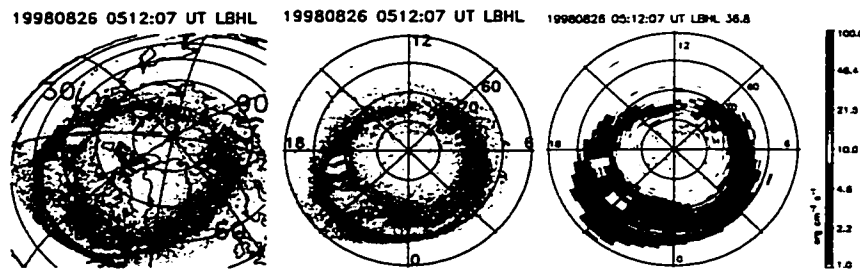


Figure A.4: UVI image mappings: geographic projection (**Right**), Apex magnetic coordinates (**Middle**), and binned Apex magnetic coordinates (**Left**).

Apex Magnetic) are shown in Figure A.4.

The UVI images used in this study are obtained in the following sequence: LBHI 18.4 second integration, LBHI 36.8 second integration, LBHs 18.4 second integration, LBHs 36.8 second integration. In this mode, the time resolution between images taken with the same filter and integration period is three minutes. To improve the signal to noise ratio for computing the average energies, the separate 18.4 and 36.8 second frames for each filter are summed to form LBHI and LBHs images with effective integration periods of 55.2 seconds. However, the separate 18.4 and 36.8 second frames cannot simply be added in series because the instrument calibration factors are all based on 36.8 second integrations. The proper image summation is given by

$$Image_{55.2} = [(Image_{18.4} - Image_{back}) + (Image_{36.8} - Image_{back})] \times \frac{2}{3} \times C$$

where C encompasses the instrument calibration factors and the factor of $\frac{2}{3}$ comes from the fact that the UVI calibration is based on 36.8 integration periods. $Image_{back}$ denotes background images obtained with the camera shutter closed and represent counts in the CCD detector due to thermal noise and other non-photonic sources.

Rapid increases in incident energy flux will produce high counts in the LBHI images while the preceding LBHs images with which the LBHI:LBHs ratio might be computed may not reflect this increase in activity. This scenario is prevalent during auroral intensifications and can result in an over-estimate of the precipitating electron mean energy. To minimize this effect on the E_{ave} computation, interpolated values of LBHI

(LBHs) photon flux are computed for the time intervals in which LBHs (LBHI) data are taken. Measured and interpolated intensities are combined to form a time series of LBHI and LBHs photon fluxes in each MLT-MLAT bin from which the LBHI:LBHs ratios and mean energies are computed. Thus, E_{ave} values are computed at a time resolution of 1.5 minutes. Average energy values in MLAT-MLT bins where the photon flux in either the LBHI or LBHs filter is less than $4 \text{ photons cm}^{-2} \text{ s}^{-1}$ are rejected. This flux threshold represents the value above which the counts in the UVI detector become statistically significant above the background noise in the detector.

Appendix B

**RELATION BETWEEN AE AND UVI DERIVED HEMISPHERIC
POWER**

For completeness it is instructive to relate the hemispheric power derived from UVI observations to previously established metrics of substorm phase. *Richmond et al.* [1990] have compared a number of parameters for measuring global ionospheric activity including the AE index and hemispheric power. *Richmond et al.* [1990] estimated the hemispheric power from particle measurements obtained by the NOAA 6 and NOAA 7 spacecraft. In this case, the hemispheric power is computed by extrapolating energy flux measurements along a single spacecraft trajectory over a statistical auroral oval that is parameterized by (some index of magnetospheric activity). Over a two day period (January 18-19, 1984) *Richmond et al.* [1990] found that the hemispheric power and AE index are well correlated (correlation coefficient of 0.81). They applied a regression fit to the data with a linear relation between HP and AE given by Equation B.1.

$$HP = 0.068AE + 9.4 \quad (\text{B.1})$$

We test the linear relation between the AE index and hemispheric power by comparing these two parameters for data spanning the years 1997-2000 (Figure B.1). The analysis is extended by comparing these two parameters under a variety of conditions in the magnetosphere-ionosphere system. *Liou et al.* [2001], *Newell et al.* [2001], and others have demonstrated statistically that ionospheric conductivity plays an important role in governing the electrodynamic coupling between the magnetosphere and ionosphere. The intensity of the aurora and the associated ionospheric currents have a documented seasonal dependence, with auroral and geomagnetic activity peaking

Table B.1: Linear fits and correlation coefficients between AE and UVI derived hemispheric power for four different conditions in the auroral ionosphere: non-storm winter, non-storm summer, storm-time winter, and storm-time summer.

| | Linear Fit | Correlation |
|-------------------|--|-------------|
| All Events | $HP = (0.119 \pm 0.001) AE + (18.378 \pm 0.377)$ | 0.748 |
| Non-storm winter | $HP = (0.1185 \pm 0.0016) AE + (17.0410 \pm 0.2870)$ | 0.801 |
| Non-storm summer | $HP = (0.1089 \pm 0.0017) AE + (16.6713 \pm 0.3996)$ | 0.750 |
| Storm-time winter | $HP = (0.1585 \pm 2.2836) AE + (30.8121 \pm 2.2836)$ | 0.707 |
| Storm-time summer | $HP = (0.0980 \pm 1.7863) AE + (25.9530 \pm 1.7863)$ | 0.671 |

when the nightside ionospheres of both hemispheres are in darkness (equinox) [Lyatsky *et al.*, 2001]. A comparison of the UVI derived hemispheric power and the AE index is thus performed as a function of both season and geomagnetic activity. Moreover, global imaging of the aurora by UVI allows us to explicitly separate the contributions to the hemispheric power from the dayside and nightside regions of the aurora. The separation of dayside and nightside contributions to the hemispheric power was previously difficult to compute because the data from which it was derived was obtained along a single satellite track and extrapolated to a statistical model auroral oval.

Scatter plots of the UVI derived hemispheric power versus the AE index are shown in Figure B.1. Figure B.1A includes all events. The four panels in Figure B.1B separate the UVI derived hemispheric power versus AE for the following conditions: Dark ionosphere during non-storm intervals, sunlit ionosphere during non-storm times, dark ionosphere during magnetic storm periods, and sunlit ionosphere during storms. The black data points correspond to the hemispheric power integrated over the entire auroral oval. Blue data points show the nightside (1800-0600 MLT) contributions to the hemispheric power versus AE index. The dayside (0600-1200 MLT) contributions to the hemispheric power are shown by the red data points. The linear relation between the AE index and hemispheric power given by *Richmond et al.* [1990] (Equation B.1) is shown by the dashed line in each panel.

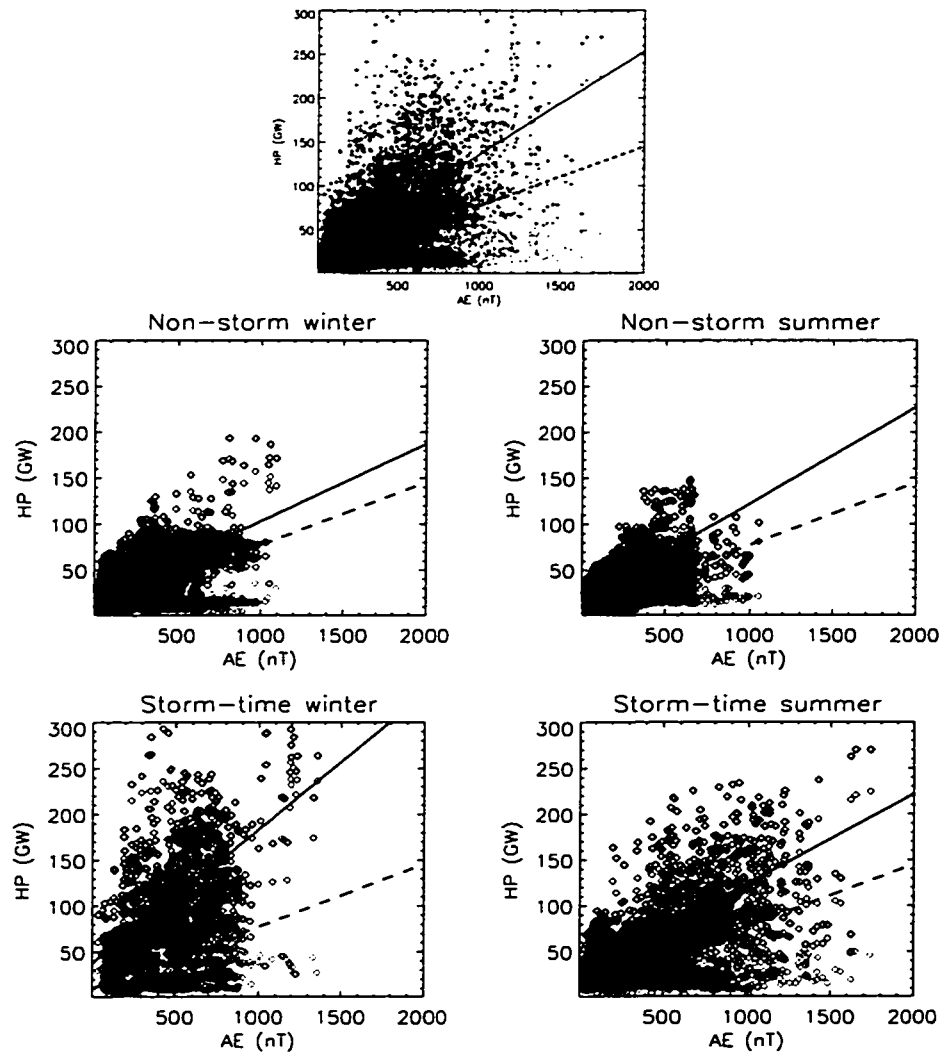


Figure B.1: Hemispheric Power (HP) versus AE index for all events (Top) and for varying conditions in the auroral ionosphere: non-storm time winter conditions (Middle Left), non-storm time summer conditions (Middle Right), storm-time winter (Bottom Left), and storm-time summer (Bottom Right). The UVI hemispheric power is separated into nightside contributions (1800-0600 MLT) shown in blue and dayside contributions (0600-1800 MLT) shown in red. The hemispheric power integrated over the entire oval is shown by the black data points. The dashed line in each panel shows the linear relation between AE and HP given by *Richmond et al.* [1990]. The solid line in each panel is the best-fit linear relation between the UVI derived HP and the AE index.

The linear fits shown by the solid lines in Figure B.1 relating the AE index to the UVI derived hemispheric power are given in Table B.1. The correlation coefficients between the AE index and the total hemispheric power are also shown for each case.

Appendix C

ANCILLARY DATA

The data contained in this appendix are shown to supplement those found in Chapter 4. The following figures are mainly sequences of Polar UVI images that show the position of the FAST spacecraft relative to the auroral oval (Figures C.1-C.9 and C.11-C.18). In these figures, the position of FAST in each UVI image frame is indicated by a set of arrows. The trailing arrow shows the position of FAST at the beginning of the image integration time. The leading arrow indicates the location of FAST at the end of the image integration.

Figure C.10 shows more examples of FAST electron measurements in the midnight sector auroral oval during substorm expansions that occur when the ionosphere is sunlit (summer). As before, the top three panels in each set of data show the downgoing, trapped, and upgoing electron energy-time spectra. The bottom three panels show the pitch angle-time spectra in the 10-100 eV, 100-1000 eV, and > 1 keV energy ranges. The spectra are in units of $\text{eV}/(\text{cm}^2 - \text{s} - \text{sr} - \text{eV})$.

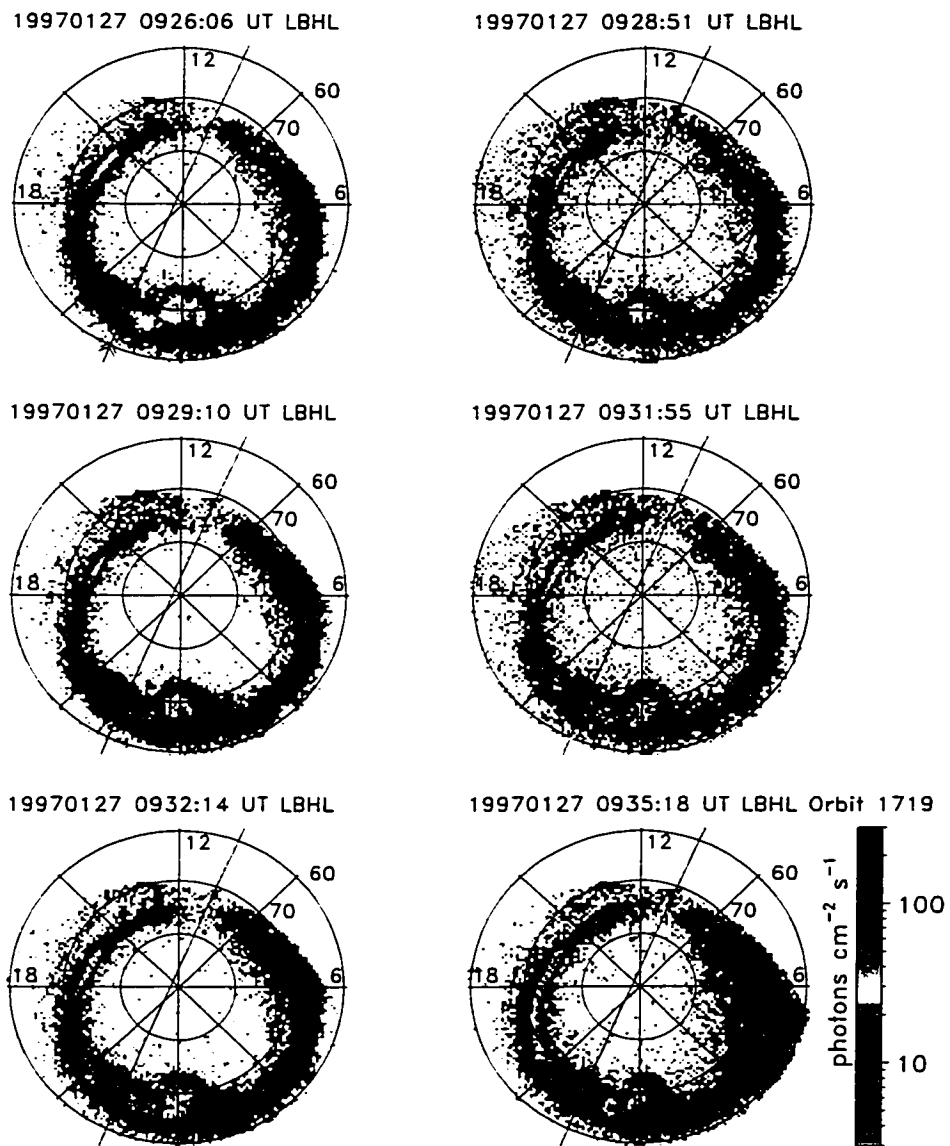


Figure C.1: UVI images corresponding to FAST orbit 1719, prior to the onset of a substorm.

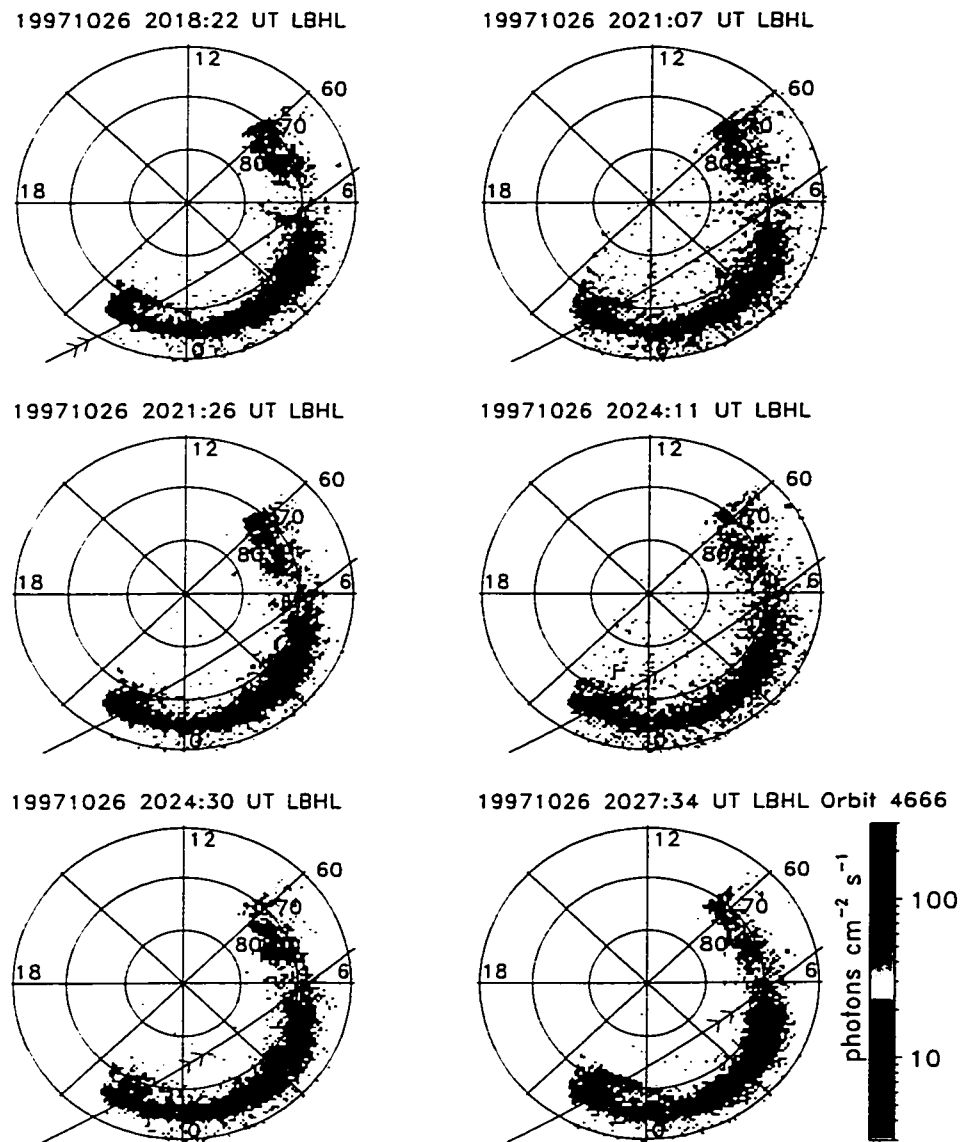


Figure C.2: UVI images corresponding to FAST orbit 4666, prior to the onset of a substorm.

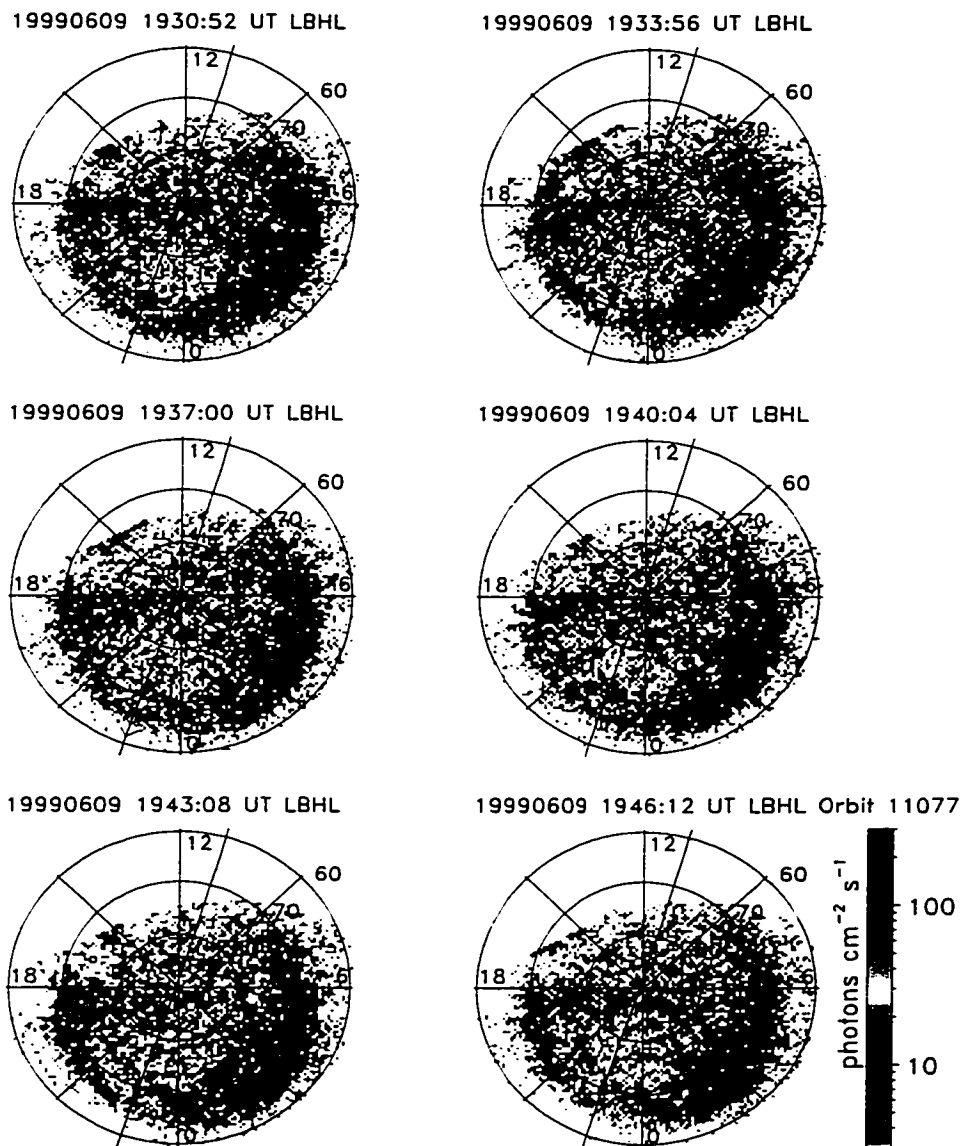


Figure C.3: UVI images corresponding to FAST orbit 11077, prior to the onset of a substorm.

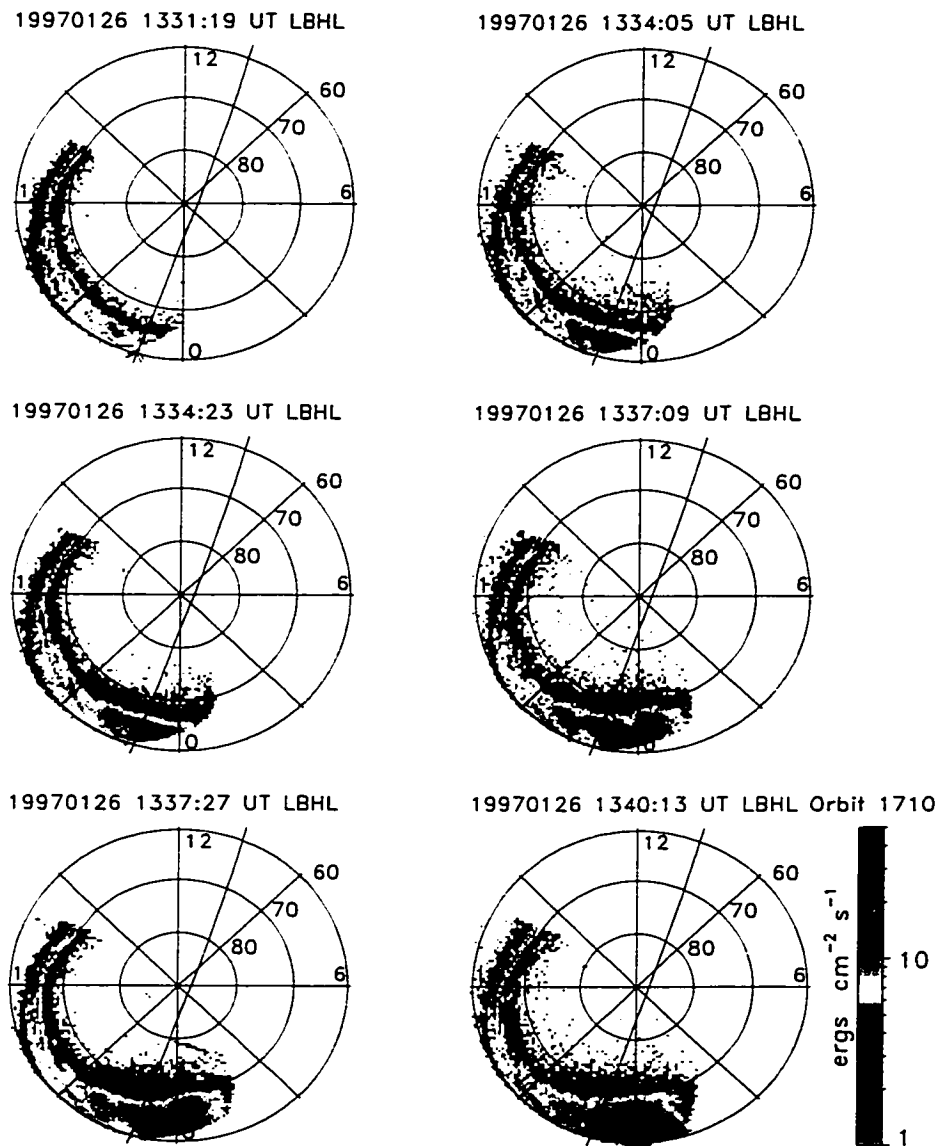


Figure C.4: UVI images corresponding to FAST orbit 1710 during substorm onset.

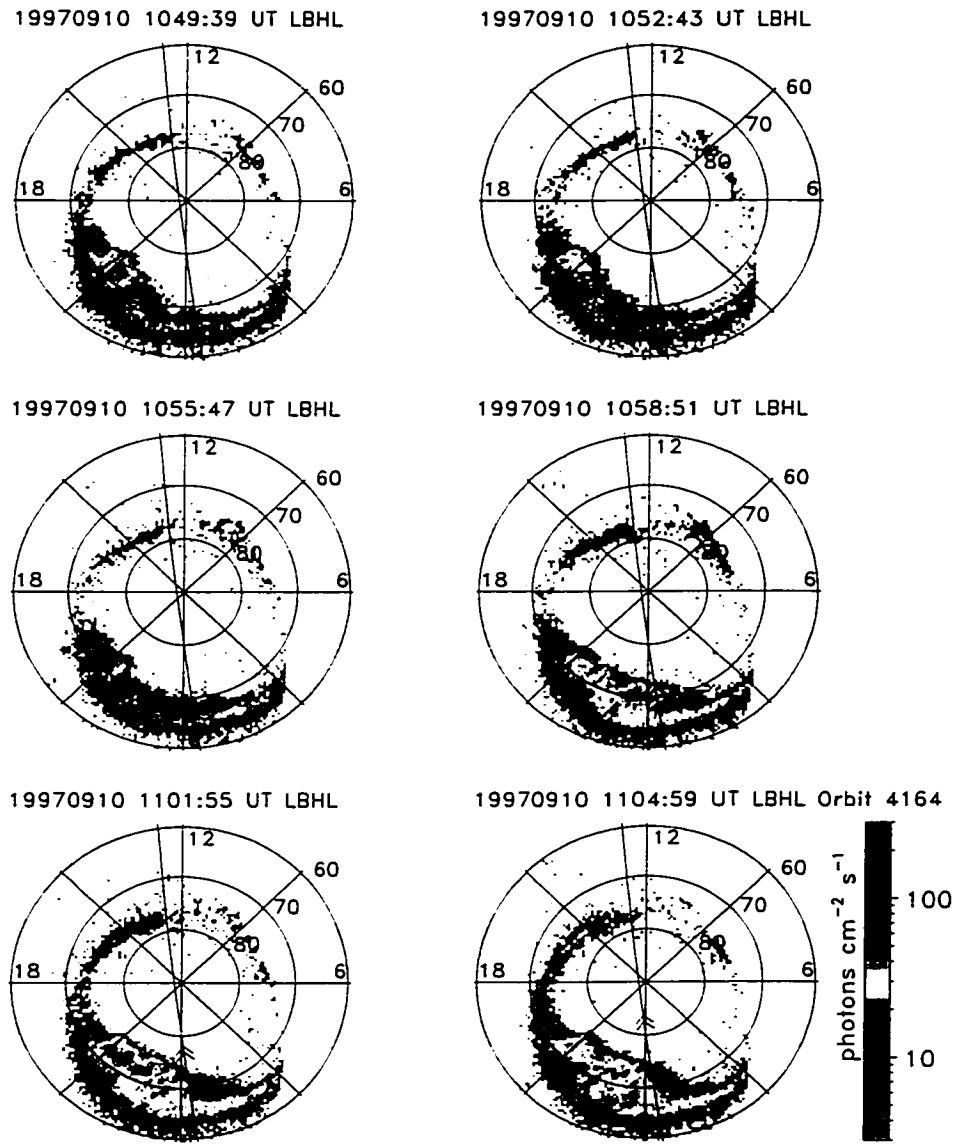


Figure C.5: UVI images corresponding to FAST orbit 4164 during substorm onset.

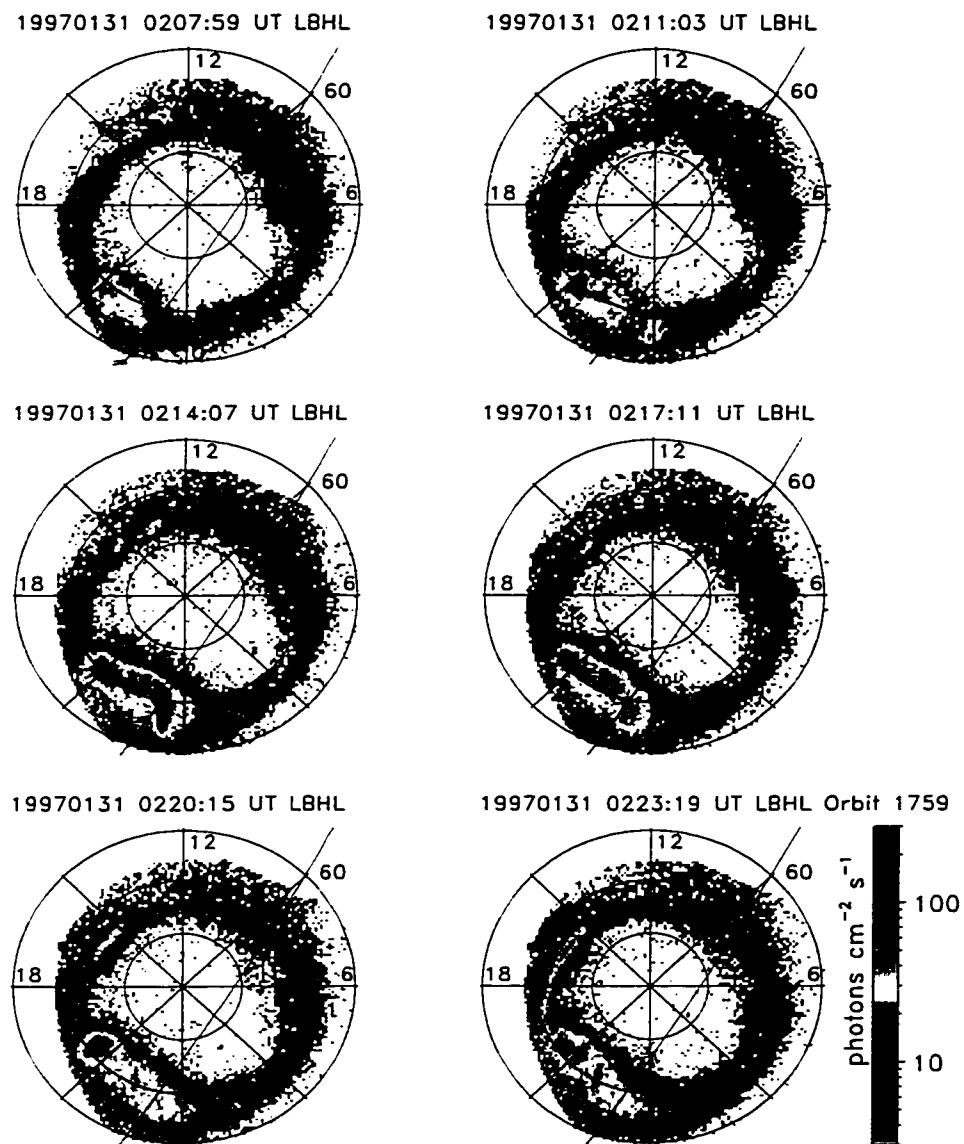


Figure C.6: UVI images corresponding to FAST orbit 1759 during substorm expansion.

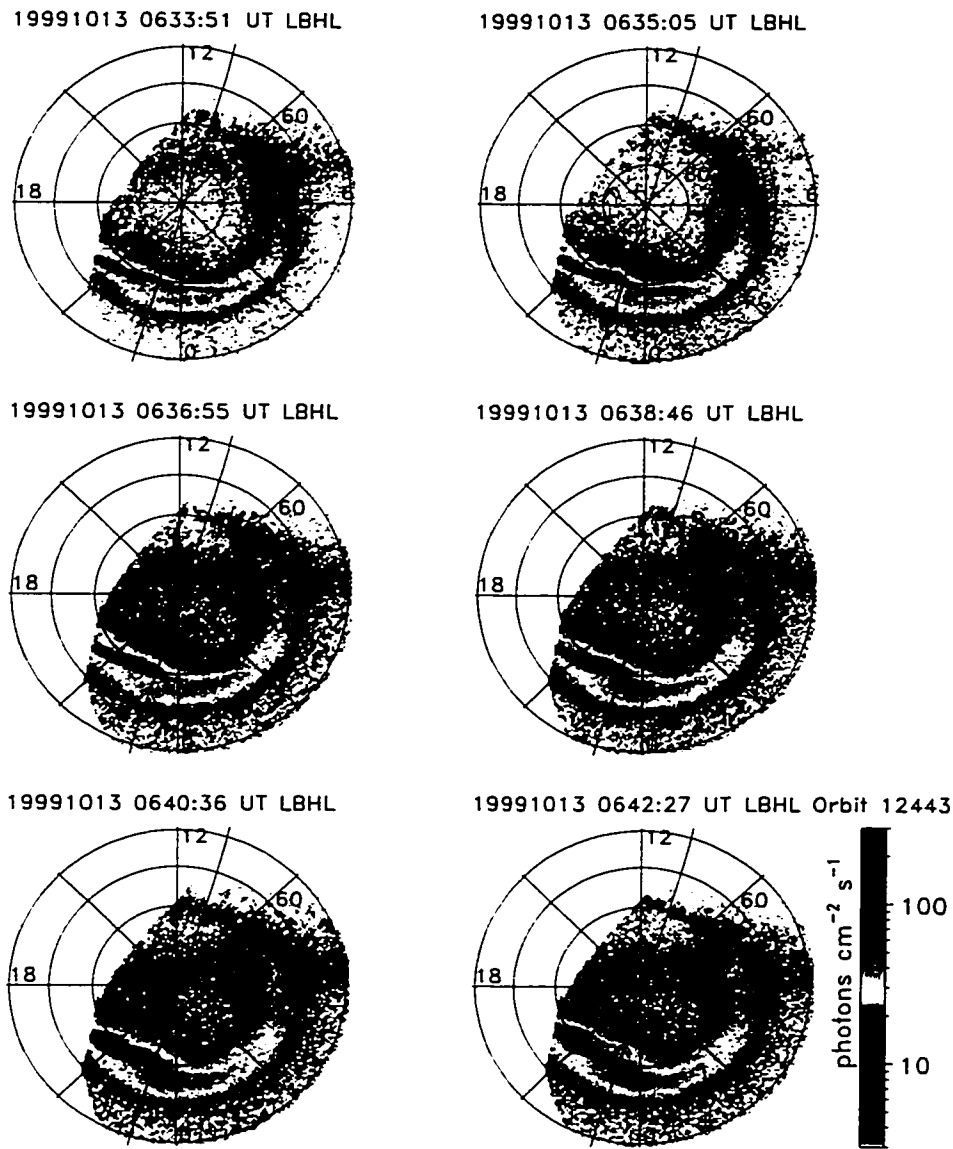


Figure C.7: UVI images corresponding to FAST orbit 12443 during substorm expansion.

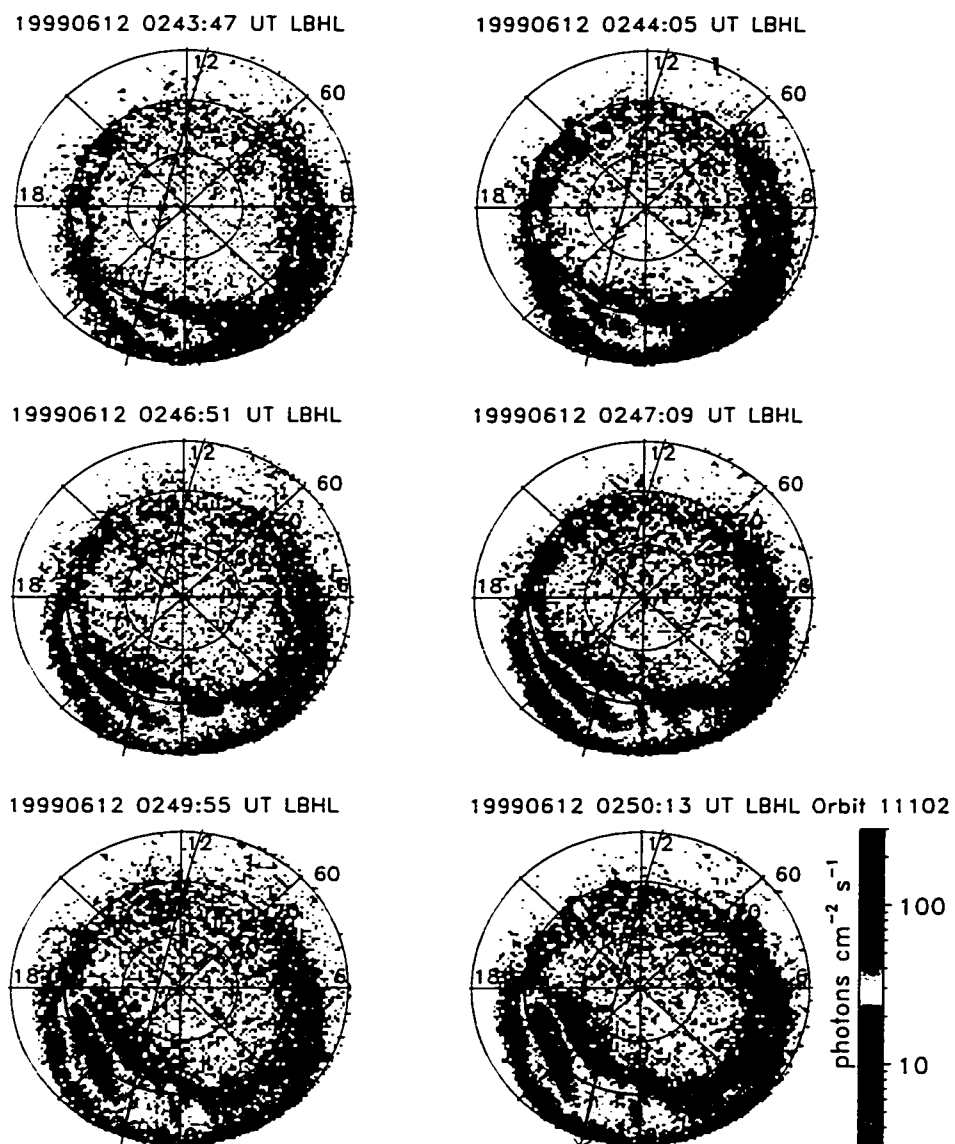


Figure C.8: UVI images corresponding to FAST orbit 11102 during substorm expansion.

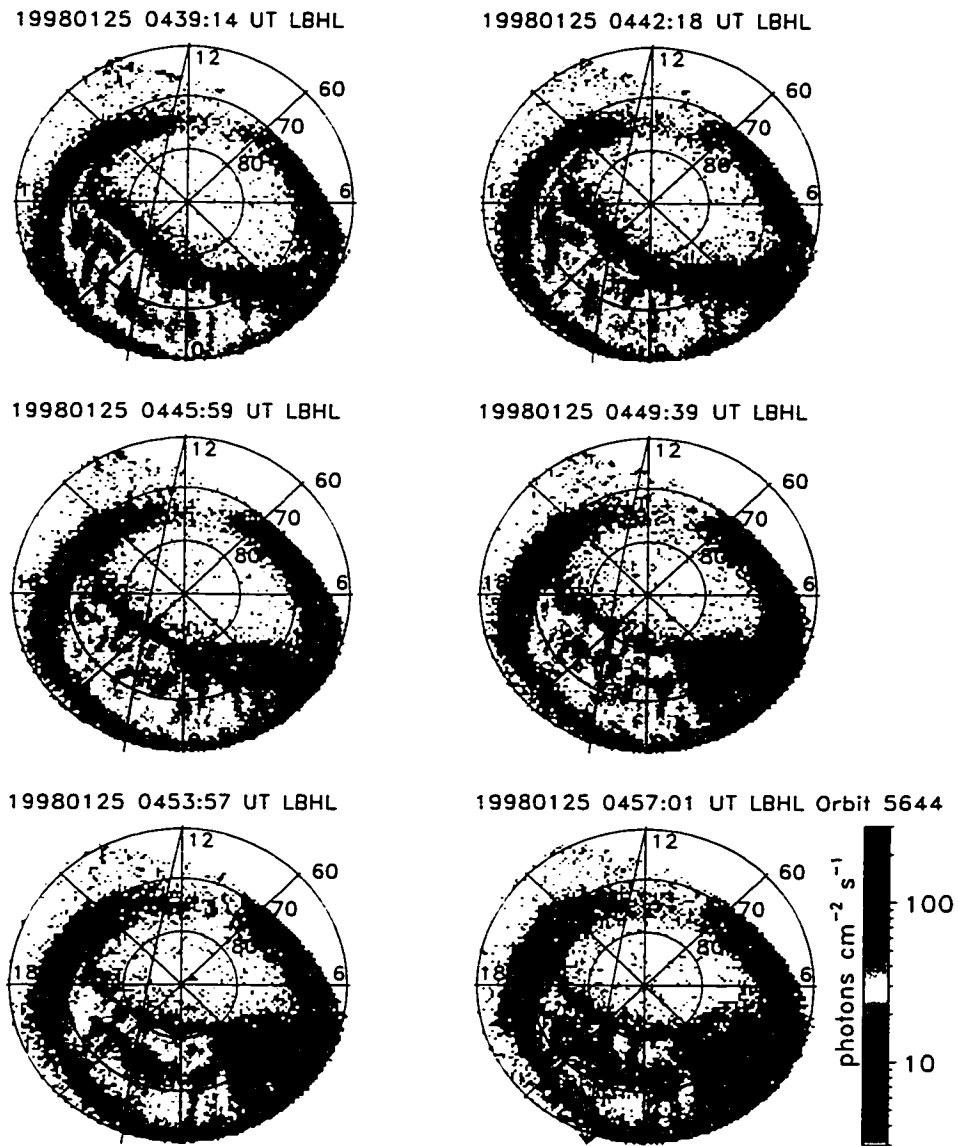


Figure C.9: UVI images corresponding to FAST orbit 5644.

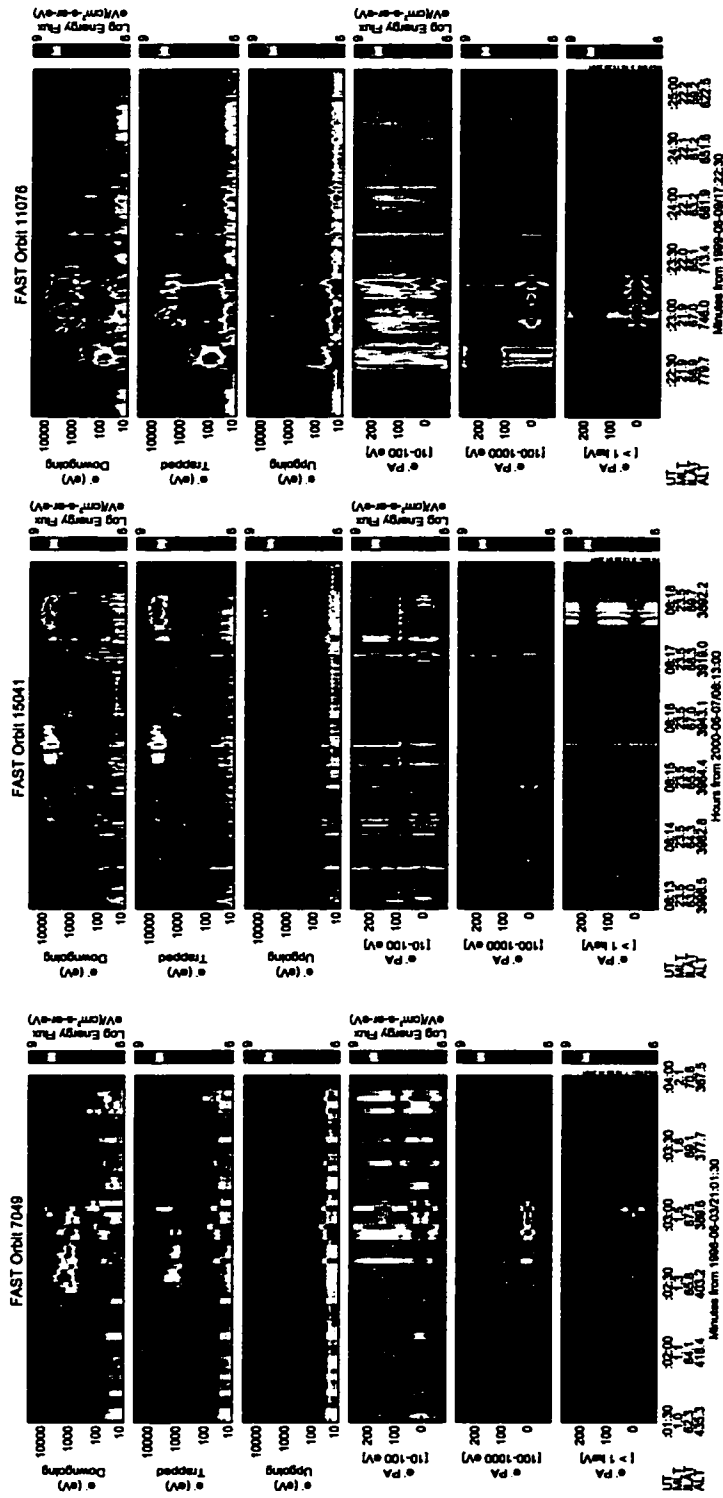


Figure C.10: More examples of summer-time FAST electron measurements during substorm expansion in the midnight sector.

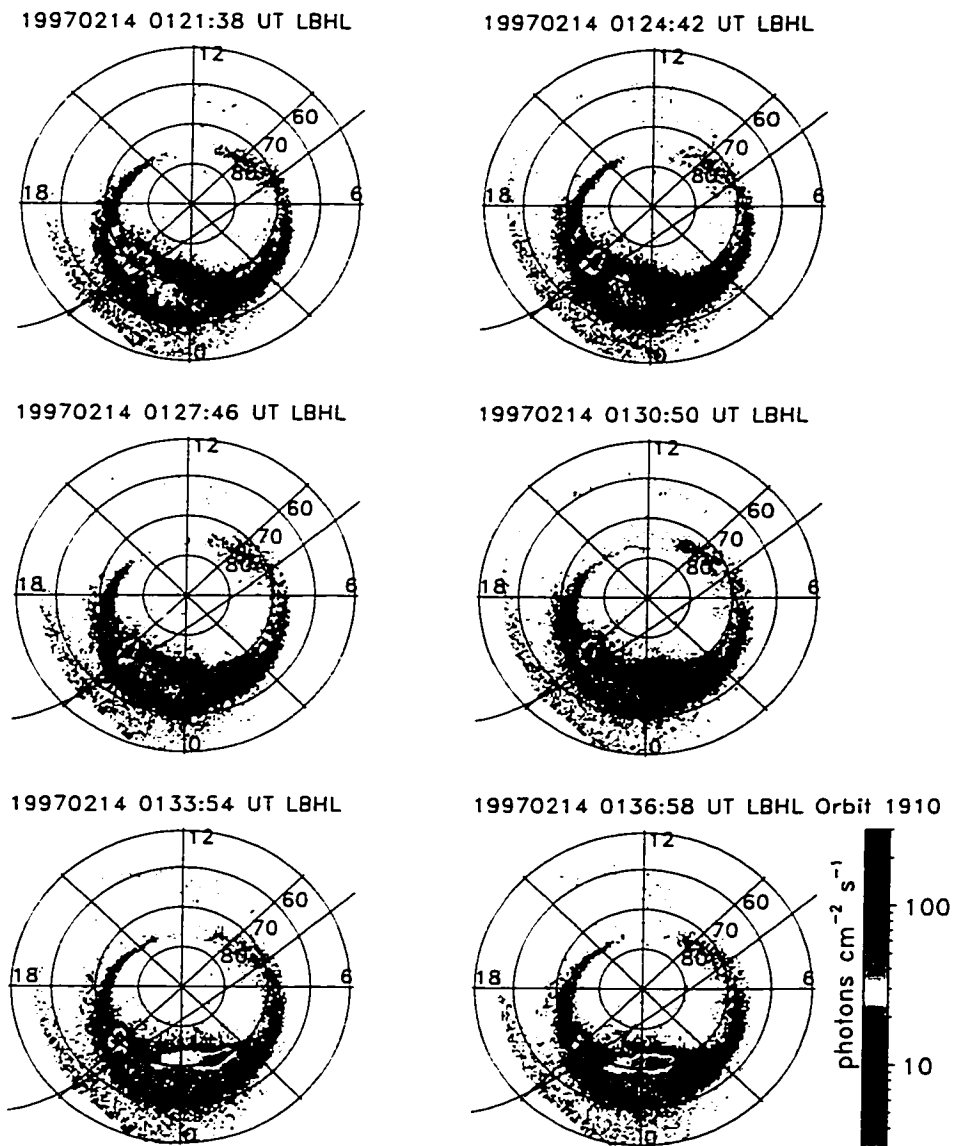


Figure C.11: UVI images corresponding to FAST orbit 1910.

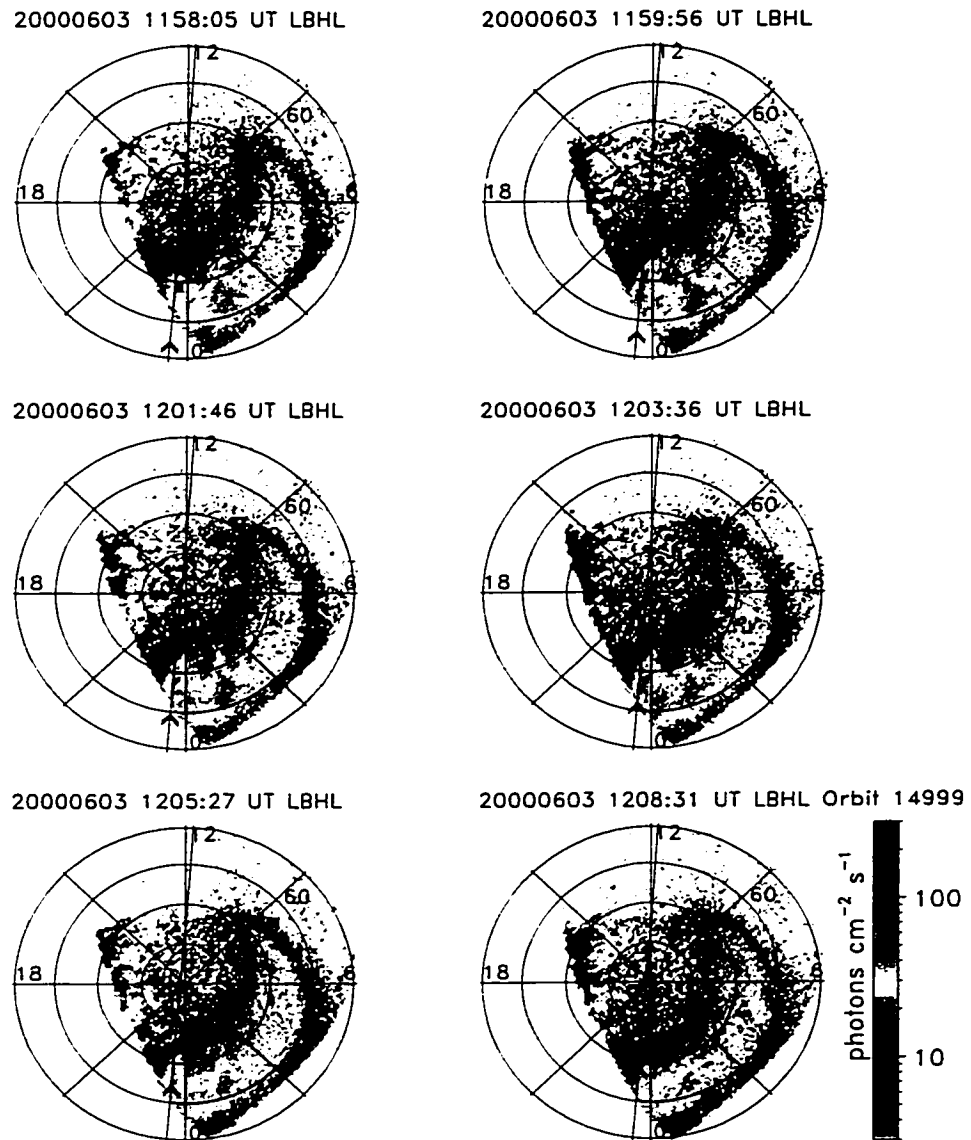


Figure C.12: UVI images corresponding to FAST orbit 14999.

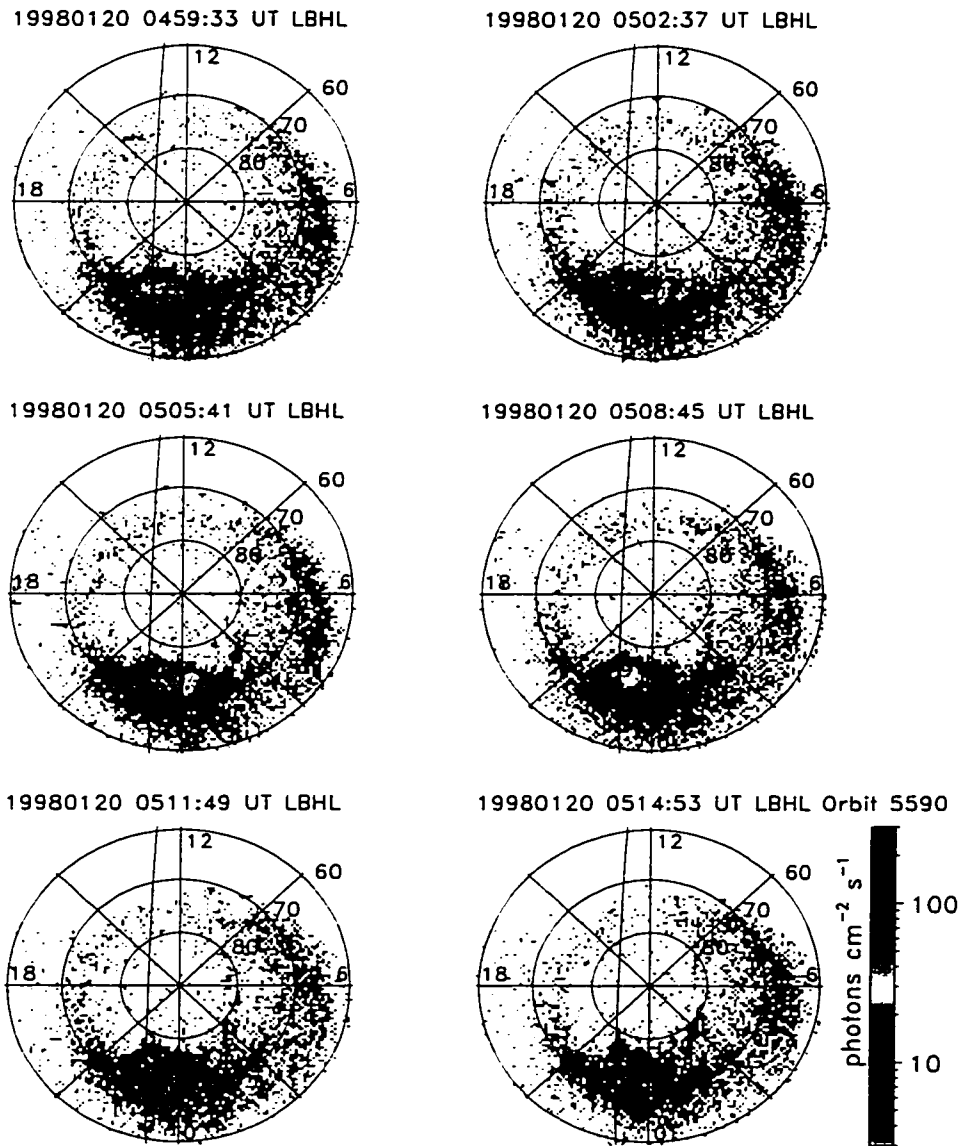


Figure C.13: UVI images corresponding to FAST orbit 5590.

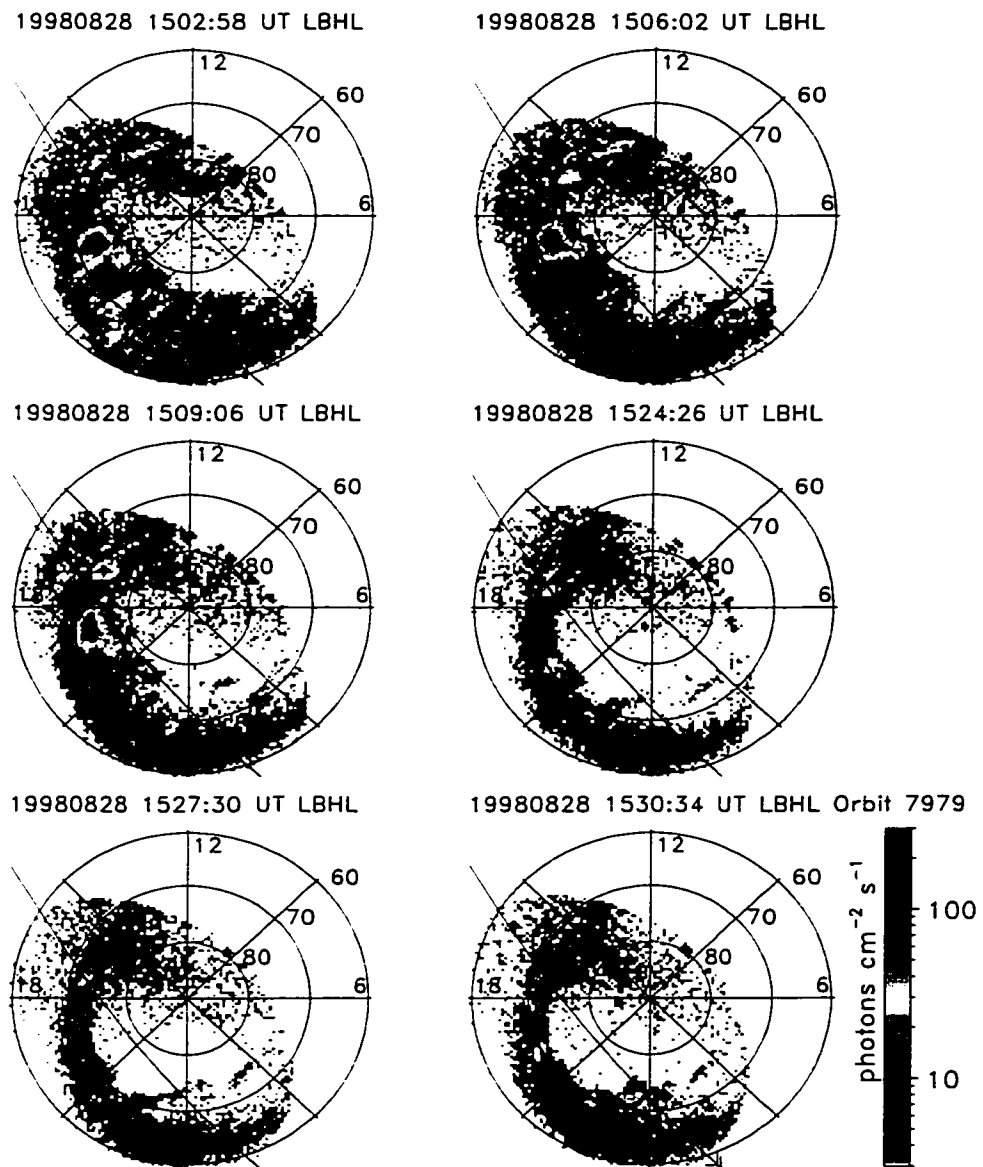


Figure C.14: UVI images corresponding to FAST orbit 7979.

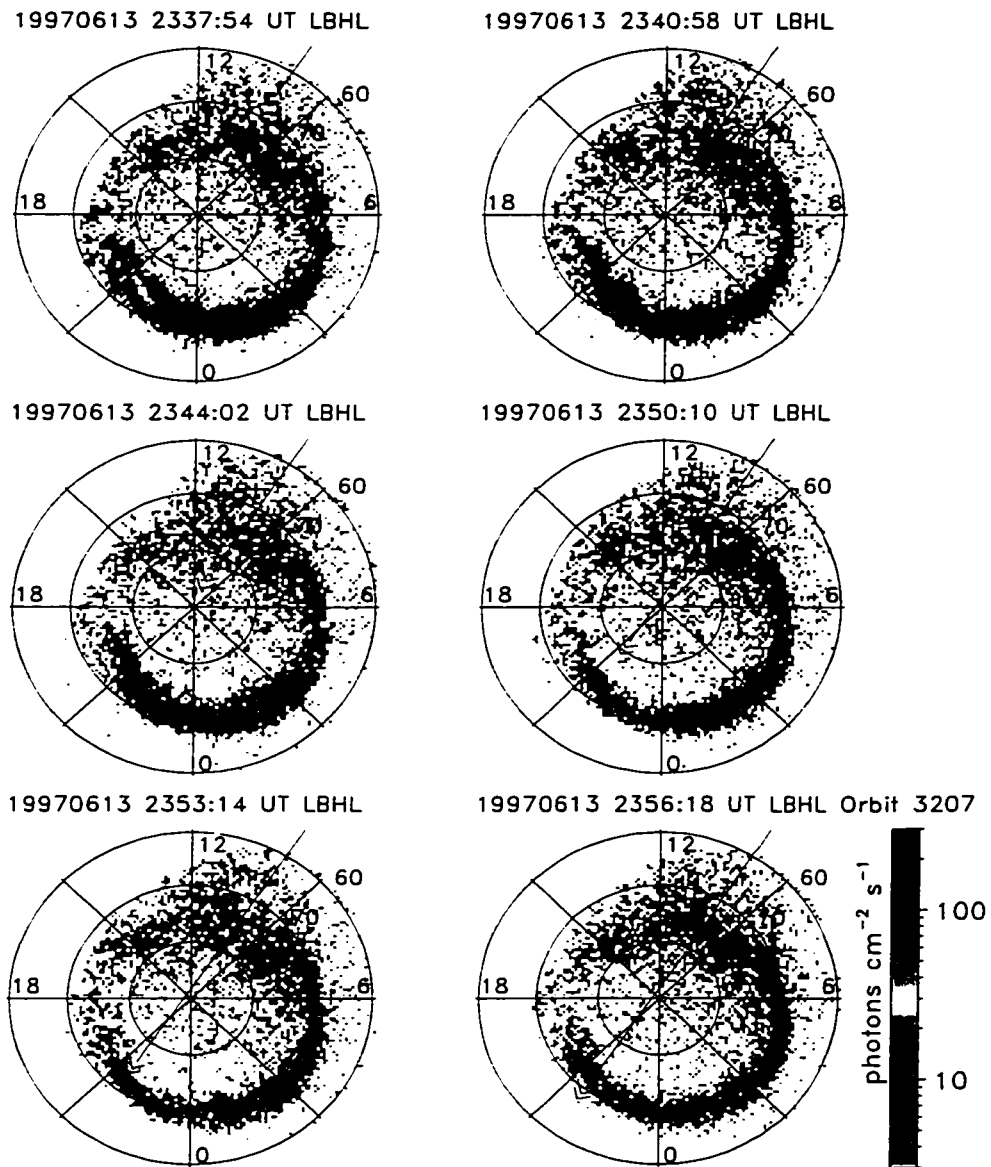


Figure C.15: UVI images corresponding to FAST orbit 7067.

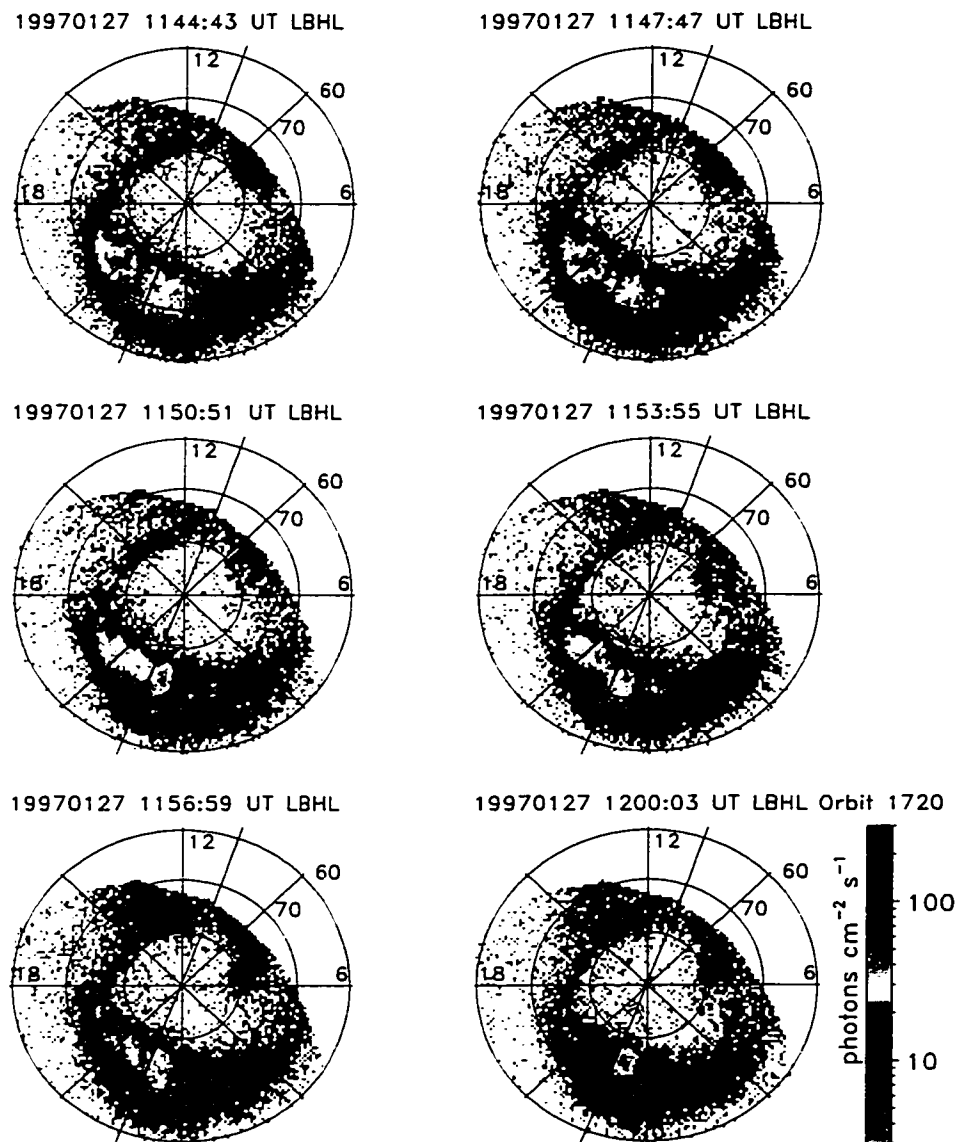


Figure C.16: UVI images corresponding to FAST orbit 1720.

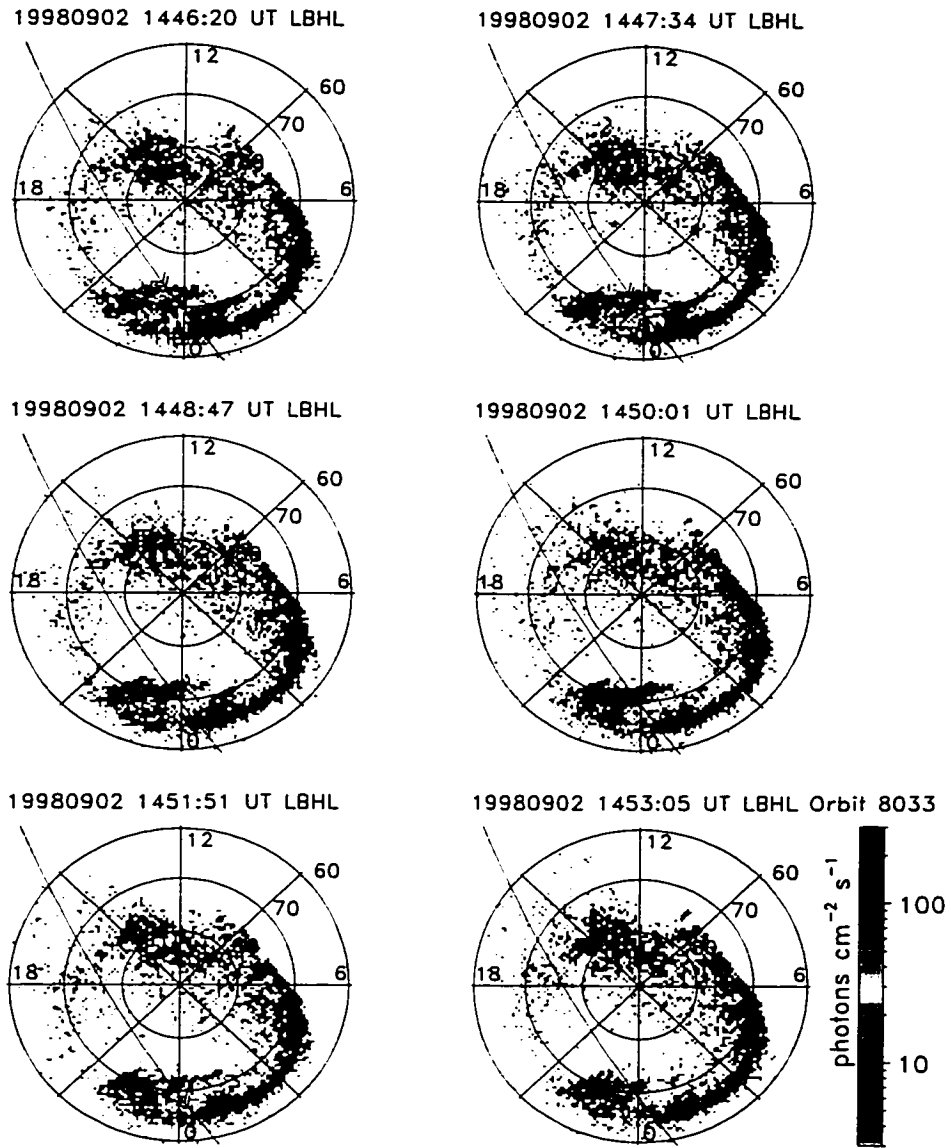


Figure C.17: UVI images corresponding to FAST orbit 8033.

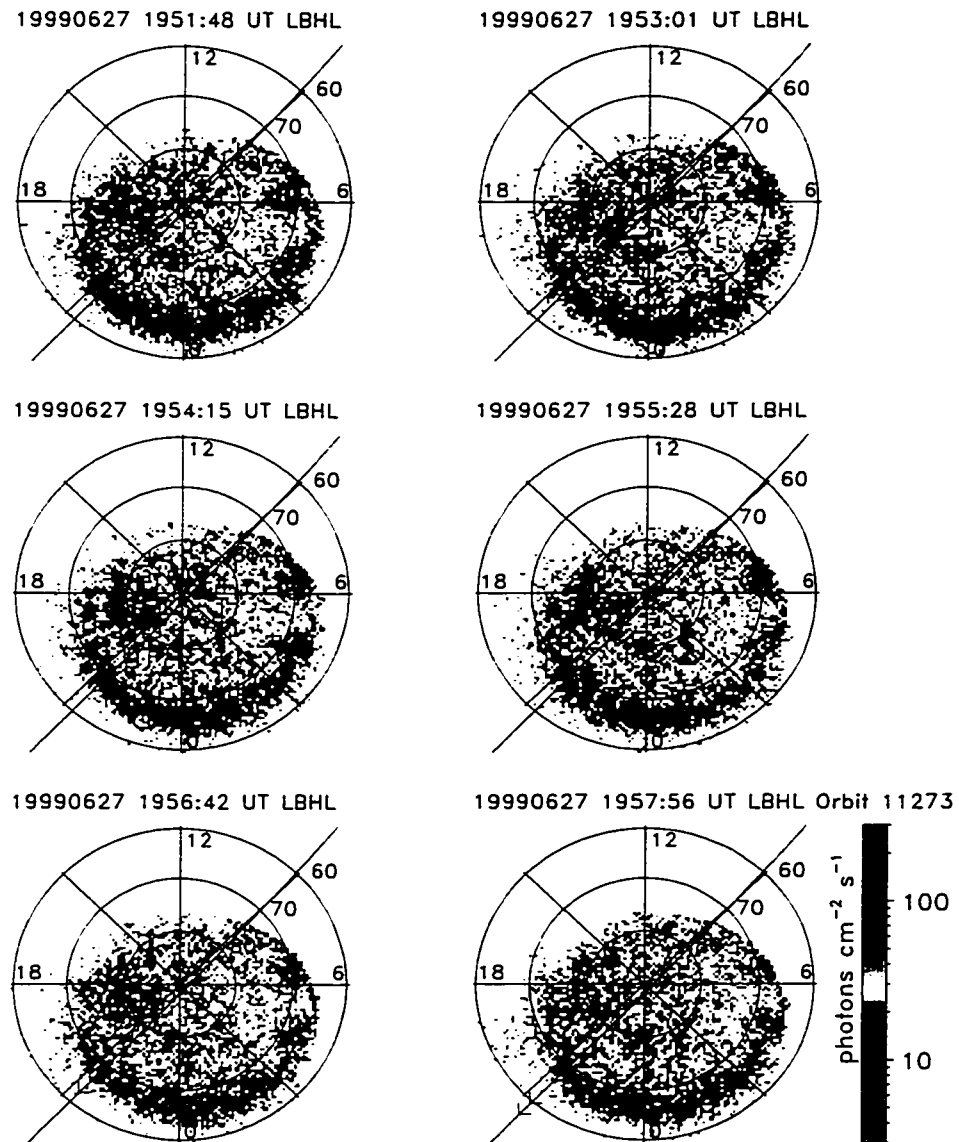


Figure C.18: UVI images corresponding to FAST orbit 11273.

VITA

Damien Han Ping Chua was born in Singapore in 1974 to Roland and Carol Chua. He was raised in Lynnwood, Washington and graduated salutatorian from Mariner High School (Everett, WA) in 1992. In 1996 he received a B.S. in Physics from the University of Puget Sound (Tacoma, WA). After finishing his undergraduate degree, he worked as a visiting scientist at the National Center for Atmospheric Research High Altitude Observatory (Boulder, CO) and the California Institute of Technology/Jet Propulsion Laboratory (Pasadena, CA). Between 1997 and 2002, he was a graduate student in the Department of Earth and Space Sciences (formerly Geophysics) at the University of Washington.